

**A GENERAL PURPOSE COMPUTATIONAL APPROACH
TO THE DESIGN OF GRADIENT COILS FOR
ARBITRARY GEOMETRIES**

by

Rostislav A. Lemdiasov

A Dissertation

Submitted to the Faculty

of the

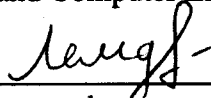
WORCESTER POLYTECHNIC INSTITUTE

in partial fulfillment of the requirements for the

Degree of Doctor of Philosophy

in

Electrical and Computer Engineering



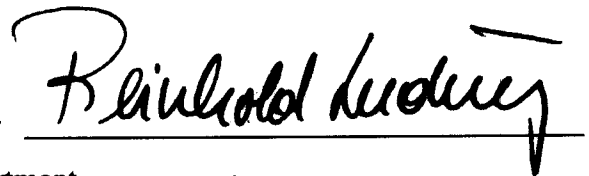
by

Rostislav A. Lemdiasov

July 27th, 2004

APPROVED:

Professor Reinhold Ludwig, Major Advisor



Electrical and Computer Engineering Department

Professor John M. Sullivan Jr.,



Mechanical Engineering Department

Professor William R. Michalson,



Electrical and Computer Engineering Department

Professor Donald R. Brown,



Electrical and Computer Engineering Department

Abstract

This research concentrates on two major engineering areas associated with biomedical instrumentation that have recently gained significant academic and industrial interest: the gradient coil design for Magnetic Resonance Imaging (MRI) and the high frequency full-wave field simulations with the Method of Moments (MoM).

A new computational approach to the design of gradient coils for magnetic resonance imaging is introduced. The theoretical formulation involves a constrained cost function between the desired field in a particular region of interest in space and the current-carrying coil plane. Based on Biot-Savart's integral equation, an appropriate weight function is introduced in conjunction with linear approximation functions. This permits the transformation of the problem formulation into a linear matrix equation whose solution yields discrete current elements in terms of magnitude and direction within a specified coil plane. These current elements can be synthesized into practical wire configuration by suitably combining the individual wire loops. Numerical predictions and measurements underscore the success of this approach in terms of achieving a highly linear field while maintaining low parasitic fields, low inductance and a sufficient degree of shielding. Experimental results confirm the field predictions of the computational approach.

Extending the numerical modeling efforts to dynamic phenomena, a novel MoM formulation permits the computation of electromagnetic fields in conductive surfaces and in three-dimensional biological bodies. The excitation can be provided with current loops, voltage sources, or an incident electromagnetic wave. This method enables us to solve a broad spectrum of problems arising in MRI: full-wave RF coil simulations, eddy currents predictions in the magnet bore, and induced currents in the biological body. Surfaces are represented as triangles and the three-dimensional bodies are subdivided into tetrahedra. This numerical discretization methodology makes the approach very flexible to handle a wide range of practical coil geometries. Specifically, in this thesis the MoM is employed to study the effect of switching gradient coils in the presence of a biological load.

Acknowledgments

I would like to express my sincere gratitude to my thesis advisor, Professor Reinhold Ludwig. Without his guidance, patience and words of appreciation I would not have been able to complete this dissertation.

I highly appreciate the criticism and comments provided by members of my thesis committee, John M. Sullivan, William R. Michalson, Donald R. Brown. Their input proved to be invaluable for success of this project.

I am grateful to my friends and co-workers from RF Lab for their encouragement and help: Aghogho Obi, Souheil Benzerrouk, Sonam Tobgay, Ming Fei, Praveen Kulkarni.

I am obliged to Bill Weir and Art Allard for construction of the gradient coils as well as to Karl Helmer and Mat Brevard for help provided during the experiments.

Special thanks to my sponsors, Craig Ferris and Jean King, for their enthusiasm and faith in success of the project.

I would like to express my deepest appreciation to my family. My parents, Anatoly and Tatiana Lemdiasov, inspired me with their endless moral support, patience and love.

Finally, I extend my gratitude to my wife, Victoria Lemdyasova, for her unlimited kindness, warmth, love and affection.

Support provided by INSL is greatly appreciated.

Contents

Abstract	i
Acknowledgments	ii
Contents	iii
List of Figures	v
List of Tables	xi
Notation	xii
Chapter 1 Introduction and Review	15
1.1 Introduction.....	15
1.2 Qualitative Description of MRI Imaging Method	17
1.3 Importance of Gradient Coils and Design Considerations	20
1.4 Literature Review.....	23
1.5 Objectives and Methodology	27
Chapter 2 Basics of Magnetic Resonance Imaging	29
2.1 Spins in a Magnetic Field	29
2.2 The Effect of Radiofrequency (RF) Pulses.....	31
2.3 Relaxation	32
2.4 Magnetic Field Gradients.....	33
2.5 Slice Selective Excitation	33
2.6 Frequency Encoding	35
2.7 Phase Encoding and Image Acquisition	35
Chapter 3 G_y Surface Gradient Coil	38
3.1 Design Goal and Quality Assessment.....	38
3.2 Prior Art	39
3.3 Theoretical Least Squares Formulation	47
3.4 Design of G_y Gradient Coils Based on the Least Squares Method.....	52
3.5 Additional Performance Improvements.....	56
3.6 Chapter Summary	63
Chapter 4 Stream Function Method for Gradient Coil Design	64
4.1 Theory.....	65
4.2 Methodology.....	68
4.3 System of Linear Equations	71
4.4 Mutual Inductance Calculation.....	75
4.5 Examples of Coil Design	76
4.6 Flat Coils.....	84
4.7 Comparison of the Least Squares Method and the Stream Function Method	91
4.8 Shielding.....	93
4.9 Graphic User Interface.....	98
4.10 Coil Construction.....	103
4.11 Experimental Results	112
4.12 Chapter Summary	118

Chapter 5 Formulation of Method of Moments for Arbitrary-Shaped Surfaces and Inhomogeneous Biological Bodies	120
5.1 Theoretical Considerations	121
5.2 Basis Functions	122
5.2.1 Discretization of a thin wire.....	122
5.2.2 Discretization of a perfectly conductive surface.....	123
5.2.3 Discretization of a 3D body	125
5.3 Total Electric Field	128
5.4 Matrix Representation and Testing of the Formulation.....	129
5.4.1 Testing with surface current function $\mathbf{f}_m^S(\mathbf{r})$	130
5.4.2 Testing with volume function $\mathbf{f}_m^V(\mathbf{r})$	131
5.5 Discretization	133
5.6 Validation of the Formulation.....	136
5.7 Additional Examples.....	140
5.8 Effect of Gradient Coils on a Biological Insert	147
5.9 Chapter Summary	149
Chapter 6 Conclusions and Recommendations.....	151
6.1 Summary and Conclusions	151
6.2 Recommendations for Future Work.....	154
References.....	155
Appendix A Mie Series Solution.....	158

List of Figures

Figure 2.1: (a) The magnetic dipole, (b) magnetic dipoles in the absence of an applied magnetic field.....	28
Figure 2.2: (a): Energy diagram, (b) precession of magnetic moment around the applied field \mathbf{B}_0	30
Figure 2.3: (a): Magnetization decay, (b) free induction decay (FID).....	31
Figure 2.4: Qualitative transverse and longitudinal relaxation behavior after the 90° pulse is turned off.....	32
Figure 2.5: Fourier transform correspondence of the sinc function.....	33
Figure 2.6: Spin-echo pulse sequence.....	35
Figure 2.7: Schematic representation of image formation via the Fourier Transform (FT and IFT denote, respectively, the forward and inverse Fourier Transform)....	36
Figure 3.1: Conceptual arrangement of three mono-planar surface gradient coils situated below the region of interest (ROI).....	37
Figure 3.2: G_y gradient coil design as originally proposed by Cho and Yi [14].	39
Figure 3.3: Magnetic flux density B_z in units of [T] for both the transversal and longitudinal direction throughout the ROI. The ROI is located 4 cm above the coil plane and ranges from 4 to 8 cm in y direction and from -2.5 to $+2.5$ cm in z and x directions, respectively.	39
Figure 3.4: Contours of magnetic flux density B_z in units of [T] in axial and sagittal cross-sections through the ROI. The spatial dimensions in x, y, z directions are given in [m]......	40
Figure 3.5: Simulations of the reconstructed image produced by the G_y gradient coil designed by Cho [14] with levels of y in terms of (z, x, y^*) coordinates. Here y^* (or YSTAR) is the predicted y -coordinate after Fourier space reconstruction. All spatial dimensions are recorded in [m].	41
Figure 3.6: Fabrication of prior art G_y gradient coil [14]......	42
Figure 3.7: (a) G_y coil [14] in a Plexiglas restrainer, (b) experimental setup for bench testing.....	43
Figure 3.8: Measured transversal magnetic flux density B_z in [G] recorded for the G_y gradient coil as proposed in [14], and based on a drive current of 1A. Spatial dimensions are recorded in [cm]......	43
Figure 3.9: Original G_y coil: (a) on the bench, placed in a Plexiglas cylindrical tube of 15cm diameter, (b) located inside the MR system.....	44
Figure 3.10: Picture and photographs of the phantom: (a) phantom schematics, (b), (c) different views of phantom. Each water compartment is 3mm in thickness.	45
Figure 3.11: Resulting images obtained from the Plexiglas phantom of Figure 3.10 with Cho's G_y surface coil. The coil plane resides 4.3 cm below the first water contour: (a) axial plane, (b) sagittal plane.	46

Figure 3.12: Set of basis functions f_{nm} chosen for the proposed least squares method. . .	49
Figure 3.13: New 5×4 G_y gradient coil design. The discrete numbers denote the wires placed in each groove.....	51
Figure 3.14: Magnetic flux density in [T] for the 5×4 G_y gradient coil. All spatial dimensions are given in [m].....	52
Figure 3.15: Simulations of the reconstructed image produced by the 5×4 G_y gradient coil. All spatial dimensions are given in [m].	52
Figure 3.16: A 6×4 G_y gradient coil wire pattern.....	53
Figure 3.17: Magnetic flux density B_z in [T] of the 6×4 G_y gradient coil. All spatial dimensions are in [m].....	53
Figure 3.18: Simulations of the expected image reconstruction produced by the 6×4 G_y gradient coil shown in Figure 3.16. All spatial dimensions are in [m].	54
Figure 3.19: A G_y gradient coil prototype.....	56
Figure 3.20: Six-loop coil G_y gradient coil.	56
Figure 3.21: Magnetic field B_z in [T] for the six-loop, G_y gradient coil. All spatial dimensions are recorded in [m].....	57
Figure 3.22: Simulations of the reconstructed image produces by the six-loop G_y gradient coil. All dimensions are listed in [m]......	57
Figure 3.23: Six-loop G_y gradient coil.	58
Figure 3.24: Photographs of the six-loop G_y coil placed in a 25 cm diameter Plexiglas tubular cylinder (left) and placed inside the 4.7T Bruker magnet with commercial gradient set (right).....	58
Figure 3.25: Resulting image of the phantom with the coil shown in Figure 3.23.....	59
Figure 3.26: B_z -component of the magnetic flux density in [T] along the vertical line ($x=0, z=0$) passing through the ROI: Cho's design [14], 5×4 design, 6×4 design, and six-loop design. Spatial dimension is recorded in [m].	60
Figure 3.27: Commercial G_y gradient coil (Bruker high-performance gradient set, 26mm inner diameter, 5 G/cm at 100 A drive current). Resulting image (FOV: 4cm by 4cm) of a marmoset brain acquired by a commercial gradient coil.....	61
Figure 3.28: Six-loop G_y gradient coil (coil plane size: 12 cm by 24 cm, 5 G/cm at 25 A drive current). Resulting image (FOV: 4cm by 4cm) of the six-loop G_y coil depicted in Figure 3.23. The surface coil was operated as phase encoding gradients.....	61
Figure 4.1: Conceptual arrangement of the gradient system.	64
Figure 4.2: Geometric surface source configuration $\mathbf{J}(\mathbf{r})$ that constitutes a bi-planar gradient coil.	65
Figure 4.3: Triangulated surface with exterior and interior boundaries.	67
Figure 4.4: Two nodes at which the current elements on the surface are evaluated.....	68
Figure 4.5: (a) Current element and basis function $\mathbf{f}_n(\mathbf{r})$, (b) one of the triangles associated with the selected node.	69

Figure 4.6: Interaction between the currents flowing in the triangles Δ_{mi} and Δ_{nj}	74
Figure 4.7: Surface discretization of the two plate crescent coil.	75
Figure 4.8: Stream function $\varphi(\mathbf{r})$ distribution in [A]; (a) original bi-surface coil layout, (b) wire patterns projected onto two flat planes.....	76
Figure 4.9: G_x crescent coil with $\alpha = 10^{-7}$, (a) wire pattern and z -component of the magnetic flux density, (b) wire pattern and absolute value of magnetic flux density, (c) streamlines of the magnetic flux density.	78
Figure 4.10: Flat coil surface discretization. Spatial dimensions are given in [m].....	80
Figure 4.11: Stream function distribution in [A]. All spatial dimensions are given in [m].	81
Figure 4.12: Wire pattern of the flat gradient coil and the magnetic flux density in the ROI.....	82
Figure 4.13: Mesh of the flat gradient coil. All dimensions are given in [m].	83
Figure 4.14: G_x gradient coil stream function pattern for different α values. All spatial dimensions are given in [m].....	85
Figure 4.15: G_y gradient coil stream function pattern for different α values. All spatial dimensions are given in [m].....	86
Figure 4.16: G_z unbalanced gradient coil stream function pattern for different α values. All spatial dimensions are given in [m].	87
Figure 4.17: G_z balanced gradient coil stream function pattern for different α values. All spatial dimensions are given in [m].	88
Figure 4.18: Dependence of the gradient coil characteristics on parameter α . (a) Gradient strength G in units of [G/cm/100A], (b) parasitic quality factor Q , (c) gradient uniformity U , (d) inductance L in units of [μ H]	89
Figure 4.19: Dependence of parasitic quality factor Q on gradient strength per unit resistance [G/cm/100A/ Ω].	91
Figure 4.20: Primary and secondary coils.....	92
Figure 4.21: G_x coil with $\alpha = 10^{-7}$ and $\beta = 0$. (a) Wire pattern and z -component of the magnetic flux density, (b) wire pattern and absolute value of magnetic flux density, (c) streamlines of the magnetic flux density.	93
Figure 4.22: G_x coil with $\alpha = 10^{-7}$ and $\beta = 0.1$. (a) Wire pattern and z -component of the magnetic flux density, (b) wire pattern and absolute value of magnetic flux density, (c) streamlines of the magnetic flux density.	95
Figure 4.23: Gradient Coil Designer.....	97
Figure 4.24: Five typical gradient coil configuration templates.	98
Figure 4.25: Biplanar mesh based on template Figure 4.24(c).	98
Figure 4.26: (a) Gradient dialog window, (b) moment dialog window, (c) region of interest.....	99
Figure 4.27: Stream function distribution over the coil surface.	100
Figure 4.28: Layout of the gradient coil.	100
Figure 4.29: z -component of the magnetic flux density in the Region of Interest.....	101

Figure 4.30: G_x coil, (a) stream function distribution, (b) wiring and magnetic flux density B_z [T], (c) magnetic flux density B_z [T] in the axial plane, (d) magnetic flux density B_z [T] in the coronal plane. All spatial dimensions are in [m].	103
Figure 4.31: Distortions of the G_x coil, (a) axial plane, (b) coronal plane. All dimensions are given in [m].	104
Figure 4.32: (a) Former of the G_x coil, (b) wiring in the G_x coil former.	104
Figure 4.33: G_y coil, (a) stream function distribution, (b) wiring and magnetic flux density B_z [T], (c) magnetic flux density B_z [T] in the axial plane, (d) magnetic flux density B_z [T] in the sagittal plane. All spatial dimensions are in [m].	106
Figure 4.34: Distortions of the G_y coil, (a) axial plane, (b) sagittal plane. All dimensions are given in [m].	107
Figure 4.35: Wirings of G_y and G_z coils in the acrylic former.	107
Figure 4.36: G_z coil, (a) stream function distribution, (b) wiring and magnetic flux density B_z [T], (c) magnetic flux density B_z [T] in the xz -plane, (d) magnetic flux density B_z [T] in the yz -plane. All spatial dimensions are in [m].	109
Figure 4.37: Distortions of the G_z coil, (a) coronal plane, (b) sagittal-plane.	110
Figure 4.38: Photographs of the gradient set.	111
Figure 4.39: Gradient coil set in the magnetic bore.	112
Figure 4.40: (a) Pulse applied to the G_y gradient coil, (b) pulse applied to the G_z gradient coil. Current is measured in [A]. Time is given in [s].	112
Figure 4.41: Phantom used in the experiment.	113
Figure 4.42: Image of the phantom (Figure 4.41) with the surface coil as a receiver coil (a) axial plane (xy -plane), (b) sagittal plane (yz -plane).	113
Figure 4.43: Image of the phantom (Figure 4.41) with the volume coil as the receiver coil (a) axial plane (xy -plane), (b) sagittal plane (yz -plane).	114
Figure 4.44: Superposition of the image of the phantom (Figure 4.41) with the figure of distortions in a sagittal plane (yz -plane).	115
Figure 4.45: Image of the rat with the surface coil as the receiver coil (a) axial plane (xy -plane), (b) sagittal plane (yz -plane).	116
Figure 4.46: Image of the rat with the surface coil as the receiver coil in the axial plane.	117
Figure 5.1: Generic problem configuration featuring conductive surface, a ring excitation (current loop), and a biological body.	121
Figure 5.2: 1D current element with current flow direction.	121
Figure 5.3: RWG current element consisting of two triangles T_n^+ and T_n^- and sharing a common edge. The vectors ρ_n^+ and ρ_n^{c+} reside in the surfaces A^\pm and refer to observation and centroid points, respectively.	123

Figure 5.4: (a) An edge \mathbf{l} residing within a particular volume and all neighboring tetrahedra $\Delta_i (i=1,2,\dots,N)$, (b) the same edge \mathbf{l} showing the connectivity to one of the tetrahedra.	124
Figure 5.5: Top-down view of the solenoidal element which depict the divergence-free property of $\mathbf{f}^V(\mathbf{r})$	126
Figure 5.6: Magnitude of normal component of the electric field \mathbf{E} [V/m] over the surface of the sphere ($f = 200$ MHz, $\epsilon_r = 2$, $\sigma = 0.0$ S/m). (a) exact Mie series solution, and (b) MoM prediction.....	136
Figure 5.7: Magnitude of the electric field \mathbf{E} [V/m] on the surface of the sphere ($f = 200$ MHz, $\epsilon_r = 2$, and $\sigma = 0.0$ S/m). Comparison of exact (solid line) with MoM solutions (dashed line) along the a) x , b) y , and c) z – axes, respectively. All spatial dimensions are in [m]......	136
Figure 5.8: Magnitude of the electric field \mathbf{E} [V/m] on the surface of a sphere ($f = 200$ MHz, $\epsilon_r = 2$, $\sigma = 0.5$ S/m). (a) exact Mie solution, (b) MoM prediction.	137
Figure 5.9: Magnitude of the electric field \mathbf{E} [V/m] on the surface of a sphere ($f = 200$ MHz, $\epsilon_r = 2$, $\sigma = 0.5$ S/m). Comparison of the exact Mie series solution (solid line) with MoM prediction (dashed line) along the a) x -, b) y -, and c) z - axes. All spatial dimensions are in [m].	137
Figure 5.10: Magnitude of the electric field \mathbf{E} [V/m] on the surface of a sphere ($f = 200$ MHz, $\epsilon_r = 80$, $\sigma = 1.0$ S/m). (a) exact Mie solution, (b) MoM prediction.	138
Figure 5.11: Magnitude of the electric field \mathbf{E} [V/m] on the surface of a sphere ($f = 200$ MHz, $\epsilon_r = 80$, $\sigma = 1.0$ S/m). Comparison of the exact Mie series solution (solid line) with MoM prediction (dashed line) along the a) x -, b) y -, and c) z - axes. All spatial dimensions are in [m].	138
Figure 5.12: Gradient coil of Figure 3.20 inside a metallic cylinder.....	139
Figure 5.13: Distribution of surface current density \mathbf{J} [A/m] induced in the magnet bore.	140
Figure 5.14: Gradient coil and a biological load inside the metallic cylinder.....	141
Figure 5.15: Surface current density \mathbf{J} [A/m] induced in the metallic cylinder and distribution of the electric field \mathbf{E} [V/m] on the sphere.....	141
Figure 5.16: Electric field \mathbf{E} [V/m] distribution inside the sphere.....	142
Figure 5.17: Mesh of TEM resonator.	143
Figure 5.18: Introducing lumped elements into the MoM formulation.....	144
Figure 5.19: Surface current density \mathbf{J} [A/m] induced in the TEM resonator.....	145
Figure 5.20: Absolute value and streamlines of the magnetic field \mathbf{B} [T] at a cross-section inside the volume coil. All spatial dimensions are given in [m]......	145
Figure 5.21: Electric field \mathbf{E} [V/m] created by the G_x gradient coil: (a) biological body inside the coil, (b) three cross-sections of the body, (c) electric field along the x -axis, (d) electric field along the y -axis, (e) electric field along the z -axis. All dimensions spatial are given in [m]......	146

Figure 5.22: Electric field E [V/m] created by the G_y gradient coil: (a) biological body inside the coil, (b) three cross-sections of the body, (c) electric field along the x -axis, (d) electric field along the y -axis, (e) electric field along the z -axis. All dimensions spatial are given in [m]..... 147

Figure 5.23: Electric field E [V/m] created by the G_z gradient coil: (a) biological body inside the coil, (b) three cross-sections of the body, (c) electric field along the line passing through the center of the sphere and directed as along the $(1,1,1)$ vector. All dimensions spatial are given in [m]. 148

List of Tables

Table 1: Gradient strengths, resistances and quality factors of three mono-planar G_y surface gradient coils.	55
Table 2: Gradient strength and quality factor of six-loop G_y surface gradient coil.	60
Table 3: Performance of crescent coil depicted in Figure 4.9.	80
Table 4: Performance of the flat coil shown in Figure 4.12.	83
Table 5: Effects of the shield on the performance of the crescent gradient coil.	97
Table 6: Characteristics of the manufactured coils.	111

Notation

a	radius of a sphere
\mathbf{A}	Magnetic vector potential
A	area of a triangle or a face
A_{Δ}	area of the triangle Δ
A_s	area of the shield
A^{\pm}	area of left/right triangle of the RWG current element
\mathbf{b}	right hand side vector
B_0	main magnetic field
$B_{n\Delta}$	normal component of the magnetic field at the center of Δ^{th} triangular patch
$B_{\text{off},z}$	z -components of offset magnetic field
B_z	z -component of magnetic field
$B_{z,\text{des}}$	z -component of the desired magnetic field
BW	bandwidth
$c_n(\mathbf{r})$	coefficient relating current in the current element and magnetic field at the point \mathbf{r} located in the region of interest
\mathbf{C}	divergence-free vector defined in (5.17)
d	thickness of excited slice
\mathbf{d}	vector of shortest distance from the node (or edge) to the opposite edge
$d_{n\Delta}$	coefficient relating current in the current element with the magnetic field in the triangle Δ
\mathbf{D}	electric field density
\mathbf{D}^{SS} , \mathbf{D}^{SV} , \mathbf{D}^{VS} , \mathbf{D}^{VV} , \mathbf{D}^{SL} , \mathbf{D}^{VL}	matrices of interaction between line currents, surface currents and volume currents
$D_m^{S\text{-Inc}}$, $D_m^{V\text{-Inc}}$	matrices of interaction between surface current, volume currents and incident wave
\mathbf{e}	vector of the opposite edge
\mathbf{E}	electric field
E_0	amplitude of an incident wave
f	frequency
$f_n(z, x)$	basis function
\mathbf{f}_n^L	basis function for wires
\mathbf{f}_n^S	basis function for highly conductive surfaces
\mathbf{f}_n^V	basis function for volume
FOV	field of view
G_x	gradient of magnetic field in x -direction
G_y	gradient of magnetic field in y -direction
G_z	gradient of magnetic field in z -direction

I_n	current in n^{th} current element
\mathbf{j}	current density
\mathbf{J}	current density
J_x, J_y, J_z	components of current density vector
k	wave number
\mathbf{l}	edge vector
L	characteristic size of the body
L_{mn}	mutual inductance between m^{th} and n^{th} basis functions
$M_{\text{longitudinal}}$	longitudinal magnetization
$M_{\text{transverse}}$	transverse magnetization
\mathbf{M}	torque vector
M_{px}, M_{py}, M_{pz}	components of the torque vector
\mathbf{n}	unit length normal vector
\mathbf{n}_{Δ}	unit length normal vector to triangle Δ
p	surface number
P	number of surfaces that gradient coil consists of.
Q	quality factor (parasitic gradients)
\mathbf{r}, \mathbf{r}'	coordinates
R	resistance
T_1	spin-lattice relaxation time
T_2	spin-spin relaxation time
T_2^*	spin-spin relaxation time
$T_{2,\text{inhomo}}$	inhomogeneity spin-spin relaxation time
$T_{2,\text{suscept}}$	susceptibility spin-spin relaxation time
$T_{2,\text{diff}}$	diffusion spin-spin relaxation time
T_n^+	“left” triangle of an RWG current element
T_n^-	“right” triangle of an RWG current element
U	ratio of minimal value of gradient to the maximum value.
\mathbf{v}	vector of the basis function
W	weight in a cost function
W_{magn}	magnetic energy
\mathbf{X}	vector of unknowns
\mathbf{Z}	system matrix

Greek Symbols

α	weight of magnetic energy term
β	shielding weight coefficient
δ_{mn}	Kronecker delta

Δ	number of a triangles or a tetrahedra
$\Delta\varphi$	size of the level of the stream function
ε	electrical permittivity
φ	stream function
φ	Green's function
$\varphi_{\min}, \varphi_{\max}$	minimum and maximum values of the stream function
φ_{level}	value of the contour line chosen for discrete wiring
Φ	cost function
γ	gyromagnetic ratio
λ	wavelength
λ_0	wavelength in a free space
$\lambda_{px}, \lambda_{py}, \lambda_{pz}$	Lagrange multipliers
μ_0	permeability
ω	angular frequency

Chapter 1

Introduction and Review

1.1 Introduction

Nuclear Magnetic Resonance (NMR) is a method that exploits the resonance behavior that is exhibited by certain substances when placed into a strong magnetic field. The phenomenon of NMR was discovered by E.K. Zavoisky in 1944 and independently by Felix Bloch and Edward Purcell in 1946. These researchers discovered that electromagnetic waves at a certain frequency are attenuated dramatically when passing through a sample placed in a strong external magnetic field. The resonant frequency was found to be proportional to the strength of the external magnetic field.

More recently, Magnetic Resonance Imaging (MRI) as a medical imaging method is based on the exploitation of NMR for biological bodies. MRI is a relatively new method used in soft tissue medical imaging that came into widespread use in the 1980s. In the United States alone there are presently over 7,000 MR systems in clinical use. The

method utilizes several encoding techniques in order to obtain information about the inner structure of the biological sample under consideration.

MRI is fundamentally different from another popular imaging method: Computed Tomography (CT). In Computed Tomography the biological sample is exposed to X-ray projections from many directions. The acquired information is then used to reconstruct the inner structure of the sample. There are several key advantages of MRI over CT:

- MRI relies on radio waves instead of harmful X-rays. This allows the use of MRI for such patients as children and pregnant women. In addition, there is no need to protect the medical personnel from potentially harmful radiation.
- MRI is significantly more sensitive to the presence of hydrogen, one of the most abundant components in human organs.
- Contrast in MRI depends not only on the hydrogen density, but also on the additional properties of the sample described by the T_1 and T_2 relaxation time constants (which will be discussed in Chapter 2). These constants can be exploited to yield high quality images.
- MRI is sensitive to the presence of chemical bonds in molecules. For instance, the chemical frequency shift phenomenon allows one to determine the amount of fatty tissue.

However, magnetic resonance imaging has also several disadvantages:

- A strong and uniform magnetic field exceeding 1 T has to be created. The required superconducting magnets increase the cost of operating the MRI scanners significantly. From a patient's safety point of view, there appears to be no evidence of any negative effects arising from the strong magnetic field.

Nonetheless, the Food and Drug Administration is presently restricting the field strength for human imaging to 3 T.

- MRI cannot be used for claustrophobic patients (due to the presence of encircling magnets) and persons wearing metallic implants.

The basic physical principle of NMR is as follows. Certain substances, when placed in a strong magnetic field, selectively absorb radio waves at a frequency that is proportional to the strength of the applied static magnetic field. Nuclei having magnetic moments attempt to align themselves in this external magnetic field. The principles of quantum mechanics dictate that there exist several energy levels associated with the magnetic moments of these nuclei. The respective distribution of the nuclei concentration between lower and upper energy levels depends on temperature and follows a Boltzmann distribution. If the energy $E = hf$ of the RF pulse equals the difference between these energy levels, then we have a resonance at the frequency f (h is the Planck's constant). During such an RF pulse nuclei switch to a higher energy level. After the RF pulse is turned off, the nuclei return to their equilibrium state and emit the accumulated energy that can be registered by a receiver coil. The pulse of magnetic energy radiated by the sample is referred to as *echo signal*.

1.2 Qualitative Description of MRI Imaging Method

As mentioned before, MRI uses the NMR phenomenon to create high-resolution images of the body. If, in addition to the main magnetic field (usually directed along the z -axis), we apply an extra magnetic field having a linear gradient in the z -direction, then different

parts of the sample will experience a varying field depending on the location along the z -coordinate. Since the resonant frequency depends on the strength of the magnetic field, each slice of the body orthogonal to the z -axis will possess its own resonant frequency. Furthermore, if we apply an RF pulse at frequency f to this sample, then only one slice having the resonant frequency f will be excited, and others remaining unaffected. When the RF pulse is terminated, the amount of energy registered by the receiver coil will be proportional to the number of nuclei in the excited z -slice. The technique of applying a gradient of the magnetic field along the z -direction is referred to as *slice selection*. The application of a comparatively low gradient strength (0.1 – 1.0 G/cm) allows us to deposit the energy of the RF pulse only to a certain slice aligned with the z -axis of the sample. An RF pulse typically has a rectangular shape in the frequency domain to sharply define the slice boundaries. The position of the z -slice depends on the center frequency of the RF pulse; the thickness of the z -slice depends on the spectral width of the RF pulse and on the corresponding gradient field strength. As we can see, the application of the gradient of magnetic field helps us to determine the number of nuclei in the z -slice of interest. This, however, is not sufficient to obtain full spatial information to create an image of the biological body, because different areas of this z -slice contain different nuclei densities.

To elicit more detailed spatial information, additional coil systems are needed. After the RF pulse and the z -gradient field are turned off, we apply a gradient field in x -direction. The excited z -slice can now be subdivided into x -strips, each having its own resonant frequency. Under this condition, each x -strip will radiate the echo signal at its own resonant frequency. The registered signal will contain all resonant frequencies from

the entire z -slice. After performing the Fourier Transform of this signal, we are able to calculate the weight of each frequency in the echo signal. Each weight is proportional to the number of nuclei in each x -strip. The technique of applying the gradient of the magnetic field along the x -direction is referred to as *frequency encoding*. Consequently, the x -axis is identified as the *frequency encoding direction*.

To obtain information from the third remaining direction – along the y -axis – we need to apply a gradient field in the y -direction. This is accomplished by a trick: the RF pulse excites a chosen z -slice several times in a row, each time increasing the value of the G_y -gradient. By doing this we record signals from each x -strip many times. Each voxel (elementary volume) of this x -strip, however, produces an echo signal, the phase of which depends on the position of the voxel along the y -axis. Again, the Fourier Transform enables us to determine the weight of each voxel in each x -strip. Finally, taking all gradient steps in sequence, we are able to determine the individual signal response from each voxel of the sample.

The MRI method gains additional versatility from the fact that the echo signal depends not only on the nuclei density, but also on other properties of the biological tissue. The most important properties are the so-called *spin-lattice relaxation constant* T_1 and the *spin-spin relaxation constant* T_2 . The physical meaning of these parameters as well as a more detailed description of the basics of MRI can be found in Chapter 2.

1.3 Importance of Gradient Coils and Design Considerations

In an MR apparatus, the gradient fields are created by so-called *gradient coils*, which are labeled G_x , G_y , G_z . The purpose of these coils is to create a gradient of the z -component of the magnetic field in all three (x, y, z) directions. In the previous section we assumed that the gradient fields depend perfectly linearly on the corresponding coordinates and that those fields can be made as strong as needed. However, technologically it is difficult to achieve both strong and highly linear magnetic fields. A low magnetic field implies that the spatial resolution of an image is limited. Poor uniformity of the magnetic fields implies that the image will appear distorted. Unfortunately, a strong gradient field often can be achieved only by sacrificing the gradient uniformity, and vice versa. There exists a trade-off between gradient field strength and magnetic field gradient uniformity. Depending on the application, more emphasis may be placed on either the strength of the gradient field or on good gradient uniformity. This creates a need to design a range of gradient coils: from high strength magnetic fields to highly uniform magnetic fields. Coils that are able to produce a strong magnetic field usually have low magnetic energy (low inductance).

Switching magnetic fields induce electric currents in conducting media. The induced currents, in turn, create a magnetic field that opposes the applied magnetic field. These induced currents, or eddy currents, take a considerable time (milliseconds) to decay; their presence normally has a negative effect on the resulting image quality. Thus, the need arises to actively shield these gradient coils. A shield in this context is an additional coil that is connected in series with the respective gradient coil and that minimizes the magnetic field leakage created by the gradient coil beyond its outer

dimensions. By introducing the shield we decrease eddy currents at the expense of reducing the gradient strength and the magnetic field gradient uniformity.

When a gradient coil is placed inside a strong static magnetic field, it will experience a significant net torque when the current is turned on. Consequently, there is a need to cancel the net torque acting on the coil. If the gradient coil is designed with built-in torque cancellation (self-balancing), then in most cases it will produce a weaker gradient field of less uniformity. Moreover, if this coil is shielded, then the shielding effect will also decrease.

Most of the gradient coils in today's MRI scanners have cylindrical shape, and most of the research on gradient coils is done for cylindrical coils. However, if for example a surgical intervention is required, there is a desire to design gradient coils of particular shapes: flat rectangular, crescent, etc. Sometimes there may exist a need to have an opening in the coil to ease access to the sample. Obviously, if we impose certain shape constraints, it will affect the performance of the gradient coil.

Consequently, there is a trade-off between the gradient strength, the coil's gradient uniformity, the shielding degree, the net torque cancellation and the geometry of the coil. Improving anyone of these five characteristics can in most cases only be achieved at the expense of worsening the other four.

As a result, researchers are seeking new methods of designing gradient coils of specific shapes and parameters capable of investigating the various trade-offs. In particular, the methods should have the capability:

- To be able to work with a wide variety of gradient coil shapes.
- To parametrically control the magnetic energy (and gradient strength) of the coil.

- To have the possibility of designing a shielded gradient coil and to parametrically control the degree of shielding.
- To have the option of designing a self-balanced gradient coil.

An important characteristic of the gradient coil is the time constant $\tau = L/R$ (L is the total inductance, and R is the total wire resistance). If the time constant is short, we will be able to switch the gradient coil faster and, thereby, improve image quality as well as image acquisition time. However, there exists a negative effect: rapidly changing magnetic fields induce electric fields. These electric fields, if sufficiently high, induce currents in the biological sample and undesired nerve stimulation may occur. The threshold for nerve stimulation at low frequencies is about 6.2 V/m. Having designed the gradient coil, we have to ensure that this threshold is not exceeded. To find the electric fields arising in the sample, we have employed the Method of Moments (MoM), which approximates the electric current inside the sample by a set of elementary currents. The total electric field is then a superposition of the electric field created by the elementary currents and the field created by the gradient coil (excitation field). The current elements interact with the excitation field and among themselves. It is possible to establish a system of linear equations for values of the current elements. Once the system of equations is solved, we are able to calculate and plot the electric field inside the sample. The details of the MoM derivation are presented in Chapter 5.

1.4 Literature Review

Over the past twenty years a variety of theoretical design methods for the construction of gradient coils have been developed. The paper by Bangert and Mansfield [1] was one of the earliest ones on the subject. They formulated the problem of achieving high gradient field while providing low inductance. They also mentioned some simple ideas of how the gradient coil can be built. For example, four appropriately positioned infinite wires already constitute a gradient coil. However, infinite wires can, of course, only crudely approximate a realistic coil and the approach is therefore only of academic interest. To obtain a practical design, return paths have to be introduced.

Several general methodologies are described in a review paper by R. Turner [2]. His paper describes some common gradient coil designs as well as several theoretical approaches such as matrix inversion methods [3-6], stream function methods, and target field methods. The target field methods have gained widespread interest due to their computational ease in determining a suitable wire pattern. Specifically, Turner [7] sets a desired (or target) magnetic field on the cylindrical surface inside the cylindrical gradient coil. After this he calculates a current distribution on the surface of the gradient coil to achieve such a magnetic field. Also, in [8], Turner considers a cylindrical coil and represents its inductance in terms of the current distribution over the coil. He then minimizes the inductance subject to the magnetic flux density subject to a desired field distribution in the region of interest (ROI). Turner and Bowley [9] have additionally studied the effect of passive shielding of the gradient coils. They showed that the introduction of passive shielding reduces the magnetic field in the ROI at high frequencies (when the skin depth is much less than the shield thickness). Bowtell and

Mansfield [10] used a similar approach to design an actively shielded gradient coil. They showed that the shield helped to minimize the magnetic field outside of the gradient coil by at least two orders of magnitude.

Another successful application of the target field method related to the design of gradient coils was made by H. Liu [11]. He considered a bi-planar design and developed an expression for the magnetic energy of the coil, which is proportional to the total inductance. After expanding the surface current in a Fourier series, he was able to determine optimal values for the series coefficients that minimize the magnetic energy subject to the magnetic field being equal to a desired distribution throughout the ROI.

In yet another paper [12] D. Green *et al.* used a very similar approach to [11] in their design approach for uniplanar gradient coils. Specifically, they minimized a weighted combination of power, inductance, and the squared difference between the actual and the desired field. Again, representing the current as a Fourier series, they found optimal coefficients that minimize the cost function.

Leggett *et al.* [13] consider the multilayer transverse cylindrical gradient coils. They again expanded the current in a Fourier series. They next devised a cost function as a weighted combination of inductance and power loss for the condition that the magnetic field equals certain values at specified points.

The paper of Cho and Yi [14] was one of the first devoted to the explicit design of surface gradient coils. The authors use simple symmetry ideas to design layouts for the three surface gradient coils (G_x , G_y , G_z). This work provides us with an idea of how the coils would appear and how the magnetic field is expected to behave. However, these coil designs are far from optimal. In his dissertation, Funan Shi [15] used a number of

optimization techniques to produce a better wire layout for all three coils. He was able to show that the magnetic field gradient uniformity can be increased dramatically. In an extension of their work, F. Shi and R. Ludwig [16] concentrated on the analysis of the three gradient coils designed by Cho.

However, despite their apparent success, all these methods suffer from a common disadvantage: they are only applicable to particular coil geometries such as cylindrical planes, or single and bi-planar surfaces. In this research, we describe a new approach for coil design that is largely independent of the shape of the source-carrying surface. This is accomplished by discretizing the surface into triangular patches, and then defining within each element a current flow formulation. We will demonstrate the success of this approach by going through the design process of several coil geometries. In particular, we will show that torque-free shielded high performance gradient coils can be constructed in an easy and flexible way.

A considerable amount of research has been carried out to efficiently formulate the Method of Moments (MoM) for a wide range of applications. There are two types of structures that are most actively investigated: infinitely conductive metallic surfaces and 3D bodies characterized by values of electric permittivity and conductance.

The significant contribution by Rao et al. [17] has resulted in the introduction of Rao-Wilton-Glisson (RWG) basis functions that describe the current distribution on an infinitely conductive surface. The surface is discretized into triangular patches and the RWG basis function is non-zero for two triangle patches sharing the common edge. The authors showed that these basis functions yield superior field accuracy when using the MoM for scattering problems in the frequency domain.

The paper of Rao and Wilton [18] represents the time-domain version of the basic frequency formulation [17]. The authors can demonstrate good agreement of their results with other researchers. Chen et al. [19] discuss the fact that RWG basis functions fail at very low frequencies. They found a way to overcome this problem by using so-called loop-tree basis functions in conjunction with RWG. In particular, the authors notice that the surface current can be divided into divergence-free and curl-free parts. They demonstrate their success by showing that excellent agreement can be obtained with the classical Mie solution.

D.H. Schaubert et al. [20] consider the scattering of a plane wave by a dielectric body of arbitrary shape. The body is discretized into tetrahedra and each face is associated with a basis function. These functions are in fact a 3D extension of the surface RWG functions introduced in [17]. An electric flux density vector \mathbf{D} can then be approximated through the use of these 3D functions. The authors were able to obtain results in agreement with other researchers. In our opinion, this formulation suffers from a serious drawback: the vector \mathbf{D} is divergence-free in the dielectric, while the volumetric basis functions have non-zero divergence.

S. Antenor and L. Mendes [21], [22] describe a way to overcome this difficulty: a divergence-free basis functions can be introduced. They use these functions in order to approximate the equivalent polarization current in the dielectric object.

In this dissertation we develop a formulation that considers the highly conductive surface of a coil and the biological (conductive) 3D sample volume at the same time. For the surfaces we use RWG current elements and for the 3D bodies the divergence-free

basis functions. Several types of excitation are possible: excitation by loops of current, excitation by an incident electromagnetic wave, and excitation by a voltage source.

1.5 Objectives and Methodology

Central objective of this dissertation is a new design approach for the construction of gradient coils for magnetic resonance imaging. The theoretical formulation involves a constraint cost function that relates the desired field in a particular region of interest in space to an almost arbitrarily defined surface which carries the current configuration. The approach is based on Biot-Savart's integral equation. An appropriate weight function in conjunction with linear approximation functions enables us to transform the problem formulation into a linear matrix equation whose solution yields discrete current elements in terms of magnitude and direction within a specified coil surface. Numerical predictions for the G_x , G_y , G_z gradient coils are used to achieve a highly linear field, while maintaining good gradient uniformity and low inductance. In particular, the following items are identified:

- Development of a mathematical model that allows the effective simulation and design of a gradient coil over arbitrary surfaces.
- Creation of a friendly Graphic User Interface (GUI) to set the model parameters.
- Performance of simulations, construction and testing the gradient coil set in an MR system.
- Development of a Method of Moments formulation that can perform a full wave analysis of a biological body in the region of interest.

The organization of this dissertation is as follows. In Chapter 2 the basics of magnetic resonance imaging theory is presented. Planar G_y gradient coil is described in Chapter 3. In Chapter 4 we provide a mathematical formulation for the shielded and unshielded coil design of arbitrary geometries. A constructed prototype is then presented and its performance is compared with the model predictions. In Chapter 5 we introduce a Method of Moments formulation for conductive surfaces and biological bodies. Finally, Chapter 6 summarizes the accomplishments of this thesis research and points out future research directions.

Chapter 2

Basics of Magnetic Resonance Imaging

2.1 Spins in a Magnetic Field

Most nuclei possess a property called spin angular momentum, which is the basis of nuclear magnetism¹. Figure 2.1 depicts a nucleus spinning around its axis. Since nuclei are charged, the spinning motion causes a magnetic moment, which is collinear with the direction of the spin axis.

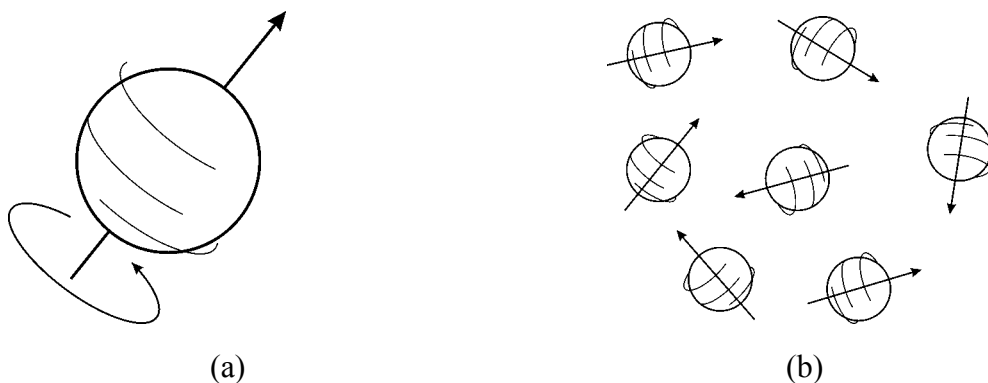


Figure 2.1: (a) The magnetic dipole, (b) magnetic dipoles in the absence of an applied magnetic field.

¹ The details of this chapter are in part a compilation of “Basic Principles of MR Imaging”, Paul J. Keller [26].

To elucidate the basic magnetic resonance principle, let us consider a collection of protons as in Figure 2.1. In the absence of the externally applied magnetic field, the individual magnetic moments have no preferred orientation. However, if a static magnetic field is applied, the magnetic moments have a tendency to align with this external field. According to quantum mechanics, the magnetic moments adopt one of two possible orientations: parallel or antiparallel to the magnetic field \mathbf{B}_0 . Alignment parallel to the magnetic field has a lower energy state and, therefore, is preferred (Figure 2.2(a)). Since the energy difference between two states is very small, thermal energy causes the two states to be almost equally populated. The population difference results in a net bulk magnetization.

The spin associated with the magnetic moment causes the moment to precess around the axis of \mathbf{B}_0 . Since more nuclear spins are aligned along the field, the magnetization is also directed along \mathbf{B}_0 . The precessional frequency is given by the Larmor equation:

$$\gamma B_0 = f, \quad (2.1)$$

where f is the precessional frequency, γ is a constant which depends on the type of nucleus. For a hydrogen nucleus γ is equal to $\gamma_H = 4257 \text{ Hz/Gauss}$. Therefore, in a magnetic field of 2 T the precession frequency is 85.5 MHz.

Figure 2.2 shows that since energy is proportional to frequency, ΔE may be defined in terms of the frequency of radiation, which is necessary to induce transitions of the spin states between the two energy levels.

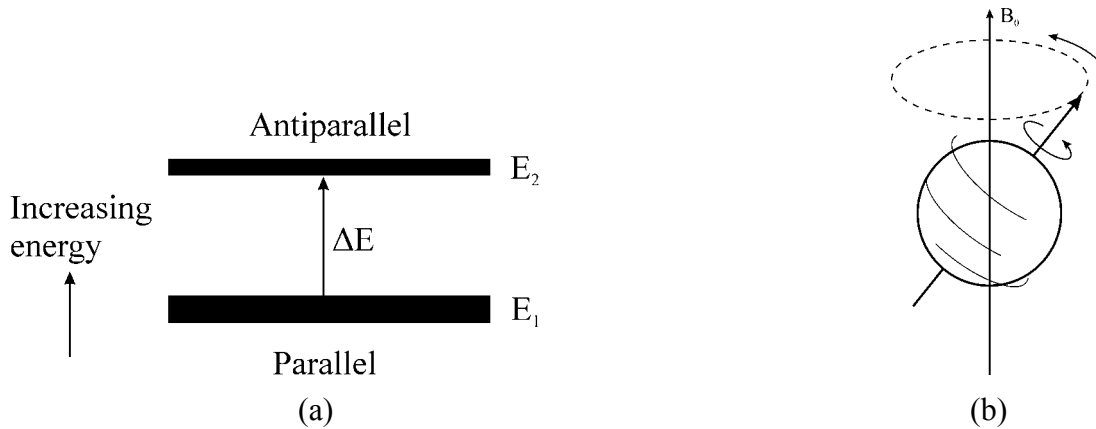


Figure 2.2: (a): Energy diagram, (b) precession of magnetic moment around the applied field \mathbf{B}_0 .

2.2 The Effect of Radiofrequency (RF) Pulses

If we apply a pulse of RF magnetic field at the Larmor frequency, its energy will be absorbed by the nuclei. During such a pulse the bulk magnetization \mathbf{M} will precess around the \mathbf{B}_1 axis. If the RF excitation is turned on only for a short period of time, the net magnetization is rotated by a certain angle away from the longitudinal axis. We call this angle a flip angle. We can choose the length of the pulse so as to obtain, for example, 90 and 180-degree flip angles.

After a pulse duration that causes a 90-degree flip angle, the net magnetization lies in the transverse plane and it precesses around the \mathbf{B}_0 axis at the Larmor frequency. The magnetization induces an AC current in a receiver coil, as depicted in Figure 2.3.

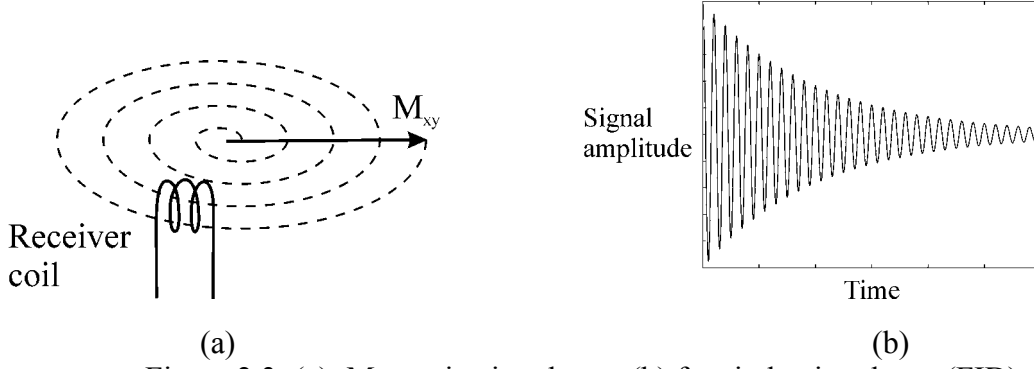


Figure 2.3: (a): Magnetization decay, (b) free induction decay (FID).

This current oscillates with Larmor frequency and it decays exponentially as $\exp(-t/T_2^*)$. This is known as the free induction decay (FID). The signal decay is due to a process known as a relaxation, whose time constant T_2^* is explained in Section 2.3.

2.3 Relaxation

At equilibrium, the net magnetization is aligned along the longitudinal axis (\mathbf{B}_0 axis). It means that the equilibrium magnetization in the transverse plane is zero. The relationship describing the decay is:

$$M_{\text{transverse}} = M_{\text{transverse}}^0 e^{-t/T_2^*}, \quad (2.2)$$

where $M_{\text{transverse}}^0$ is the initial transverse magnetization. T_2^* characterizes the rate of decay. There are several mechanisms contributing to the transverse decay: spin-spin T_2 relaxation, B_0 field inhomogeneity $T_{2,\text{inhomo}}$, susceptibility $T_{2,\text{suscept}}$, and diffusion $T_{2,\text{diff}}$, etc.:

$$\frac{1}{T_2^*} = \frac{1}{T_2} + \frac{1}{T_{2,\text{inhomo}}} + \frac{1}{T_{2,\text{suscept}}} + \frac{1}{T_{2,\text{diff}}} + \dots \quad (2.3)$$

For the longitudinal relaxation we have a different mechanism described by:

$$M_{\text{longitudinal}} = M_{\text{longitudinal}}^0 \left(1 - e^{-t/T_1}\right), \quad (2.4)$$

where T_1 is a longitudinal relaxation constant.

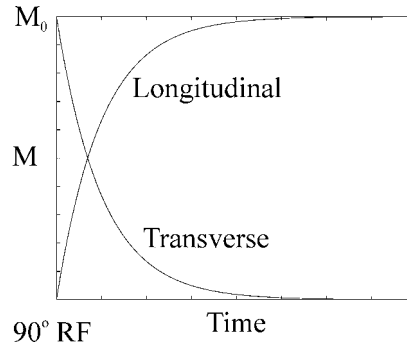


Figure 2.4: Qualitative transverse and longitudinal relaxation behavior after the 90° pulse is turned off.

2.4 Magnetic Field Gradients

The magnetic field can be modified through the application of spatially varying magnetic fields, so-called gradient fields. Since

$$\gamma B = f, \quad (2.5)$$

the resonance frequencies of protons will vary along the gradient axis. Since we can measure frequencies and we know the imposed spatial variation of magnetic field, the positions of resonating protons can be determined from their frequencies.

$$f = \gamma(B_0 + rG_r), \quad (2.6)$$

where r is the position along r -axis (x , y , or z) and G_r is the corresponding gradient field.

2.5 Slice Selective Excitation

The signal response in the third spatial dimension needs to be restricted. This is accomplished by selectively exciting only spins in a well-defined slice of tissue within the

imaging volume. This is achieved by imposing a gradient along an axis perpendicular to the chosen slice plane, which causes a linear variation of resonance frequencies along that axis. As shown in Figure 2.5, a sinc-shaped RF pulse excites a band of frequencies of width $\Delta f = 1/\tau$ around the center frequency f_0 .

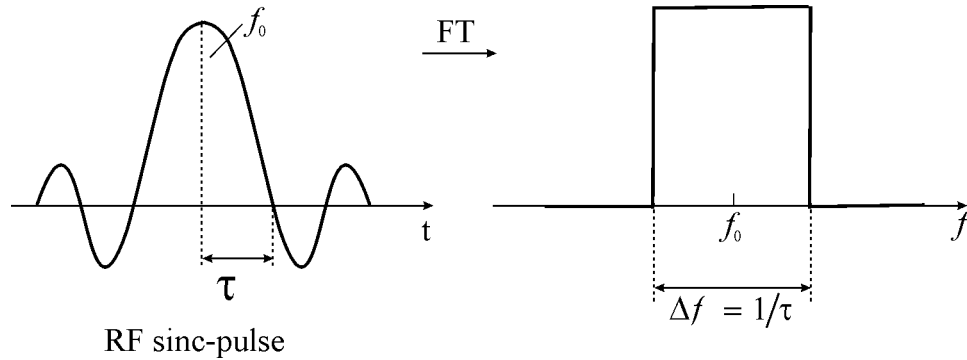


Figure 2.5: Fourier transform correspondence of the sinc function.

The thickness of the excited slice d is related to the gradient amplitude G and RF bandwidth Δf as follows:

$$\Delta f = \gamma G d . \quad (2.7)$$

This equation determines slice thickness to be excited. The location of this slice can be found from the center frequency of the RF sinc-pulse via an offset location z_{offset} :

$$\Delta f_0 = \frac{z_{offset} \cdot \Delta f}{d} . \quad (2.8)$$

If the center frequency is equal to the resonance frequency of protons in the absence of gradient, then the excited slice is in the isocenter ($z = 0$) of the magnet system.

2.6 Frequency Encoding

The next task is encoding the image information within the excited slice. The image information source is actually the amplitude of the MR signal arising from the various locations in the slice. Two distinct processes are used for encoding the two dimensions: frequency encoding and phase encoding. Frequency encoding will be discussed first.

Imposition of a gradient along one of the two principal axes of the plane during the period when the receiver coil is on, causes the signal received to be an interference pattern arising from various precessional frequencies of the spins along the gradient axis.

A signal is acquired in the presence of the read-out (frequency-encoding) gradient. Another gradient pulse, termed a “dephaser”, is also implemented along the frequency encoding axis. Area of the dephaser gradient pulse is one-half that of the read gradient. The field of view along the frequency axis (FOV_f) can be found from:

$$\gamma G_x FOV_f = BW, \quad (2.9)$$

where G_x is the amplitude of the frequency-encoding gradient.

2.7 Phase Encoding and Image Acquisition

In order to produce a two-dimensional image of the slice, one can cause a systematic variation in phase, which would encode the spatial information along the one remaining principal axis of the image plane. The sampling theorem needs to be used for phase encoding. At positions between the two edges of field of view in the phase encoding dimension (FOV_p) the phase should change by less than 180° . Quantitatively, we can write:

$$\gamma G_x FOV_p T_p = N_p \pi, \quad (2.10)$$

where T_p is the length of the phase-encoding pulse, N_p is the number of phase-encoding pulses.

The phase encoding is not on within the acquisition window; it cannot affect the detected frequencies. The complete pulse sequence (Figure 2.6) is played out many times and the resulting signals are stored separately.

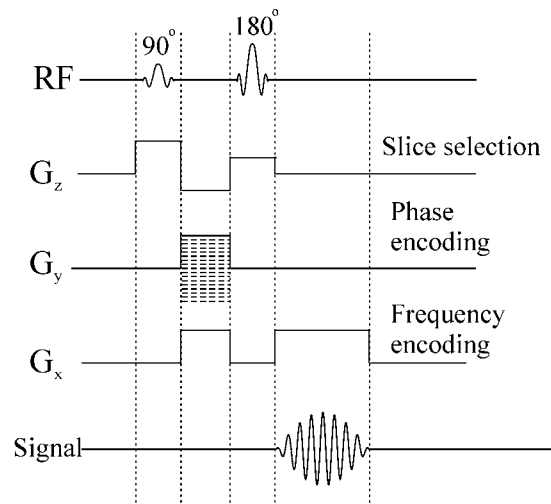


Figure 2.6: Spin-echo pulse sequence.

The only variation from one acquisition to the next is the amplitude of the phase encoding gradient, which is changed in a step-wise fashion. Collection of MR data from the slice yields a set of spin echoes (views). This dataset is also known as k -space (Figure 2.7(b)).

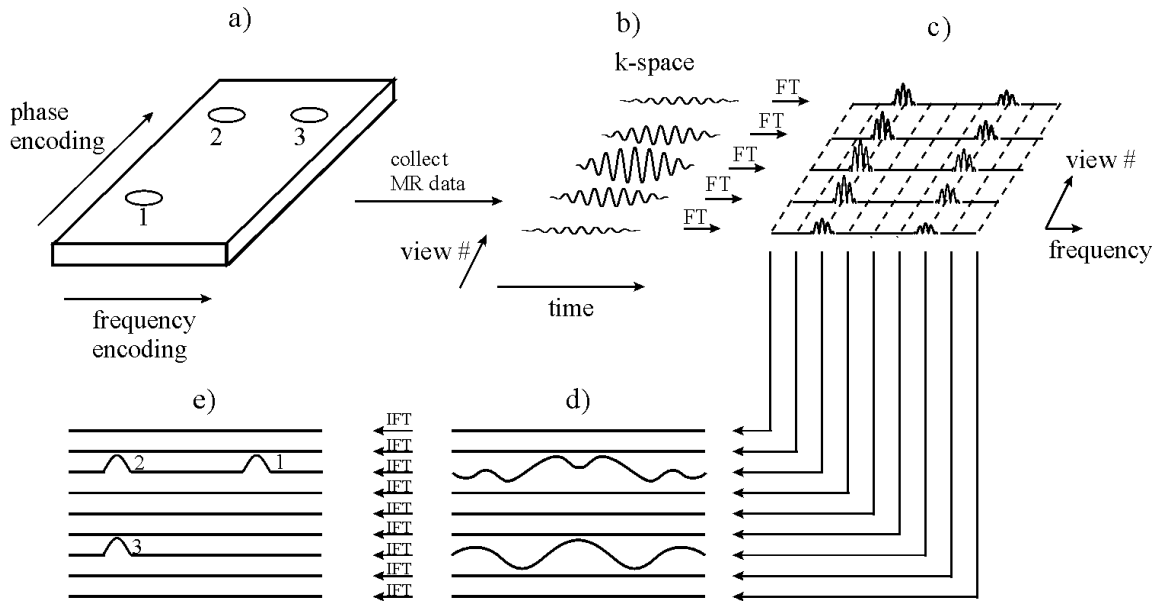


Figure 2.7: Schematic representation of image formation via the Fourier Transform (FT and IFT denote, respectively, the forward and inverse Fourier Transform).

Separate Fourier transformation of each of these data sets (views) yields a set of projections onto the read axis (Figure 2.7(c)). These projections are identical with respect to frequency, but not with respect to phase.

A data set consisting of the first point from every projection is constructed and subjected to the Fourier transform. Another data set is assembled from the second point of every projection, Fourier transformed and stored separately, and so on. This gives rise to the data set shown in Figure 2.7(d).

Fourier Transform of this data set produces a new data representation shown in Figure 2.7(e). After being transposed this data set represents the image of the slice.

Chapter 3

G_y Surface Gradient Coil

3.1 Design Goal and Quality Assessment

As previously discussed, linear and strong magnetic gradient fields are indispensable for high-resolution imaging of biological tissue. Goal of this dissertation is to design an effective surface gradient coil configuration (Figure 3.1) in a pre-described plane. Effectiveness in this context is understood as the ability to provide a strong gradient field, while at the same time minimizing the parasitic gradients within the region of interest (ROI).

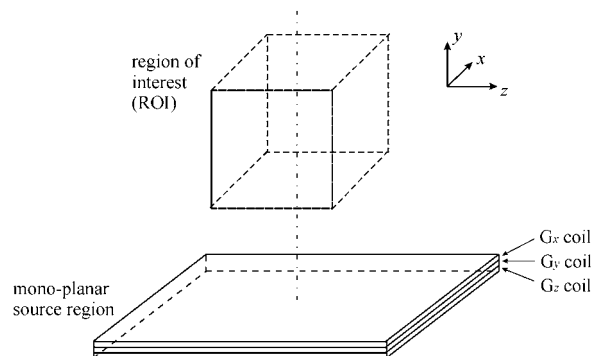


Figure 3.1: Conceptual arrangement of three mono-planar surface gradient coils situated below the region of interest (ROI).

For the subsequent theoretical and practical coil considerations we need to define certain criteria that greatly facilitate the comparison of the various coil designs. In particular, three criteria are needed:

- Gradient strength. Obviously the image resolution improves if the gradient coil is able to produce a higher field magnitude for the same amount of input current.
- Field uniformity. Distortions in the image are minimized if the magnetic field is highly linear in the ROI. As discussed in Section 3.2, we can estimate the field uniformity visually from the magnetic field plots and from distortions of the image of the phantom that consists of several equidistant layers.
- Parasitic gradient field distribution. To assess the overall quality of the gradients (for example the G_y coil), a so-called coil quality factor Q can be defined as:

$$Q = \min_{\text{ROI}} \left(\frac{|G_y|}{\sqrt{G_x^2 + G_y^2 + G_z^2}} \right).$$

The coil, which has the highest Q , is preferred in the sense that it yields the lowest parasitic gradients.

3.2 Prior Art

One of the few mono-planar surface gradient coil designs was reported by Cho and Yi [14]. In their paper they describe a three-channel gradient set consisting of the G_x -, G_y - and G_z gradient coils. In Figure 3.2 the G_y surface gradient coil is depicted.

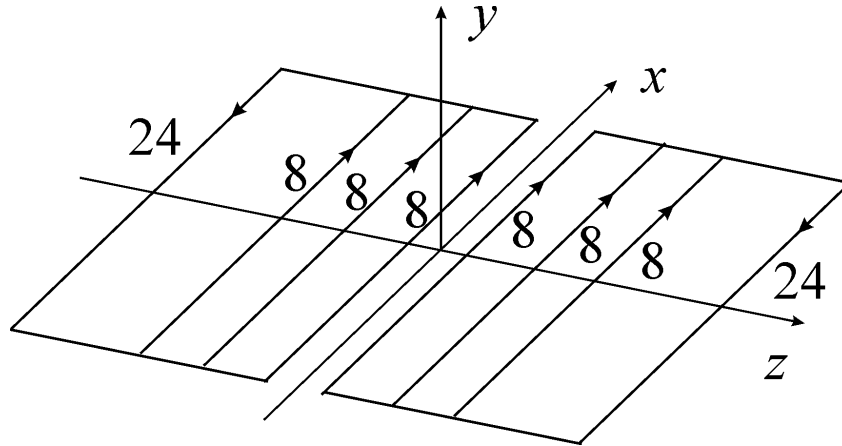


Figure 3.2: G_y gradient coil design as originally proposed by Cho and Yi [14].

In Figure 3.3 we have computed the z -component of the magnetic flux density based on Biot-Savart's law and for a normalized input current of $i = 1A$.

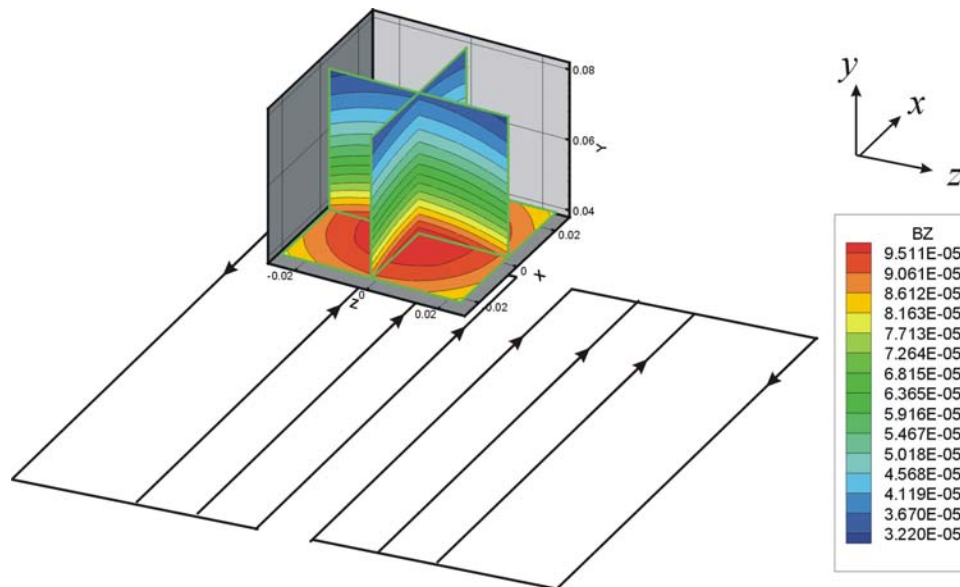


Figure 3.3: Magnetic flux density B_z in units of [T] for both the transversal and longitudinal direction throughout the ROI. The ROI is located 4 cm above the coil plane and ranges from 4 to 8 cm in y direction and from -2.5 to $+2.5$ cm in z and x directions, respectively.

We observe that the magnetic field exhibits parasitic gradients in x and z -directions. This is more clearly seen in Figure 3.4 where we again show the axial and sagittal slices taken through the center of the ROI.

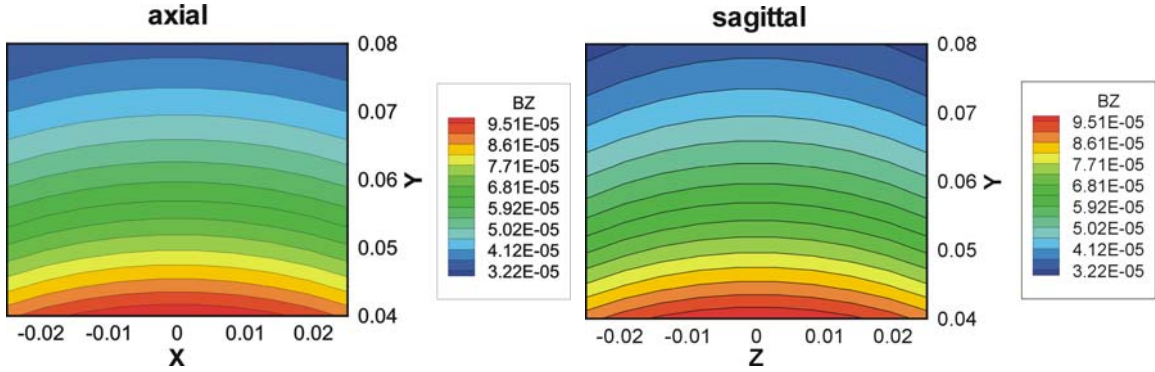


Figure 3.4: Contours of magnetic flux density B_z in units of [T] in axial and sagittal cross-sections through the ROI. The spatial dimensions in x, y, z directions are given in [m].

Since nonlinear field distributions result in image distortions, it is important to visualize the exact extent of the magnetic field behavior. As we see in Figure 3.4, points having the same value of the magnetic field are located on slightly curved contour lines (magnitude level of the magnetic field). The underlying MRI Fourier space reconstruction approach treats points that have the same field level as belonging to the same y -coordinate. In fact, those points of constant magnetic field values in Figure 3.4 would become straight, equidistant lines after Fourier space reconstruction. In order to assess the degree of distortion, it is advantageous to plot the y -coordinate values within the ROI in a new (z, x, B_z) coordinate representation. In other words, we consider y as a function of x and B_z . Thus, we can associate values of B_z with a new coordinate y^* (the y -coordinate after Fourier space reconstruction) such that:

$$y^* = 0.04 + \frac{0.08 - 0.04}{B_z(y = 0.08) - B_z(y = 0.04)} [B_z - B_z(y = 0.04)] \text{ [m]}.$$

y^* depends linearly on B_z . Indeed, we can now plot y in a (z, x, y^*) coordinate representation. Contours of constant y reveal the extent of how straight lines in the ROI are distorted after Fourier space reconstruction for a particular G_y coil design. As an example, the G_y coil designed by Cho [14] yields a simulated reconstruction image as shown in Figure 3.5.

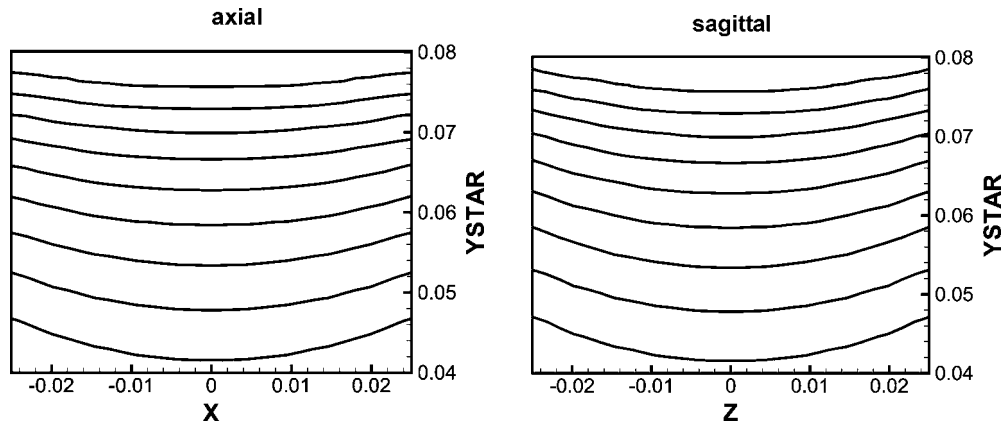


Figure 3.5: Simulations of the reconstructed image produced by the G_y gradient coil designed by Cho [14] with levels of y in terms of (z, x, y^*) coordinates. Here y^* (or YSTAR) is the predicted y -coordinate after Fourier space reconstruction. All spatial dimensions are recorded in [m].

As we see from Figure 3.5, the space within the ROI closest to the coil appears to be significantly expanded and curved.

In addition, as a single figure of merit we can also employ the coil quality factor Q to assess the overall G_y performance. Calculating Q for the coil designed by Cho, we obtain $Q=0.867$. This coil was built using a plastic former (of thickness 4mm) and wiring of AWG-20 (American Wire Gauge) copper wires. The wire pattern was wound around a suitable arranged template of metal pegs mounted on a wooden plate, before

transferring it into the plastic former with milled grooves. The wire pattern is spatially fixed within the grooves by using an epoxy resin. A photograph of the finished G_y coil is seen in Figure 3.6.

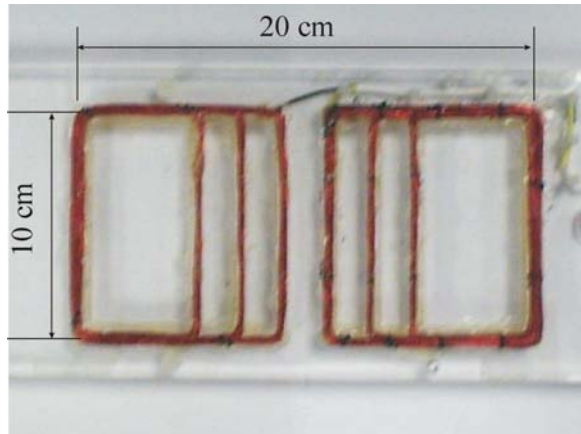


Figure 3.6: Fabrication of prior art G_y gradient coil [14].

This particular wire arrangement forms the baseline for subsequent comparisons against our new, improved coil designs. This coil has an inductance and resistance of $L = 0.315 \text{ mH}$ and $R = 0.54 \Omega$, respectively. The actual coil was benchtested using a specially designed nonmagnetic, plastic holder, as depicted in Figure 3.7(a). Based on an applied DC current of 1A the magnetic field in the ROI was measured with a Hall sensor attached to a Gaussmeter (see Figure 3.7 (b)).

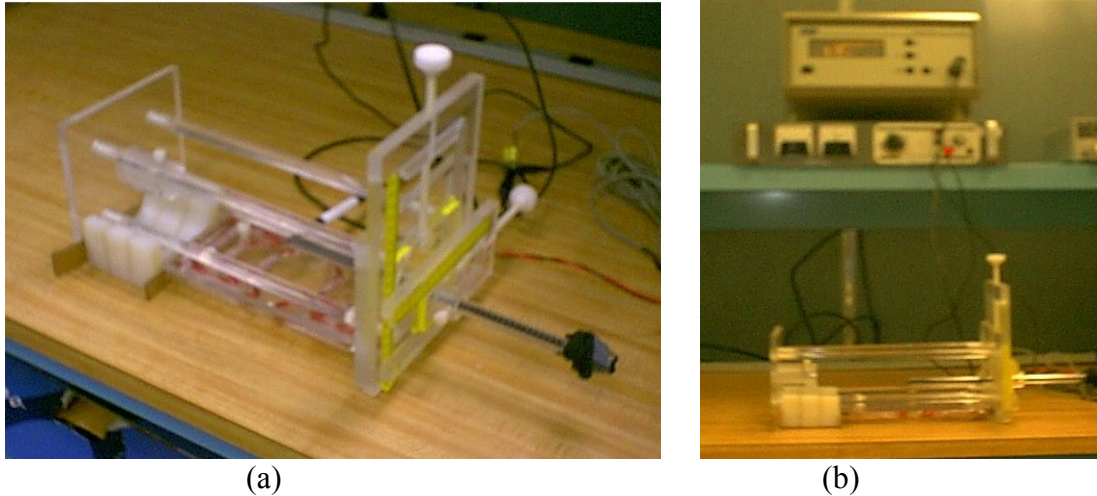


Figure 3.7: (a) G_y coil [14] in a Plexiglas restrainer, (b) experimental setup for bench testing.

The magnetic field of the coil in an axial, or xy , plane was measured and plotted in Figure 3.8.

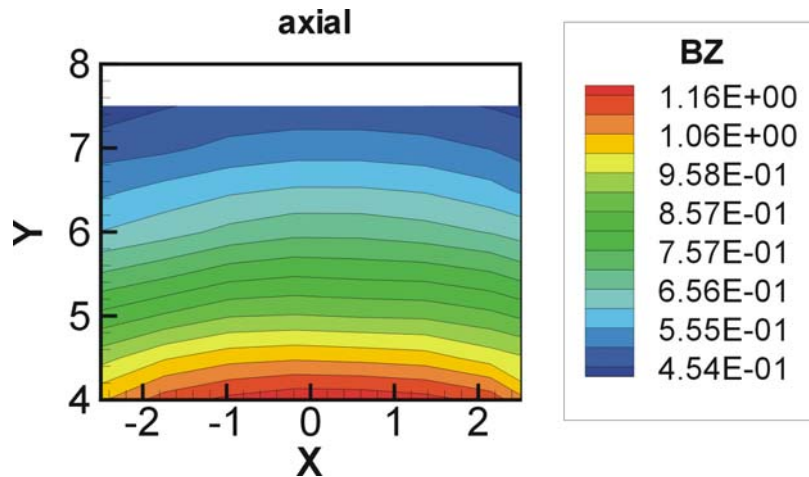


Figure 3.8: Measured transversal magnetic flux density B_z in [G] recorded for the G_y gradient coil as proposed in [14], and based on a drive current of 1A. Spatial dimensions are recorded in [cm].

The above G_y coil arrangement was tested in a GE CSI-II 2.0 T 45-cm imaging spectrometer operated at 85.56 MHz and residing within a commercial, self-shielded

gradient set. The G_y coil was placed in the 5mm thick Plexiglas plastic tube and fastened with plastic screws as shown in Figure 3.9.

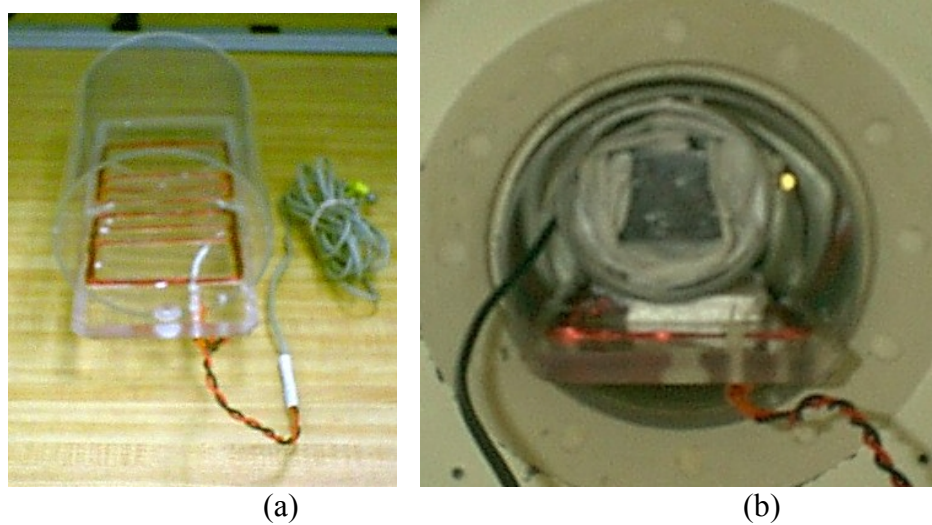


Figure 3.9: Original G_y coil: (a) on the bench, placed in a Plexiglas cylindrical tube of 15cm diameter, (b) located inside the MR system.

In addition to the G_y surface coil a custom-built 12-element low-pass RF bird-cage coil of 10 cm diameter was fastened on the coil plane. Inside the RF coil a Plexiglas phantom of 5.0 cm width (x -direction), 5.0 cm length (z -direction), 3.9 cm height was positioned, see Figure 3.10. The phantom has six water filled compartments, each 3 mm in thickness. The compartments are separated by 3 mm thick Plexiglas layers. Epoxy resin was used to provide reliable adhesion between different parts of the phantom.

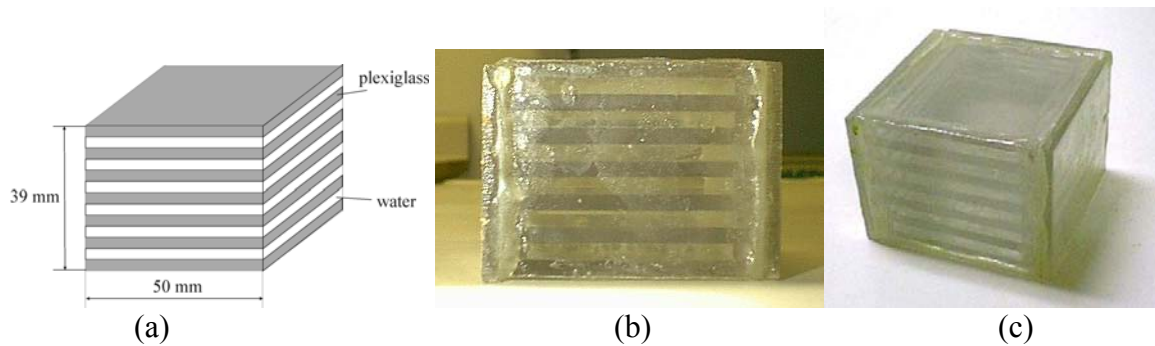


Figure 3.10: Picture and photographs of the phantom: (a) phantom schematics, (b), (c) different views of phantom. Each water compartment is 3mm in thickness.

After inserting the coil within the main magnet, which was equipped with a three-channel GE gradient, the following steps were carried out:

- a) The gradient amplifier cable link leading to the GE G_y channel was disconnected and attached to the G_y surface gradient coil.
- b) The resistance ($R=33.4 \text{ k}\Omega$) and capacitance ($C=3.17 \text{ nF}$) values within the feedback control loop at the output stage of the G_y gradient amplifier were adjusted so as to compensate for the induced eddy current influence. The numerical values were selected such that an applied rectangular pulse sent to the G_y surface coil was reproduced with minimal under- and over-swings, as observed through an attached oscilloscope.
- c) A spin echo pulse sequence was selected with $TR/TE = 2000/20 \text{ ms}$ (where TR is the repetition time, and TE is the echo time). Here, the y -direction was used for frequency encoding. For axial imaging we used the z -axis for slice selection and the x -axis for phase encoding. For sagittal slices the selection

was changed as follows: the x -axis for slice selection and the z -axis for phase encoding.

Figure 3.11 depicts the images obtained from the phantom in the axial and sagittal planes.

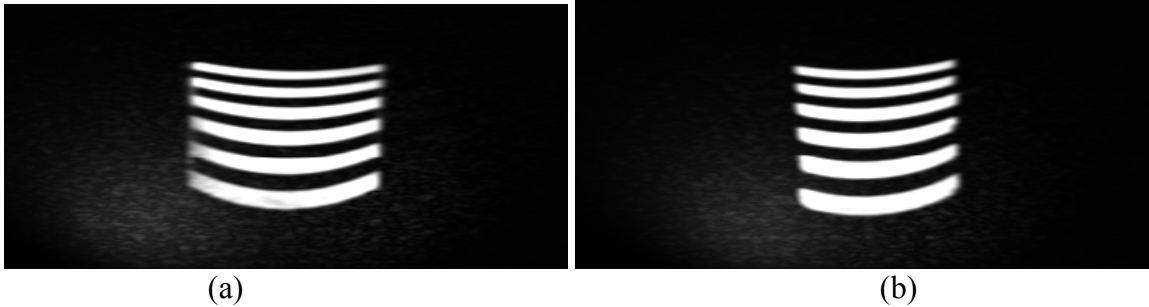


Figure 3.11: Resulting images obtained from the Plexiglas phantom of Figure 3.10 with Cho's G_y surface coil. The coil plane resides 4.3 cm below the first water contour: (a) axial plane, (b) sagittal plane.

Clearly observable are the image distortions both in terms of undesirable curvature and non-uniform thickness layers. These results form the basis of improving the designs by modifying the current flow so as to maximize the gradient uniformity. To improve upon these images, the following sections outline the theoretical approach, the fabricated coils, and the resulting images.

3.3 Theoretical Least Squares Formulation

In order to significantly improve upon the existing surface gradient coil design, we devised a mathematical formulation that determines the optimal current distribution in a given coil plane based on a prescribed magnetic field and given ROI. The subsequent sections outline the steps required to formulate this theoretical model and to arrive at an optimal current distribution.

We consider an excitation current density $\mathbf{j}(z, x)$ residing in the z - x plane. The uniplanar coil region is restricted to the following spatial dimensions: $[z_{min}, z_{max}, x_{min}, x_{max}] = [-0.1m, 0.1m, -0.05m, 0.05m]$.

The overall size is dictated by the bore size of the main magnet. We next consider a cubical ROI with the following dimensions:

$$[z_{min}, z_{max}, x_{min}, x_{max}, y_{min}, y_{max}] = [-0.025m, 0.025m, -0.025m, 0.025m, 0.04m, 0.08m],$$

which is sufficient for cranial imaging of small animals such as rats and other rodents.

Our goal is to find the current density $\mathbf{j}(z, x)$ that yields a desired magnetic field distribution $B_{z,des}(z_o, x_o, y_o)$ inside a predefined region of interest (ROI) as depicted in Figure 3.1. Starting point is the Biot-Savart law in the form:

$$\mathbf{B}(\mathbf{r}_o) = \frac{\mu_0}{4\pi} \int \frac{\mathbf{j} \times \mathbf{r}}{r^3} dS_s, \quad (3.1)$$

where $\mathbf{r} = \mathbf{r}_o - \mathbf{r}_s$ and $r = |\mathbf{r}|$. Vector \mathbf{r}_o points to the coordinates of the observation point residing inside the ROI, and \mathbf{r}_s are the coordinates of the unknown excitation source. Since we are interested in the z -component of the B-field, we consider only the x -component of the surface current density $\mathbf{j}(z, x)$. Thus, (3.1) is re-written as:

$$B_z(\mathbf{r}_o) = \frac{\mu_0}{4\pi} \int \frac{\hat{\mathbf{x}} \times \mathbf{r}}{r^3} j_x(z, x) dS_s = \frac{\mu_0}{4\pi} \int \frac{y_o}{|\mathbf{r}_o - \mathbf{r}_s|^3} j_x(z, x) dS_s, \quad (3.2)$$

where $\hat{\mathbf{x}}$ is a unit vector in x -direction and S_s is the surface of the source. Explicitly, the flux density takes on the form:

$$B_z(z_o, x_o, y_o) = \frac{\mu_0}{4\pi} \int_{x_{min}}^{x_{max}} \int_{z_{min}}^{z_{max}} \frac{y_o}{[y_o^2 + (x_o - x)^2 + (z_o - z)^2]^{3/2}} j_x(z, x) dz dx. \quad (3.3)$$

Since the sum of the inflowing coil current has to equal the sum of the exiting current, a constraint condition can be imposed on $j_x(z, x)$, i.e.,

$$\int_{z_{min}}^{z_{max}} j_x(z, x) dz = 0 \quad (3.4)$$

for all values of x . We next approximate this current density $j_x(z, x)$ by a generic set of basis functions $f_n(z, x)$, $n = 1, \dots, N$ such that

$$j_x(z, x) = \sum_n^N I_n f_n(z, x). \quad (3.5)$$

Here I_n are constants to be determined. Inserting (3.5) into (3.3) yields:

$$B_z(z_o, x_o, y_o) = \frac{\mu_0}{4\pi} \sum_n^N I_n \int_{x_{min}}^{x_{max}} \int_{z_{min}}^{z_{max}} \frac{y_o f_n(z, x)}{\left[y_o^2 + (x_o - x)^2 + (z_o - z)^2 \right]^{3/2}} dz dx. \quad (3.6)$$

Written in more compact notation we see that

$$B_z(z_o, x_o, y_o) = \sum_{n=1}^N I_n K_n(z_o, x_o, y_o), \quad (3.7)$$

where K_n is given by:

$$K_n(z_o, x_o, y_o) = \frac{\mu_0}{4\pi} \int_{x_{min}}^{x_{max}} \int_{z_{min}}^{z_{max}} \frac{y_o f_n(z, x)}{\left[y_o^2 + (x_o - x)^2 + (z_o - z)^2 \right]^{3/2}} dz dx. \quad (3.8)$$

We next establish a functional Φ that relates the computed field B_z to the desired field $B_{z,des}$. Specifically,

$$\begin{aligned} \Phi = & \frac{1}{2} \iiint_{ROI} W(z_o, x_o, y_o) \cdot \left[B_z(z_o, x_o, y_o) - B_{z,des}(z_o, x_o, y_o) \right]^2 dz_o dx_o dy_o \\ & + \int_{x_{min}}^{x_{max}} \lambda(x) \int_{z_{min}}^{z_{max}} j_x(z, x) dz dx. \end{aligned} \quad (3.9)$$

Here, $W(z_o, x_o, y_o)$ is an arbitrarily chosen weight function and λ is a Lagrange multiplier. As discussed below, by appropriately selecting this function we can affect gradient uniformity.

Our goal is to find $B_z(z_o, x_o, y_o)$ that minimizes the functional Φ . This is accomplished by setting the derivative to zero with respect to the unknown currents, i.e.,

$$0 = \frac{\partial \Phi}{\partial I_{n'}} = \iiint_{ROI} \mathcal{W}(z_o, x_o, y_o) \cdot \left[\sum_n I_n K_n(z_o, x_o, y_o) - B_{z,des}(z_o, x_o, y_o) \right] K_n(z_o, x_o, y_o) dz_o dx_o dy_o + \int_{x_{min}}^{x_{max}} \lambda(x) \int_{z_{min}}^{z_{max}} f_n(z, x) dz dx \quad (3.10)$$

for $n' = 1 \dots N$. For $0 = \frac{\partial \Phi}{\partial \lambda}$ we have:

$$0 = \sum_n I_n \int_{z_{min}}^{z_{max}} f_n(z, x) dz \quad \text{for all } x. \quad (3.11)$$

Equations (3.10) and (3.11) can also be represented as a system of linear equations in compact notation:

$$\mathbf{AX} = \mathbf{b}. \quad (3.12)$$

Solving this system yields the solution vector \mathbf{X} that contains the discrete current elements I_n , $n = 1, \dots, N$, and λ .

We now consider a special choice of basis functions: function f_{mn} is zero everywhere except that it behaves like a δ -function, $\delta(z - z_m)$, over the interval $(z_m, x_n^-) - (z_m, x_n^+)$, see Figure 3.12.

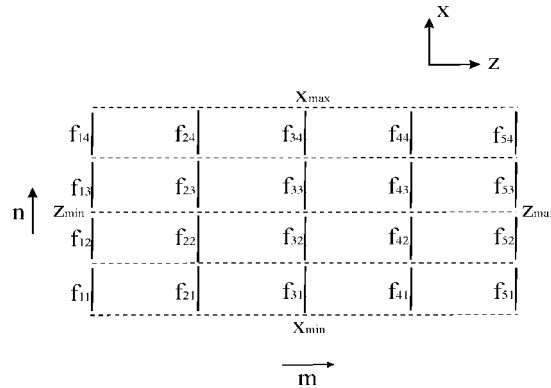


Figure 3.12: Set of basis functions f_{nm} chosen for the proposed least squares method.

In this case the functional takes on the form:

$$\Phi = \frac{1}{2} \iiint_{ROI} W(z_o, x_o, y_o) \cdot [B_z(z_o, x_o, y_o) - B_{z,des}(z_o, x_o, y_o)]^2 dz_o dx_o dy_o + \sum_n^N (\Delta x \lambda_n) \left(\sum_m I_{mn} \right). \quad (3.13)$$

The last term follows from the limitation that we imposed on surface current. Due to the delta function representation for the basis function, (3.8) simplifies to:

$$K_{mn}(z_o, x_o, y_o) = \frac{\mu_0}{4\pi} \int_{x_n^-}^{x_n^+} \frac{y_o}{[y_o^2 + (x_o - x)^2 + (z_o - z_m)^2]^{3/2}} dx. \quad (3.14)$$

The resulting system of equations (3.12) has the following coefficients for matrix **A** and column vector **b**:

$$A_{M(n'-1)+m', M(n-1)+m} = \sum_{mn} \iiint_{ROI} W(z_o, x_o, y_o) K_{mn}(z_o, x_o, y_o) K_{m'n'}(z_o, x_o, y_o) dz_o dx_o dy_o$$

for $m, m' = 1, \dots, M$, $n, n' = 1, \dots, N$,

and

$$A_{M(n'-1)+m', MN+n'} = 1, \quad \text{for } m' = 1, \dots, M, \quad n' = 1, \dots, N, \quad (3.15)$$

$$A_{MN+n', i} = 1, \quad \text{for } i = 1 + M(n'-1), \dots, Mn', \quad n' = 1, \dots, N,$$

$$b_{M(n'-1)+m'} = \iiint_{ROI} W(z_o, x_o, y_o) K_{m'n'}(z_o, x_o, y_o) B_{z,des}(z_o, x_o, y_o) dz_o dx_o dy_o,$$

$m' = 1, \dots, M, \quad n' = 1, \dots, N.$

Vector **X** is comprised of the elements:

$$X_{M(n'-1)+m'} = I_{m'n'} \quad \text{where } m' = 1, \dots, M, \quad n' = 1, \dots, N,$$

$$X_{MN+n'} = \Delta x \lambda_{n'} \quad \text{where } n' = 1, \dots, N. \quad (3.16)$$

Solving (3.12) either directly (Gauss elimination) or iteratively (conjugate gradient method) for the unknown currents I_{mn} yields the discrete current elements (magnitude and direction). After scaling these currents into integer values we obtain the direction and discrete strength of each segment that should be placed into the grooves of the planar former. Dictated by practical considerations, the discrete numbers of wires should not exceed 25 so as to maintain appropriate compactness.

3.4 Design of G_y Gradient Coils Based on the Least Squares

Method

In what follows, the above outlined mathematical design methodology is employed to construct two novel surface gradient coil wire patterns with superior field strength and field uniformity. Although the approach was done for the construction of the G_y coil only, a completely analogous approach can be done for the G_x and G_z surface coils.

(a) G_y gradient coil with $m=5$ and $n=4$ (labeled as 5×4 G_y gradient coil)

At first we have chosen a configuration with $m=5$ and $n=4$, depicted in Figure 3.12. After solving Eq. (3.12) for the unknown currents, we arrive at the discrete current distributions within the generic layout pattern depicted in Figure 3.12. The actual layout is displayed in Figure 3.13.

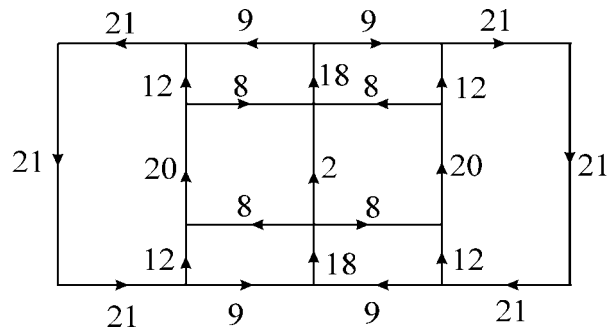


Figure 3.13: New 5×4 G_y gradient coil design. The discrete numbers denote the wires placed in each groove.

In Figure 3.13, the integers denote the number of wire segments carrying current in the indicated directions. The field produced by this coil is represented in Figure 3.14.

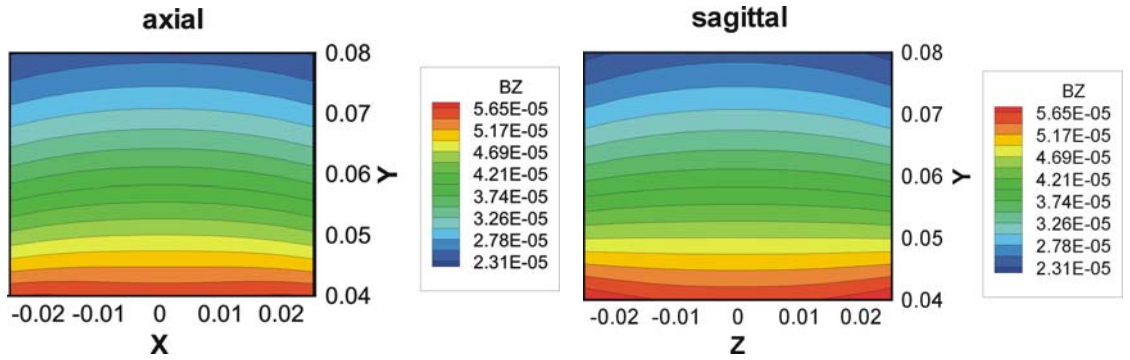


Figure 3.14: Magnetic flux density in [T] for the $5 \times 4 G_y$ gradient coil. All spatial dimensions are given in [m].

Theoretically predicted image distortions of the phantom placed within the coil's ROI are based on our earlier discussion and are shown in Figure 3.15. We notice compression in the upper layers (due to non-linear flux distribution) and curvature (due to parasitic field distribution).

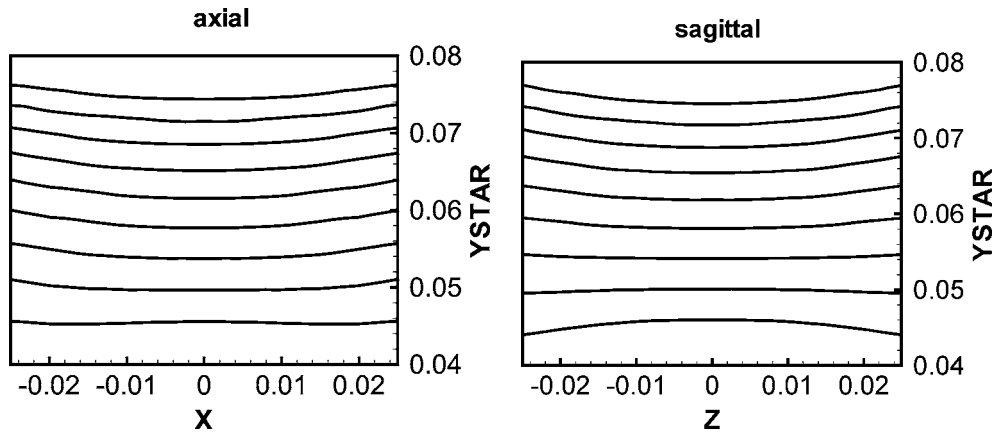


Figure 3.15: Simulations of the reconstructed image produced by the $5 \times 4 G_y$ gradient coil. All spatial dimensions are given in [m].

In terms of the coil's figure of merit we obtain: $Q=0.908$, which represents a significant improvement over $Q=0.867$, the baseline coil developed by Cho [14].

(b) G_y gradient coil with $m=6$ and $n=4$ (labeled as $6 \times 4 G_y$ gradient coil)

As a second example, a configuration with $m=6$, $n=4$ is considered. Using the least squares method we obtain the wire distribution shown in Figure 3.16.

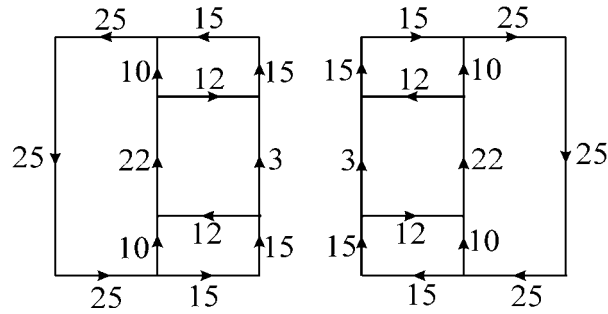


Figure 3.16: A $6 \times 4 G_y$ gradient coil wire pattern.

Here again, the integers in Figure 3.16 denote the number of wire elements and the direction of current flow is depicted by arrows. The corresponding field produced by this coil is represented in Figure 3.17.

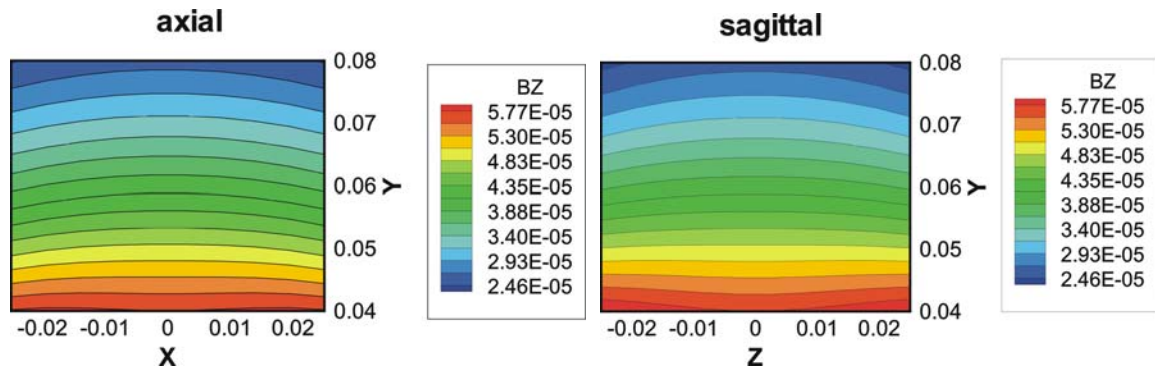


Figure 3.17: Magnetic flux density B_z in [T] of the $6 \times 4 G_y$ gradient coil. All spatial dimensions are in [m].

Figure 3.18 provides numerical predictions of the anticipated axial and sagittal distortions within the ROI.

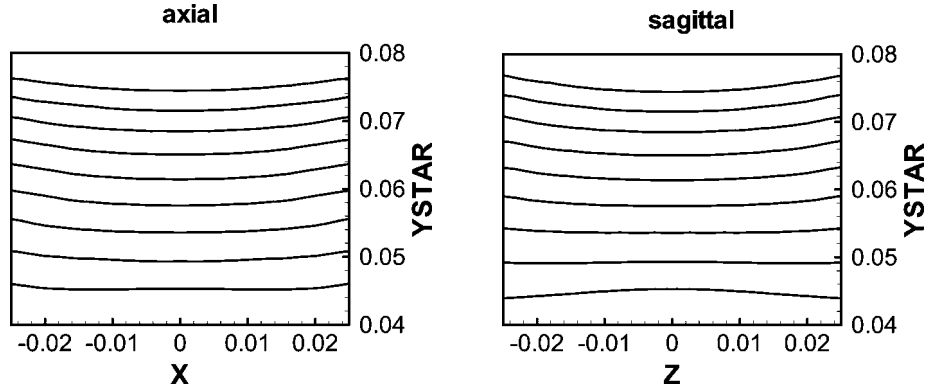


Figure 3.18: Simulations of the expected image reconstruction produced by the 6×4 G_y gradient coil shown in Figure 3.16. All spatial dimensions are in [m].

We will next compare the strength of the surface gradient coils in the center of the region of interest as well as their respective quality factor for all three coils described above. Table 1 reports the maximum field strength in the center of the ROI and the Q factor as defined in Section 3.1.

From Table 1 we notice that the 5×4 and 6×4 coils yield better magnetic field uniformity. As a result, the obtained images of the phantom are significantly less distorted. However, the gradient strengths produced by these coils are weaker than the gradient strength of the one reported in [14].

Table 1: Gradient strengths, resistances and quality factors of three mono-planar G_y surface gradient coils.

Design	G_y [G/cm/100A] (recorded at height $y=6$ cm)	R , [Ω]	Q
Cho <i>et al.</i> [14] (maximum 24 wires)	15.50	0.54	0.867
5×4 G_y gradient coil	8.14	0.52	0.908
6×4 G_y gradient coil	8.26	0.61	0.915

It is interesting to point out that the 5×4 and 6×4 coils feature current elements that are generally farther away from the ROI. This allows the magnetic field to be made more

uniform at the expense of field strength. However, as explained below, the trade-off between field strength and field uniformity can be mitigated somewhat.

3.5 Additional Performance Improvements

There are certain design constraints that are difficult to overcome by using the least squares method. As noted, coils generated by this method do not yield high gradient strengths. Increasing the number m and n results in higher field uniformities, but also lower gradient strengths. Moreover, the practical coil fabrication becomes increasingly difficult for coils with high numbers of m and n . Consequently, it is desirable to develop an alternative, more effective approach for the surface coil design.

Towards this end, we can introduce several basic restrictions to avoid making the design excessively cumbersome. Specifically:

- (a) The coil should be simple to build,
- (b) The number of wires in each groove should not exceed a value of 25,
- (c) The current-carrying wires (grooves) should not intersect,
- (d) The neighboring grooves should not be closer than 1 cm from each other, and
- (e) The sharp angles at the coil nodes should be avoided.

Obviously, these conditions are difficult, if not impossible, to implement in terms of a simple least squares design method. However, the results obtained by this method along with previous designs can provide us with a hint as to how to place the wires in order to achieve a better gradient field. Our first goal is to consider a template as shown in Figure 3.19.

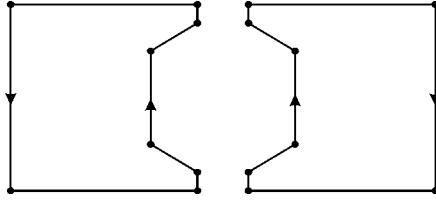


Figure 3.19: A G_y gradient coil prototype.

This design considers two loops, each carrying 24 wires. We immediately notice a significant amount of unused space inside each loop. By placing additional wire configurations inside these loops, we will be able to (i) improve the field strength, and (ii) have more freedom to improve the field quality factor (i.e., lower the parasitic gradients). The nodal coordinates were optimized by a trial-and-error method, resulting in a design depicted in Figure 3.20. We did not use any numerical optimization technique because it would be impossible to comply with all the restrictions listed above.

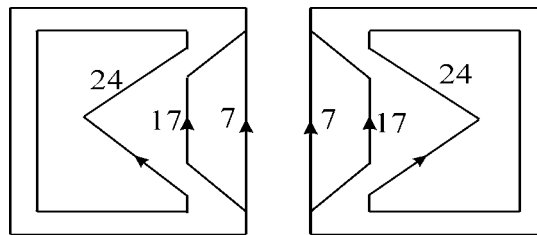


Figure 3.20: Six-loop coil G_y gradient coil.

The corresponding magnetic field simulations produced by this G_y coil are depicted in Figure 3.21.

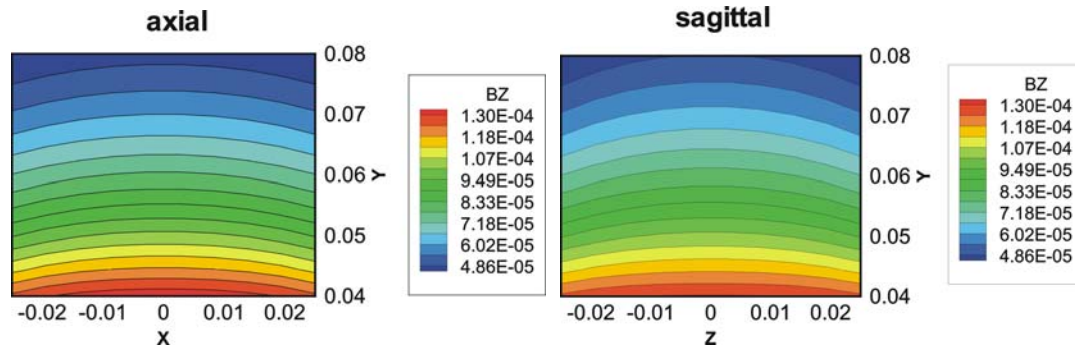


Figure 3.21: Magnetic field B_z in [T] for the six-loop, G_y gradient coil. All spatial dimensions are recorded in [m].

Examining the predicted distortions for a phantom placed within the ROI is shown in Figure 3.22 both for the axial and sagittal planes.

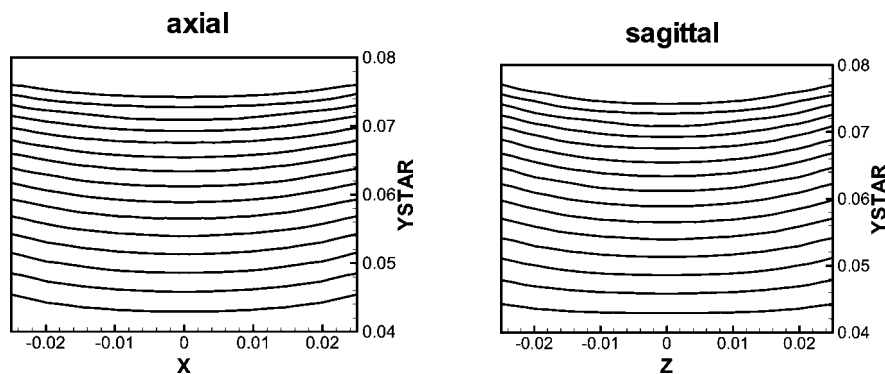


Figure 3.22: Simulations of the reconstructed image produced by the six-loop G_y gradient coil. All dimensions are listed in [m].

This coil yields a quality factor of $Q=0.880$. The system was constructed on a plastic former, as shown in Figure 3.23. Specifically, the G_y coil was wound on a planar 11 by 22 cm Garolite (G-10) former with machined grooves. To pre-shape the wire pattern, enamel-coated copper wire of AWG-20 size was wound on a template, prior to placing the pattern into the grooved former. An epoxy resin was used to fix the wire pattern within the former.

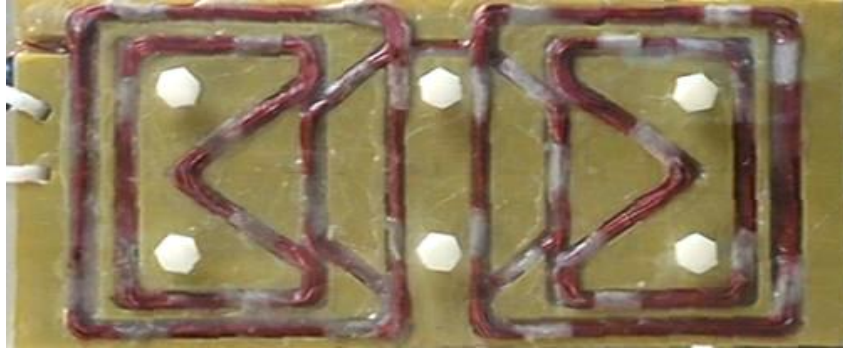


Figure 3.23: Six-loop G_y gradient coil.

Measurement of the inductive and resistive circuit parameters yield $L_s = 0.496$ mH and $R_s = 1.1 \Omega$, respectively.

This coil design was tested in a 4.7T Bruker MRI scanner with 40cm bore, shown in Figure 3.24. The resulting images from a phantom are depicted in Figure 3.25.



Figure 3.24: Photographs of the six-loop G_y coil placed in a 25 cm diameter Plexiglas tubular cylinder (left) and placed inside the 4.7T Bruker magnet with commercial gradient set (right).

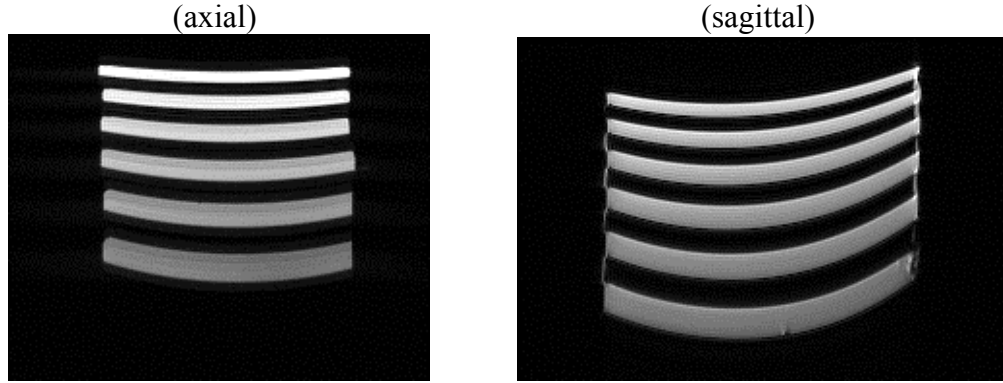


Figure 3.25: Resulting image of the phantom with the coil shown in Figure 3.23.

There is a key reason why the lower portion of sagittal image in Figure 3.25 appears distorted: it is difficult to measure precisely the distance between the coil plane and the lower edge of the phantom. The entire phantom in the experiment should have been positioned slightly closer to the coil than it was actually placed. The superior performance parameters of the six-loop G_y gradient coil both in terms of Q and field strength are summarized in Table 2.

Table 2: Gradient strength and quality factor of six-loop G_y surface gradient coil.

Design	G_y [G/cm/100A] (recorded at height $y=6$ cm)	R , [Ω]	Q
six-loop G_y gradient coil (maximum 24 wires)	20.80	1.10	0.880

Finally, Figure 3.26 depicts a comprehensive comparison of the various coil designs versus the Cho design [14] by displaying the strength of the magnetic field along the vertical axis passing through the center of the ROI:

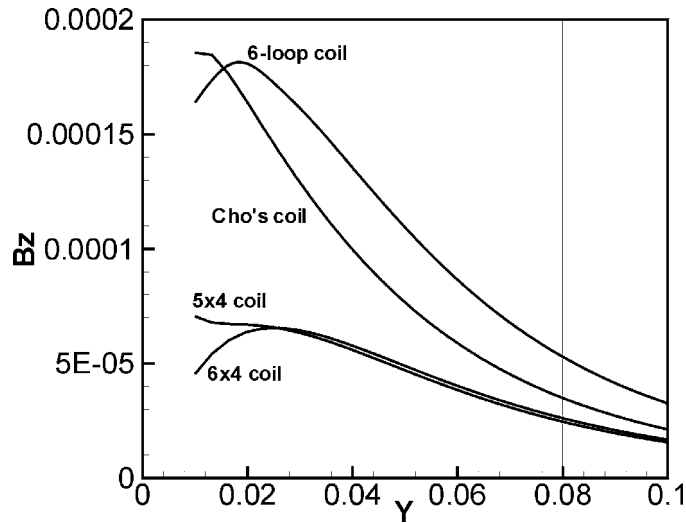


Figure 3.26: B_z -component of the magnetic flux density in [T] along the vertical line ($x=0$, $z=0$) passing through the ROI: Cho's design [14], 5x4 design, 6x4 design, and six-loop design. Spatial dimension is recorded in [m].

A set of preliminary experiments with a marmoset brain was performed in an effort to assess the image quality of a commercial encircling G_y coil (30.5-cm inner diameter Magnex gradient set of 68 mT/m, 220 μ sec rise time) versus the novel planar G_y coil. For the direct comparison, the six-loop coil was used without shim currents, and only minimal pre-emphasis current adjustment was applied to obtain the same rise time. The applied drive current for the six-loop coil was adjusted to a maximum of 20A, although currents of 100A can be achieved. Basic testing in the MR scanner confirmed the fact that shimming of the six-loop coil is not needed.

The following MR parameters are used for the image acquisition: spin-echo pulse sequence, TR/TE = 500/30 ms, FOV = 40 mm by 40 mm, 256x256 matrix size, slice thickness = 1.0 mm. Figures 3.27 – 3.28 display the transverse view of the cranial area. The slight asymmetry in the image observed with the six-loop coil is most likely due to

the fact the distance coil plane – center of ROI was larger than the targeted distance of 6cm.

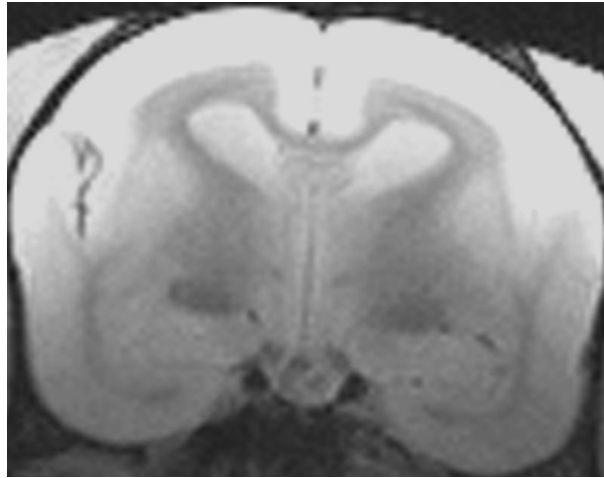


Figure 3.27: Commercial G_y gradient coil (Bruker high-performance gradient set, 26mm inner diameter, 5 G/cm at 100 A drive current). Resulting image (FOV: 4cm by 4cm) of a marmoset brain acquired by a commercial gradient coil.

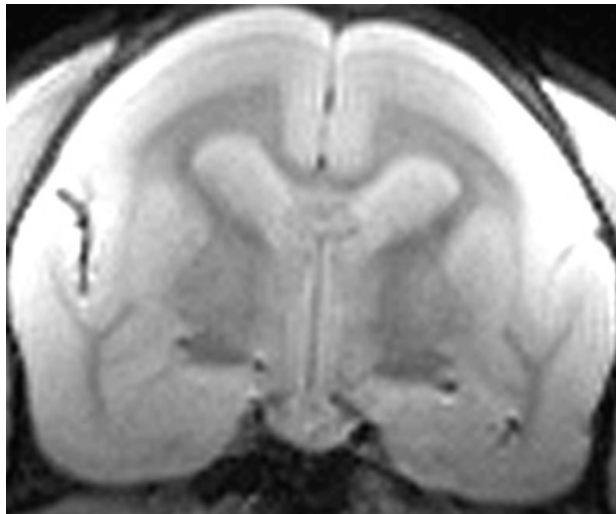


Figure 3.28: Six-loop G_y gradient coil (coil plane size: 12 cm by 24 cm, 5 G/cm at 25 A drive current). Resulting image (FOV: 4cm by 4cm) of the six-loop G_y coil depicted in Figure 3.23. The surface coil was operated as phase encoding gradients.

The drive current setting of the six-loop coil had to be reduced by a factor of four to stay compatible with the remaining two commercial (G_x, G_z) gradient coils. A remarkable experimental observation is that, due to the relatively large distance from the gradient plane to main magnet bore; no shimming or shielding is required to operate the six-loop coil technology. Moreover, because of the open designs placed in close proximity to the sample, eddy current influences are negligible.

3.6 Chapter Summary

This chapter discussed the Least Squares Method for coil design. The LS method permits the control of the field uniformity through numbers of discretization m and n (in z and x directions). High numbers of m and n correspond to high gradient uniformity and low gradient strength. The method allows us to control the coil inductance as well as shielding and balancing. To address these issues, another method has to be developed. The new method presented in Chapter 4 deals with a wide variety of coil geometries and it is significantly more powerful.

Charter 4

Stream Function Method for Gradient Coil Design

A new design approach for the construction of gradient coils for magnetic resonance imaging is presented. The theoretical formulation involves a constraint cost function between the desired field in a particular region of interest in space and an almost arbitrarily defined surface that carries the current configuration based on Biot-Savart's integral equation. An appropriate weight function in conjunction with linear approximation functions permits us to transform the problem formulation into a linear matrix equation whose solution yields discrete current elements in terms of magnitude and direction within a specified coil surface. Numerical predictions for the G_x , G_y , G_z gradient coils underscore the success of this approach in terms of achieving a highly linear field while maintaining low parasitic fields and low inductance.

4.1 Theory

Generally speaking, the gradient coil system in an MR instrument requires three coils termed G_x , G_y , G_z . Each orientation consists of two subsets: primary and secondary coils. Purpose of the primary coil is to create the gradient field, while the secondary coil is to suppress the magnetic field outside the gradient system. Furthermore, each of these coils may be implemented by one or several current-carrying surfaces positioned in space. This generic setup is illustrated in Figure 4.1.

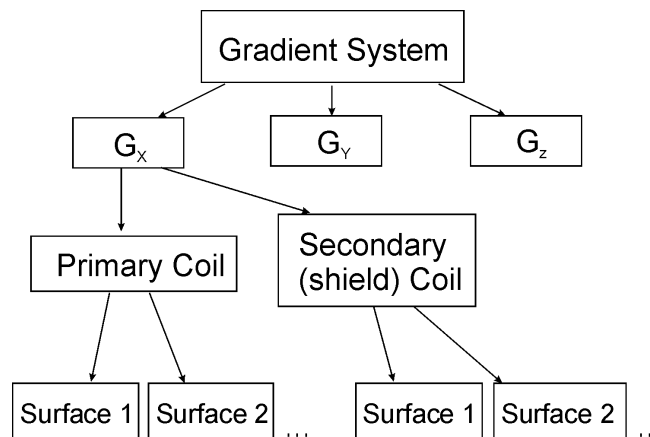


Figure 4.1: Conceptual arrangement of the gradient system.

Let us consider the construction of the primary coil first. We define a surface that establishes the gradient field with a surface current distribution $\mathbf{J}(\mathbf{r})$ flowing in this plane. In general, the coil plane may consist of several discrete surfaces that are not connected with each other. An example of a structure consisting of two surfaces is the bi-planar gradient coil shown in Figure 4.2.

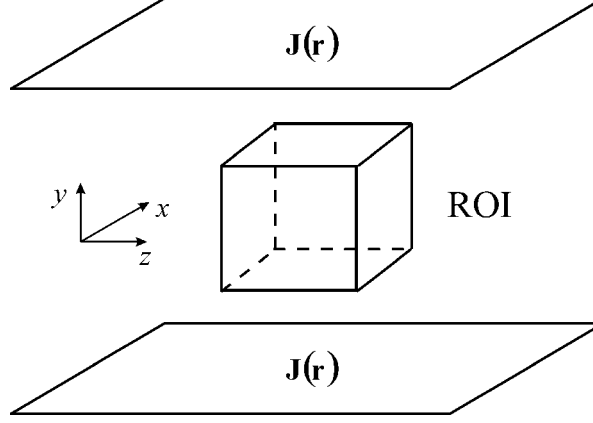


Figure 4.2: Geometric surface source configuration $\mathbf{J}(\mathbf{r})$ that constitutes a bi-planar gradient coil.

Our goal is to find an optimal current distribution so as to achieve a desired magnetic field in the ROI as depicted in Figure 4.2. Moreover, the magnetic energy of the coil has to be low to reduce the total inductance, and each part of the coil may be set to be torque-free. Also, since the primary interest is the gradient of the magnetic field, one has to optimize the offset magnetic field. The reason for this is the following: for certain coil geometries we could achieve a better performance if the magnetic field is non-zero in the center of the ROI. This so-called bias field optimization is particularly important in case of uniplanar G_y gradient coils, which typically possess a bias magnetic field. Furthermore, the magnetic flux through the secondary (shield) coil has to be minimal to reduce coupling with surrounding metallic structures. According to these requirements, we introduce a cost function Φ that consists of four terms:

$$\Phi = \frac{1}{2} \sum_{k=1}^K W(\mathbf{r}_k) [B_z(\mathbf{r}_k) - B_{des,z}(\mathbf{r}_k) + B_{off,z}]^2 + \alpha W_{magn} + \beta \frac{1}{2A_s} \int_{S_s} (\mathbf{B} \cdot \mathbf{n})^2 dS_s - \sum_{p=1}^P (\lambda_{px} M_{px} + \lambda_{py} M_{py} + \lambda_{pz} M_{pz}). \quad (4.1)$$

Here $W(\mathbf{r})$ is a weight function, $B_{des,z}(\mathbf{r})$ is the z -component of the desired magnetic field, $B_{off,z}$ is an offset (bias) magnetic field. W_{magn} is the magnetic energy of the current (in both primary and secondary coils), α is a magnetic energy weight coefficient, \mathbf{B} is the magnetic field, β is a shielding weight coefficient, and A_s is the area of the shield. Finally, M_{px} , M_{py} , M_{pz} are the components of the torque vector \mathbf{M}_p , which is calculated with respect to a fixed point, the origin. In Eq. (4.1) index K is the number of points in the ROI. Index p labels all separate surfaces (from 1 to P) of the gradient coil. For example, for the bi-planar design, $P=2$. Finally, λ_{px} , λ_{py} , λ_{pz} are Lagrange multipliers.

As we see from Eq. (4.1), the cost function Φ is first of all a weighted sum of squared deviations from the desired field. In addition, the magnetic energy term, shielding term, and Lagrange multipliers are introduced to ensure that the inductance is minimized, the magnetic flux through the shield is minimized, and that every part of the gradient coil is torque-free. It is worth noting that the introduction of the Lagrange coefficients for the torque vector is optional. This is because for certain coil geometries some (or all) components of \mathbf{M} may equal zero. In Eq. (4.1) the explicit expression for the magnetic energy is

$$W_{magn} = \frac{\mu_0}{8\pi} \int_S \int_{S'} \mathbf{J}(\mathbf{r}) \cdot \mathbf{J}(\mathbf{r}') \frac{1}{|\mathbf{r} - \mathbf{r}'|} dS dS'. \quad (4.2)$$

Furthermore, the expression for the torque \mathbf{M} can be cast in the form:

$$\mathbf{M} = \int_S \mathbf{r} \times [\mathbf{J}(\mathbf{r}) \times \mathbf{B}_0(\mathbf{r})] dS, \quad (4.3)$$

where $\mathbf{B}_0(\mathbf{r})$ is the external magnetic field. Usually, $\mathbf{B}_0(\mathbf{r})$ is directed along the z -axis, which simplifies (4.3) to

$$\mathbf{M} = B_0 \begin{pmatrix} \int_S J_x z dS \\ \int_S J_y z dS \\ - \int_S (J_x x + J_y y) dS \end{pmatrix}, \quad (4.4)$$

where x, y, z are components of the radial vector \mathbf{r} . Under steady state conditions, the current satisfies the conservation of charge equation

$$\nabla \cdot \mathbf{J}(\mathbf{r}) = 0. \quad (4.5)$$

It is our goal to develop an efficient computational method to determine the current distribution $\mathbf{J}(\mathbf{r})$ that minimizes the cost function Φ .

4.2 Methodology

To fix ideas, let us consider an arbitrary surface discretized into triangular patches. For simplicity, we consider a flat surface as shown in Figure 4.3. This surface could, either completely or in part, accommodate the gradient coil arrangement. We notice that this surface has an exterior and interior boundary.

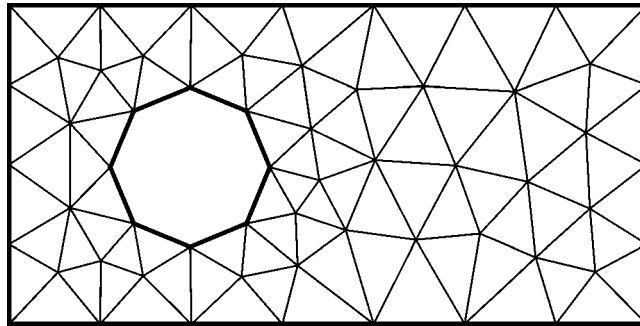


Figure 4.3: Triangulated surface with exterior and interior boundaries.

We arbitrarily select one side of the surface to be “positive” and define a unit-length vector $\mathbf{n}(\mathbf{r})$ perpendicular to this surface. We further define a stream function $\phi(\mathbf{r})$

residing in this surface. Consequently, the surface current density $\mathbf{J}(\mathbf{r})$ is tangential to the normal $\mathbf{n}(\mathbf{r})$, or

$$\mathbf{J}(\mathbf{r}) = \nabla \times [\varphi(\mathbf{r}) \mathbf{n}(\mathbf{r})]. \quad (4.6)$$

We approximate the stream function $\varphi(\mathbf{r})$ by linear or hat (Chapeau) basis functions $\varphi_n(\mathbf{r})$. The stream function is a combination of the basis functions with unknown coefficients I_n :

$$\varphi(\mathbf{r}) \approx \sum_{n=1}^N I_n \varphi_n(\mathbf{r}), \quad (4.7)$$

where N is the total number of nodes. Substituting (4.7) into (4.6) results in

$$\mathbf{J}(\mathbf{r}) \approx \sum_{n=1}^N I_n \nabla \times [\varphi_n(\mathbf{r}) \mathbf{n}(\mathbf{r})] = \sum_{n=1}^N I_n \mathbf{f}_n(\mathbf{r}). \quad (4.8)$$

Functions $\mathbf{f}_n(\mathbf{r})$ can be illustrated as follows: from all surface nodes we can pick two nodes (node 1 and node 2) as shown in Figure 4.4.

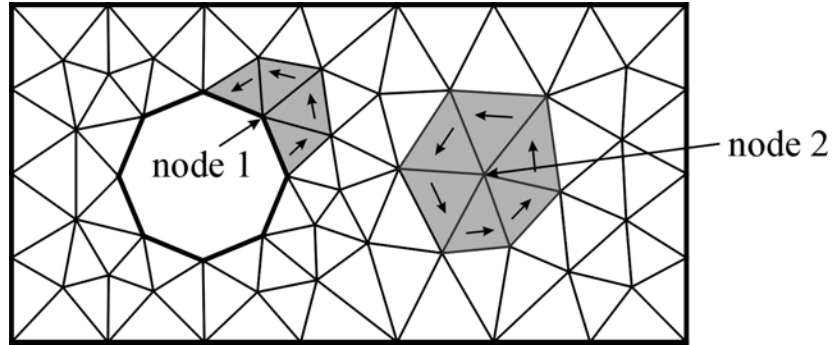


Figure 4.4: Two nodes at which the current elements on the surface are evaluated.

A current element includes all neighboring triangle patches of the chosen non-boundary node, see Figure 4.5(a).

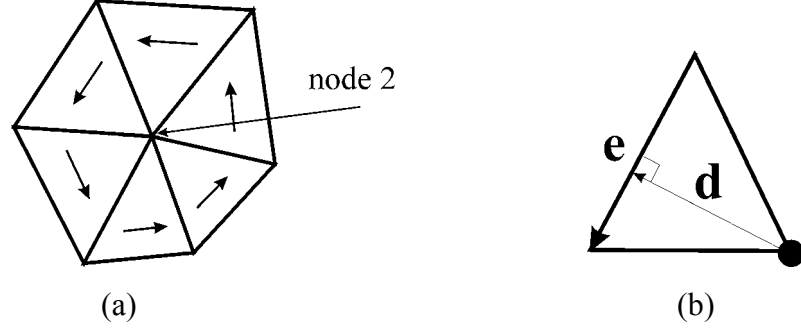


Figure 4.5: (a) Current element and basis function $\mathbf{f}_n(\mathbf{r})$, (b) one of the triangles associated with the selected node.

In general, an algorithm can be developed that ensures that all current elements have flow direction in the same way (clockwise or counterclockwise).

In each neighboring triangle we introduce vectors \mathbf{e} (opposite edge) and \mathbf{d} (minimum distance vector) perpendicular to \mathbf{e} (see Figure 4.5(b)). Mathematically, the expression for the current basis function $\mathbf{f}_n(\mathbf{r})$ is then

$$\mathbf{f}_n(\mathbf{r}) = \begin{cases} \frac{\mathbf{e}_{ni}}{|\mathbf{e}_{ni}| |\mathbf{d}_{ni}|} \frac{1}{N_n}, & \text{if } \mathbf{r} \text{ belongs to } \Delta_{ni}, \\ 0, & \text{otherwise} \end{cases} \quad i = 1, \dots, N_n, \quad (4.9)$$

where N_n is the number of triangles in a particular current element and Δ_{ni} denotes an i^{th} triangle belonging to node n . To simplify notation, we rewrite (4.9) as:

$$\mathbf{f}_n(\mathbf{r}) = \begin{cases} \mathbf{v}_{ni}, & \text{if } \mathbf{r} \text{ belongs to } \Delta_{ni}, \\ 0, & \text{otherwise} \end{cases} \quad i = 1, \dots, N_n, \quad (4.10)$$

where $\mathbf{v}_{ni} = \mathbf{e}_{ni} / (|\mathbf{e}_{ni}| |\mathbf{d}_{ni}|)$. Clearly, the divergence of $\mathbf{f}_n(\mathbf{r})$ is zero and the flux through the edges containing the selected node is unity.

4.3 System of Linear Equations

Utilizing (4.8) we can approximate the magnetic vector potential as follows:

$$\mathbf{A}(\mathbf{r}) = \frac{\mu_0}{4\pi} \int_{S'} \frac{\mathbf{J}(\mathbf{r}')}{|\mathbf{r} - \mathbf{r}'|} dS' \approx \frac{\mu_0}{4\pi} \sum_{n=1}^N I_n \int_{S'} \frac{\mathbf{f}_n(\mathbf{r}')}{|\mathbf{r} - \mathbf{r}'|} dS'. \quad (4.11)$$

The magnetic flux density is then

$$\mathbf{B}(\mathbf{r}) = \nabla \times \mathbf{A}(\mathbf{r}) \approx \frac{\mu_0}{4\pi} \sum_{n=1}^N I_n \int_{S'} \nabla \times \frac{\mathbf{f}_n(\mathbf{r}')}{|\mathbf{r} - \mathbf{r}'|} dS' = \frac{\mu_0}{4\pi} \sum_{n=1}^N I_n \int_{S'} \nabla \frac{1}{|\mathbf{r} - \mathbf{r}'|} \times \mathbf{f}_n(\mathbf{r}') dS'. \quad (4.12)$$

If we consider only the z -component of the magnetic flux density, we see immediately that

$$B_z(\mathbf{r}) \approx \frac{\mu_0}{4\pi} \sum_{n=1}^N I_n \int_{S'} \left[\frac{-f_{ny}(\mathbf{r}')(x-x') + f_{nx}(\mathbf{r}')(y-y')}{|\mathbf{r} - \mathbf{r}'|^3} \right] dS'. \quad (4.13)$$

Again, to simplify the notation we introduce:

$$c_n(\mathbf{r}) = \frac{\mu_0}{4\pi} \int_{S'} \left[\frac{-f_{ny}(\mathbf{r}')(x-x') + f_{nx}(\mathbf{r}')(y-y')}{|\mathbf{r} - \mathbf{r}'|^3} \right] dS' \quad (4.14)$$

and re-express (4.14) in a series expansion:

$$B_z(\mathbf{r}) \approx \sum_{n=1}^N I_n c_n(\mathbf{r}). \quad (4.15)$$

Next, we define the magnetic energy as follows:

$$W_{magn} = \frac{\mu_0}{8\pi} \iint_{S S'} \frac{\mathbf{J}(\mathbf{r}) \cdot \mathbf{J}(\mathbf{r}')}{|\mathbf{r} - \mathbf{r}'|} dS' dS \approx \frac{\mu_0}{8\pi} \sum_{n=1}^N \sum_{m=1}^N I_n I_m \iint_{S S'} \frac{\mathbf{f}_n(\mathbf{r}) \cdot \mathbf{f}_m(\mathbf{r}')}{|\mathbf{r} - \mathbf{r}'|} dS' dS. \quad (4.16)$$

The mutual inductance between the m^{th} and n^{th} elements can then be cast in the following inductance expression:

$$L_{mn} = \frac{\mu_0}{4\pi} \iint_{S S'} \frac{\mathbf{f}_n(\mathbf{r}) \cdot \mathbf{f}_m(\mathbf{r}')}{|\mathbf{r} - \mathbf{r}'|} dS' dS, \quad n, m = 1, \dots, N. \quad (4.17)$$

Because of symmetry, we have $L_{mn} = L_{nm}$. Thus,

$$W_{magn} \approx \frac{1}{2} \sum_{n=1}^N \sum_{m=1}^N I_n I_m L_{mn}. \quad (4.18)$$

The normal component of the magnetic flux density with respect to the triangle Δ of the shield is

$$B_{n\Delta}(\mathbf{r}) \approx \frac{\mu_0}{4\pi} \sum_{n=1}^N I_n \mathbf{n}_\Delta \cdot \int_{S'} \nabla \frac{1}{|\mathbf{r} - \mathbf{r}'|} \times \mathbf{f}_n(\mathbf{r}') dS', \quad \Delta = 1, \dots, N_s. \quad (4.19)$$

We re-express (4.19) as

$$B_{n\Delta}(\mathbf{r}_\Delta) \approx \sum_{n=1}^N I_n d_{n\Delta}, \quad \Delta = 1, \dots, N_s, \quad (4.20)$$

where

$$\begin{aligned} d_{n\Delta} = & \frac{\mu_0}{4\pi} \int_{S'} n_{\Delta x} \left[\frac{-f_{nz}(\mathbf{r}')(y-y') + f_{ny}(\mathbf{r}')(z-z')}{|\mathbf{r} - \mathbf{r}'|^3} \right] dS' \\ & + \frac{\mu_0}{4\pi} \int_{S'} n_{\Delta y} \left[\frac{-f_{nx}(\mathbf{r}')(z-z') + f_{nz}(\mathbf{r}')(x-x')}{|\mathbf{r} - \mathbf{r}'|^3} \right] dS' \\ & + \frac{\mu_0}{4\pi} \int_{S'} n_{\Delta z} \left[\frac{-f_{ny}(\mathbf{r}')(x-x') + f_{nx}(\mathbf{r}')(y-y')}{|\mathbf{r} - \mathbf{r}'|^3} \right] dS', \end{aligned} \quad (4.21)$$

$n = 1, \dots, N, \quad \Delta = 1, \dots, N_s.$

The components of the torque vector are:

$$M_x = B_0 \int_S J_x z dS \approx B_0 \sum_{n=1}^N I_n \int_S f_{nx} z dS, \quad (4.22)$$

$$M_y = B_0 \int_S J_y z dS \approx B_0 \sum_{n=1}^N I_n \int_S f_{ny} z dS, \quad (4.23)$$

$$M_z = -B_0 \int_S (J_x x + J_y y) dS \approx -B_0 \sum_{n=1}^N I_n \int_S (f_{nx} x + f_{ny} y) dS. \quad (4.24)$$

Combining all the above expressions, the functional Φ assumes the final form

$$\begin{aligned} \Phi = & \frac{1}{2} \sum_{k=1}^K W(\mathbf{r}_k) (B_z(\mathbf{r}_k) - B_{des,z}(\mathbf{r}_k) + B_{off,z})^2 + \frac{\alpha}{2} \sum_{n=1}^N \sum_{m=1}^N I_n I_m L_{nm} + \beta \frac{1}{2A_s} \sum_{\Delta=1}^{N_s} A_\Delta B_{n\Delta}(\mathbf{r}_\Delta)^2 \\ & - B_0 \sum_{p=1}^P \left\{ \lambda_{px} \sum_{n=1}^N \delta_{n \in p} I_n \int_S f_{nx} z dS + \lambda_{py} \sum_{n=1}^N \delta_{n \in p} I_n \int_S f_{ny} z dS - \lambda_{pz} \sum_{n=1}^N I_n \delta_{n \in p} \int_S (f_{nx} x + f_{ny} y) dS \right\}. \end{aligned} \quad (4.25)$$

Here, A_s is the area of the shield, $\delta_{n \in p}$ equals one if the n^{th} current element belongs to the p^{th} surface part of the gradient coil, otherwise it is zero. For convenience we denote

$\tilde{\lambda}_x = B_0 \lambda_x$, $\tilde{\lambda}_y = B_0 \lambda_y$, $\tilde{\lambda}_z = B_0 \lambda_z$. As a next step, we can now minimize the functional

Φ :

$$\begin{aligned}
0 = \frac{\partial \Phi}{\partial I_{n'}} &= \sum_k W(\mathbf{r}_k) c_{n'}(\mathbf{r}_k) \left[\sum_{n=1}^N I_n c_n(\mathbf{r}_k) - B_{des,z}(\mathbf{r}_k) + B_{off,z} \right] \\
&+ \frac{\alpha}{2} \sum_{n=1}^N \sum_{m=1}^N (\delta_{n'm} I_n + \delta_{n'n} I_m) L_{mn} + \frac{\beta}{A_s} \sum_{\Delta=1}^{N_s} A_{\Delta} \left(\sum_{n=1}^N d_{n\Delta} I_n \right) d_{n'\Delta} \\
&- \sum_{p=1}^P \delta_{n' \in p} \left\{ \tilde{\lambda}_{px} \int_S f_{n'x} z dS + \tilde{\lambda}_{py} \int_S f_{n'y} z dS - \tilde{\lambda}_{pz} \int_S (f_{n'x} x + f_{n'y} y) dS \right\}, \\
& \hspace{15em} n' = 1, \dots, N.
\end{aligned} \tag{4.26}$$

Simplifying (4.26) results in:

$$\begin{aligned}
0 = \frac{\partial \Phi}{\partial I_{n'}} &= \sum_{n=1}^N I_n \sum_k W(\mathbf{r}_k) c_{n'}(\mathbf{r}_k) c_n(\mathbf{r}_k) - \sum_{k=1}^K W(\mathbf{r}_k) c_{n'}(\mathbf{r}_k) B_{des,z}(\mathbf{r}_k) \\
&+ B_{off,z} \sum_{k=1}^N W(\mathbf{r}_k) c_{n'}(\mathbf{r}_k) + \alpha \sum_{n=1}^N I_n L_{n'n} + \frac{\beta}{A_s} \sum_{n=1}^N \left(\sum_{\Delta=1}^{N_s} A_{\Delta} d_{n\Delta} d_{n'\Delta} \right) I_n \\
&- \sum_{p=1}^P \left\{ \tilde{\lambda}_{px} \delta_{n' \in p} \int_S f_{n'x} z dS + \tilde{\lambda}_{py} \delta_{n' \in p} \int_S f_{n'y} z dS - \tilde{\lambda}_{pz} \delta_{n' \in p} \int_S (f_{n'x} x + f_{n'y} y) dS \right\}, \\
& \hspace{15em} n' = 1, \dots, N.
\end{aligned} \tag{4.27}$$

Upon differentiating (4.25) with respect to the bias term $B_{off,z}$, we obtain:

$$\begin{aligned}
0 = \frac{\partial \Phi}{\partial B_{off,z}} &= \sum_{k=1}^K W(\mathbf{r}_k) \left(\sum_{n=1}^N I_n c_n(\mathbf{r}_k) - B_{des,z}(\mathbf{r}_k) + B_{off,z} \right) = \\
&= \sum_{k=1}^K W(\mathbf{r}_k) \sum_{n=1}^N I_n c_n(\mathbf{r}_k) + B_{off,z} \sum_{k=1}^K W(\mathbf{r}_k) - \sum_{k=1}^K W(\mathbf{r}_k) B_{des,z}(\mathbf{r}_k).
\end{aligned} \tag{4.28}$$

Furthermore, differentiating (4.25) with respect to $\tilde{\lambda}_x$, $\tilde{\lambda}_y$, $\tilde{\lambda}_z$ yields:

$$0 = \frac{\partial \Phi}{\partial \tilde{\lambda}_{p'x}} = - \sum_{n=1}^N \delta_{n \in p'} I_n \int_S f_{nx} z dS, \quad p' = 1, \dots, P, \tag{4.29}$$

$$0 = \frac{\partial \Phi}{\partial \tilde{\lambda}_{p'y}} = - \sum_{n=1}^N \delta_{n \in p'} I_n \int_S f_{ny} z dS, \quad p' = 1, \dots, P, \tag{4.30}$$

$$0 = \frac{\partial \Phi}{\partial \tilde{\lambda}_{p'z}} = \sum_{n=1}^N I_n \delta_{n \in p'} \int_S (f_{nx} x + f_{ny} y) dS, \quad p' = 1, \dots, P, \tag{4.31}$$

where P is the number of surfaces composing the gradient coil. We form a vector of unknowns such that

$$\mathbf{X} = \left\{ I_1, \dots, I_N, B_{off,z}, \tilde{\lambda}_{1x}, \tilde{\lambda}_{1y}, \tilde{\lambda}_{1z}, \dots, \tilde{\lambda}_{Px}, \tilde{\lambda}_{Py}, \tilde{\lambda}_{Pz} \right\}^T$$

The resulting linear system of equations consists of the following terms:

$$\begin{aligned} & \sum_{n=1}^N \left(\sum_k W(\mathbf{r}_k) c_{n'}(\mathbf{r}_k) c_n(\mathbf{r}_k) + \alpha L_{n'n} + \frac{\beta}{A_s} \sum_{\Delta=1}^{N_s} A_{\Delta} d_{n\Delta} d_{n'\Delta} \right) I_n + B_{off,z} \sum_{k=1}^K W(\mathbf{r}_k) c_{n'}(\mathbf{r}_k) \\ & - \sum_{p=1}^P \left\{ \tilde{\lambda}_{px} \delta_{n' \in p} \int_S f_{n'x} z dS + \tilde{\lambda}_{py} \delta_{n' \in p} \int_S f_{n'y} z dS - \tilde{\lambda}_{pz} \delta_{n' \in p} \int_S (f_{n'x} x + f_{n'y} y) dS \right\} \end{aligned} \quad (4.32)$$

$$= \sum_{k=1}^K W(\mathbf{r}_k) c_{n'}(\mathbf{r}_k) B_{des,z}(\mathbf{r}_k), \quad n' = 1, \dots, N,$$

$$\sum_{n=1}^N \left(\sum_{k=1}^K c_n(\mathbf{r}_k) W(\mathbf{r}_k) \right) I_n + B_{off,z} \sum_{k=1}^K W(\mathbf{r}_k) = \sum_{k=1}^K W(\mathbf{r}_k) B_{des,z}(\mathbf{r}_k), \quad (4.33)$$

$$\sum_{n=1}^N \left(\delta_{n \in p'} \int_S f_{nx} z dS \right) I_n = 0, \quad p' = 1, \dots, P, \quad (4.34)$$

$$\sum_{n=1}^N \left(\delta_{n \in p'} \int_S f_{ny} z dS \right) I_n = 0, \quad p' = 1, \dots, P, \quad (4.35)$$

$$\sum_{n=1}^N \left(\delta_{n \in p'} \int_S (f_{nx} x + f_{ny} y) dS \right) I_n = 0, \quad p' = 1, \dots, P. \quad (4.36)$$

These individual equations can be collected into a large global matrix equation:

$$\mathbf{Z}\mathbf{I} = \mathbf{b}. \quad (4.37)$$

When solving this system of equations we have to keep in mind that all nodes belonging to the same boundary give rise only to one unknown since the stream function is the same for each one of them. Also, we have to prescribe a value of the stream function on one of the boundaries. For example, in Figure 4.4 there are two boundaries (exterior and interior). All exterior boundary nodes have the same value of the stream function, which we arbitrarily set to zero. All inner boundary nodes also share the same value of the stream function (unknown yet).

4.4 Mutual Inductance Calculation

The mutual inductances $L_{n'n}$ are given by (4.17). Explicitly, we can state

$$L_{mn} = \begin{cases} \frac{\mu_0}{4\pi} \sum_i \sum_j (\mathbf{v}_{mi} \cdot \mathbf{v}_{nj}) \frac{A_{mi} A_{nj}}{|\mathbf{r}_{mi} - \mathbf{r}'_{nj}|}, & \text{if } \Delta_{mi} \neq \Delta_{nj} \\ \frac{\mu_0}{4\pi} \sum_i \sum_j (\mathbf{v}_{mi} \cdot \mathbf{v}_{nj}) \int_{S_{mi}} \int_{S'_{mi}} \frac{dS' dS}{|\mathbf{r}_{mi} - \mathbf{r}'_{mi}|}, & \text{if } \Delta_{mi} = \Delta_{nj}, \end{cases} \quad (4.38)$$

where A_{mi} is the area of the corresponding triangle patch. The notation in (4.38) is best seen with reference to Figure 4.6.

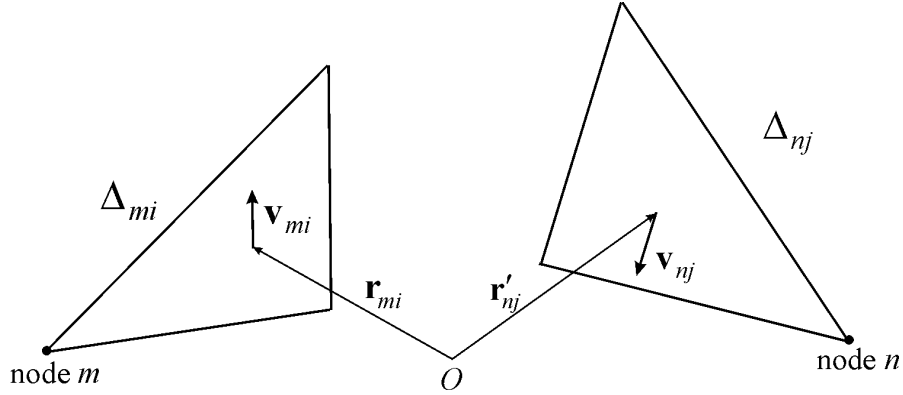


Figure 4.6: Interaction between the currents flowing in the triangles Δ_{mi} and Δ_{nj} .

In case of $\Delta_{mi} = \Delta_{nj}$ the double integral can be calculated in a closed form [23] and is given in (4.39):

$$\begin{aligned} \frac{1}{4A^2} \int_{S_{mi}} \int_{S'_{mi}} \frac{dS' dS}{|\mathbf{r}_{mi} - \mathbf{r}'_{mi}|} &= \frac{1}{6\sqrt{a}} \ln \left(\frac{(a - b + \sqrt{a}\sqrt{a - 2b + c})(b + \sqrt{ac})}{(-b + \sqrt{ac})(-a + b + \sqrt{a}\sqrt{a - 2b + c})} \right) \\ &+ \frac{1}{6\sqrt{c}} \ln \left(\frac{(b + \sqrt{ac})(-b + c + \sqrt{c}\sqrt{a - 2b + c})}{(b - c + \sqrt{c}\sqrt{a - 2b + c})(-b + \sqrt{ac})} \right) + \\ &+ \frac{1}{6\sqrt{a - 2b + c}} \ln \left(\frac{(a - b + \sqrt{a}\sqrt{a - 2b + c})(-b + c + \sqrt{c}\sqrt{a - 2b + c})}{(b - c + \sqrt{c}\sqrt{a - 2b + c})(-a + b + \sqrt{a}\sqrt{a - 2b + c})} \right), \end{aligned} \quad (4.39)$$

where $a = (\mathbf{r}_3 - \mathbf{r}_1) \cdot (\mathbf{r}_3 - \mathbf{r}_1)$, $b = (\mathbf{r}_3 - \mathbf{r}_1) \cdot (\mathbf{r}_3 - \mathbf{r}_2)$, $c = (\mathbf{r}_3 - \mathbf{r}_2) \cdot (\mathbf{r}_3 - \mathbf{r}_2)$ and $\mathbf{r}_1, \mathbf{r}_2, \mathbf{r}_3$

are the vectors pointing to the three nodes of the triangle.

4.5 Examples of Coil Design

To reduce the mathematical formulation to practice, we will consider several gradient coil configurations.

(a) Crescent G_x Gradient Coil

To demonstrate how the algorithm works, let us consider a coil consisting of two curved plates, each of which has a size of 20×10 cm. These plates are curved with a radius of $R=6.5$ cm and positioned side by side. The coil is discretized into a triangular mesh as shown in Figure 4.7. In total, the coil consists of 1380 nodes and 2546 triangle patches.

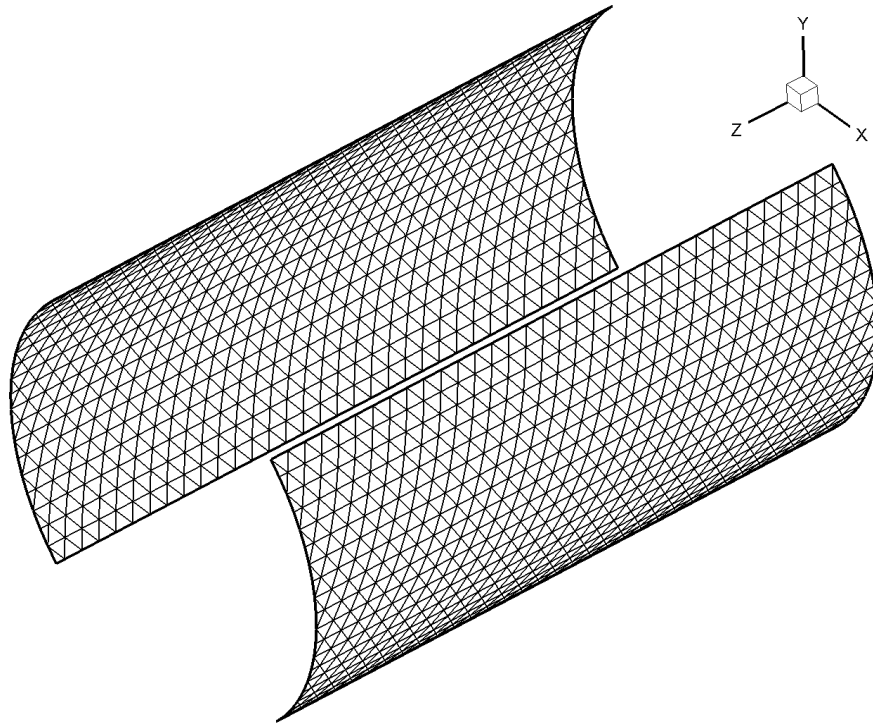


Figure 4.7: Surface discretization of the two plate crescent coil.

Using the developed algorithm, we determine all the current elements composing this coil. Again, the number of current elements is equal to the number of nodes in the coil.

The region of interest (ROI) is defined as a $6 \times 6 \times 6$ cm cube located in the center of the coil. Along each axis we choose 10 equidistant points. Thus, there are 1000 points within the cube at which we can define the desired magnetic field. Other parameters specified during the simulation include the gradient strength $G = 10^{-4}$ T/m, the weighting parameter $\alpha = 10^{-7}$, and a weight function $W_k = 1/1000$ for all points k .

The entries for inductance matrix \mathbf{L} are based on evaluation of (4.17); the matrix \mathbf{Z} entries as well as the vector \mathbf{b} components are filled according to equations (4.32) - (4.36). Solving the resulting system (4.37) we obtain vector \mathbf{I} that represents the values of the stream function at the corresponding nodes. Figure 4.8 depicts the distribution of the stream function on the surface of the coil.

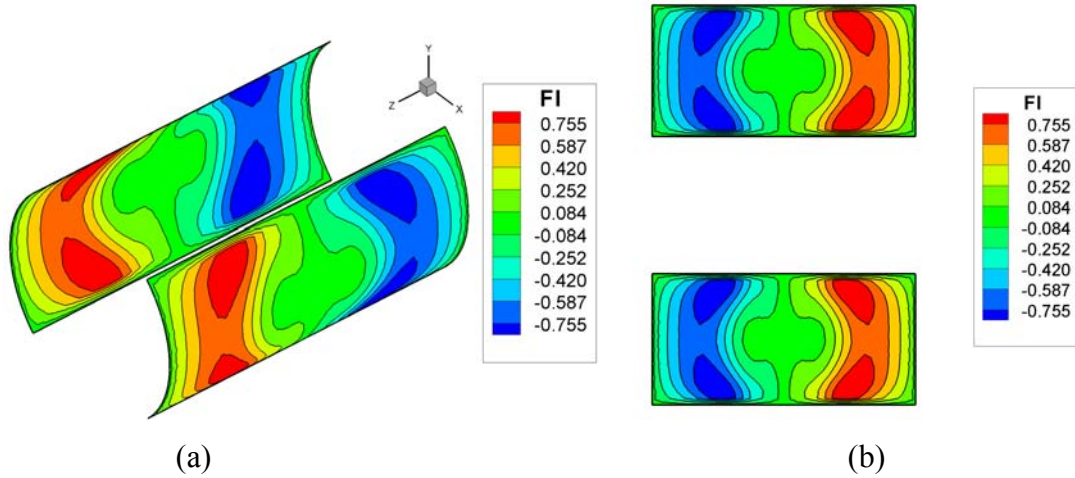


Figure 4.8: Stream function $\varphi(\mathbf{r})$ distribution in [A]; (a) original bi-surface coil layout, (b) wire patterns projected onto two flat planes.

The stream function ranges from $\varphi_{\min} = -0.9231$ A to $\varphi_{\max} = 0.9231$ A. We next have to discretize the stream function range into a certain number of levels. Each level gives rise to one or several grooves that must carry several wire loops. A high number of levels would give us a discrete coil whose field is close to that of a continuous coil.

Unfortunately, but such a coil would be difficult to manufacture. We choose to divide the interval into $N_{\text{level}} = 6$ levels, each one having a size of $\Delta\phi = 0.3077 \text{ A}$. For the value of the stream function in the middle of each level we use the notation ϕ_{level} . Thus we determine and plot loops corresponding to each of the levels ϕ_{level} . These loops represent paths needed to lay out the wire pattern. Having found the wiring of the coil, we are able to plot the magnetic field within the ROI. Figure 4.9 displays the wire pattern corresponding to six levels of the stream function. It also shows the magnetic field inside the coil. The gradient strength in the center of ROI is 27.96 G/cm for a drive current of 100A.

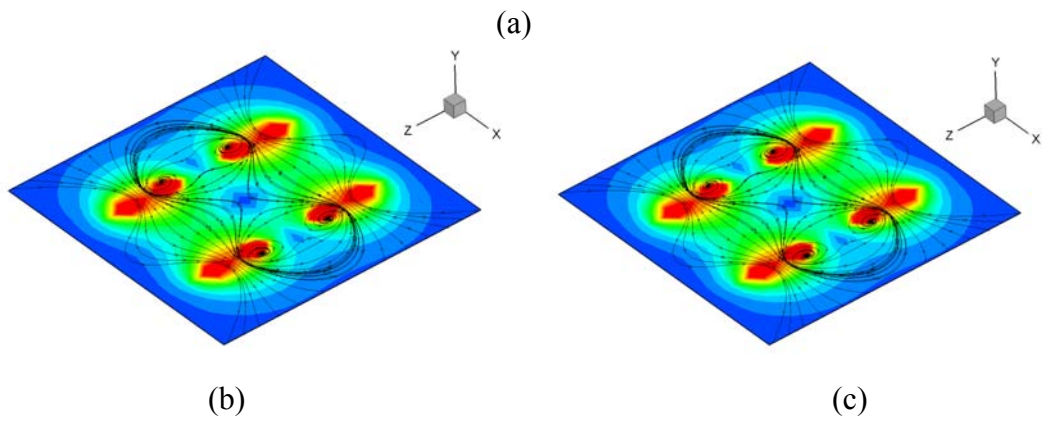
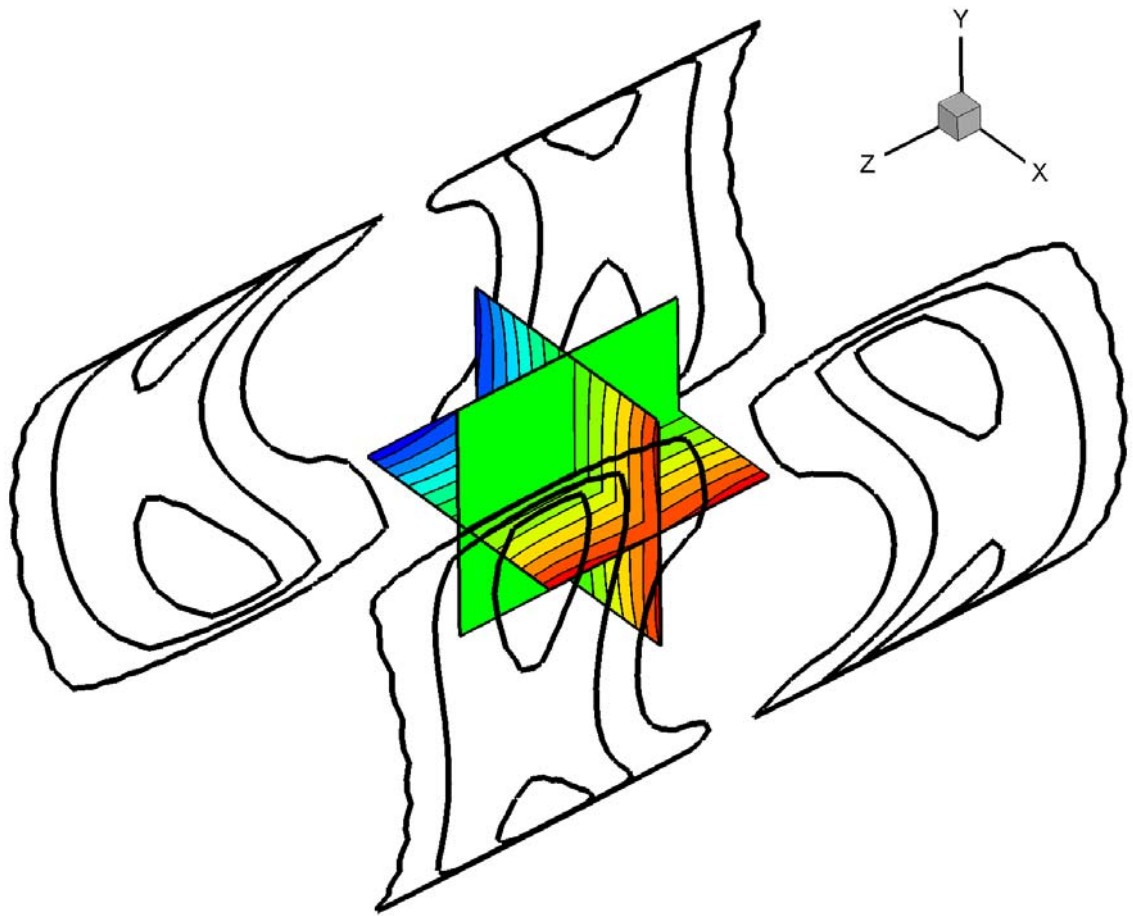


Figure 4.9: G_x crescent coil with $\alpha = 10^{-7}$, (a) wire pattern and z -component of the magnetic flux density, (b) wire pattern and absolute value of magnetic flux density, (c) streamlines of the magnetic flux density.

The magnetic energy of the coil is $W_{magn} = 1.53919 \cdot 10^{-7} \text{ J}$. If wound with AWG-20 copper wire, and assuming a total resistance of $R = 1.035 \text{ } \Omega$, a total wire length of 31.07 m is needed. When placed into the former, this results in nine turns.

When this coil is driven with 1 A current, the magnetic energy in this case becomes $W_{magn} = (9/0.3077)^2 \cdot 1.539 \cdot 10^{-7} \text{ J} = 1.317 \cdot 10^{-4} \text{ J}$. In addition, the total inductance is $L = 2W_{magn} / (1\text{A})^2 = 263 \text{ } \mu\text{H}$. We should keep in mind that this value corresponds to a continuous current distribution in the coil. Actual values of inductance may differ from this value significantly.

We can next examine the coil performance in terms of the quality factor Q_x

defined by $Q_x = \min_{\text{ROI}} \left(\frac{|G_x|}{\sqrt{G_x^2 + G_y^2 + G_z^2}} \right)$, and in terms of the ratio

$$U_x = \min_{\text{ROI}}(G_x) / \max_{\text{ROI}}(G_x).$$

The value of Q_x indicates how strong the influence of the parasitic gradients (G_y and G_z) is. The closer Q_x is to one, the lower the parasitic gradient influence is. The value of U_x on the other hand shows us how uniform the magnetic field in the ROI is. Low values of U_x indicate non-uniform magnetic field distribution. For the above coil, we obtain the following results:

Table 3: Performance of crescent coil depicted in Figure 4.9.

	Q_x	U_x
6×6×6 cm cube	0.943	0.366
5×5×5 cm cube	0.978	0.573
4×4×4 cm cube	0.994	0.766

In this model, the coil performance is affected by the choice of the points in the ROI and by parameter α . When choosing a large value of α , we achieve a low inductance design at the expense of field uniformity. Alternatively, when choosing a low α , we achieve a highly uniform magnetic field. However, the coil wire pattern becomes very complicated, which makes it difficult to construct. For this G_x gradient coil the value of $\alpha = 10^{-7}$ represents a good balance in terms of high field uniformity and low inductance.

(b) Flat G_y Gradient Coil with Holes

As a second example, we consider a flat 20×10 cm coil with six holes (diameter 2 cm) reserved for fastening. The coil's mesh consists of 1327 nodes and 2444 triangle patches (Figure 4.10).

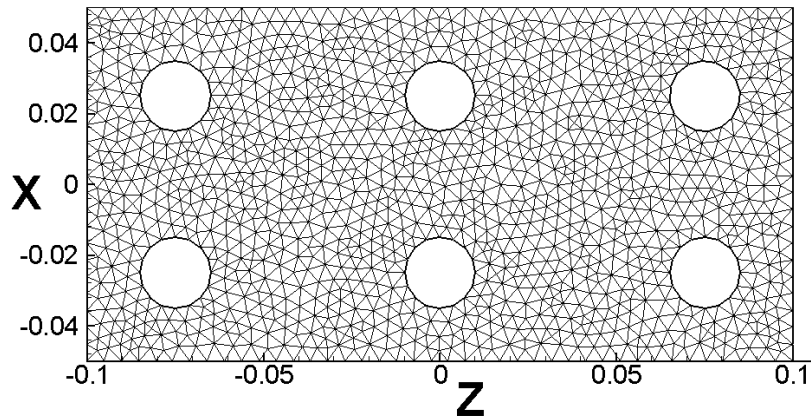


Figure 4.10: Flat coil surface discretization. Spatial dimensions are given in [m].

The region of interest where we prescribe the magnetic field is defined as a 6×6×6 cm cube with the center at (0, 6, 0) cm, or 6 cm above the coil plane. Also, we set the gradient strength to $G = 10^{-4}$ T/m, the weighting parameter to $\alpha = 10^{-7}$, and a weight

function to $W_k = 1/1000$ for all k . Having solved the system of equations, we obtain the stream function depicted in Figure 4.11.

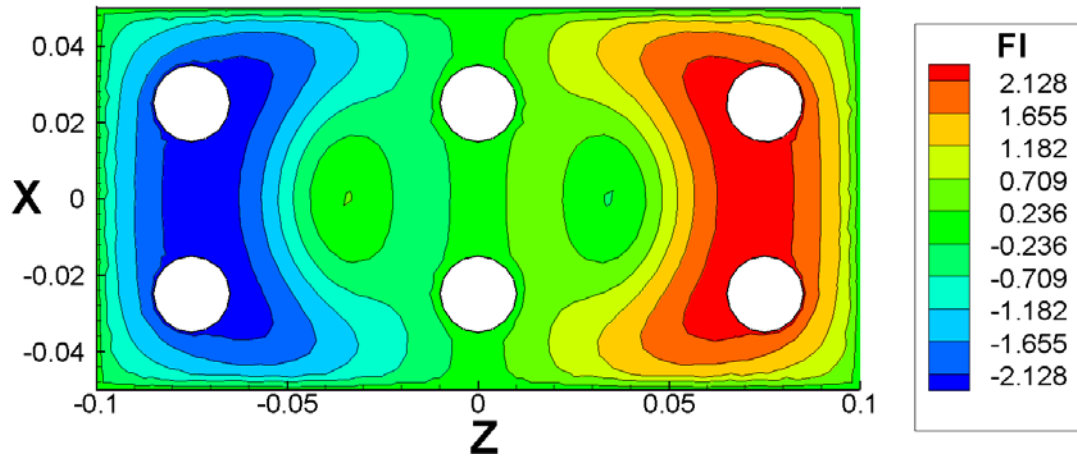


Figure 4.11: Stream function distribution in [A]. All spatial dimensions are given in [m].

The stream function ranges from $\varphi_{\min} = -2.411A$ to $\varphi_{\max} = 2.411A$. As before, we divide this interval into six levels. From it we determine the wire pattern. The wire distribution and the magnetic field created by this wire distribution are shown on Figure 4.12.

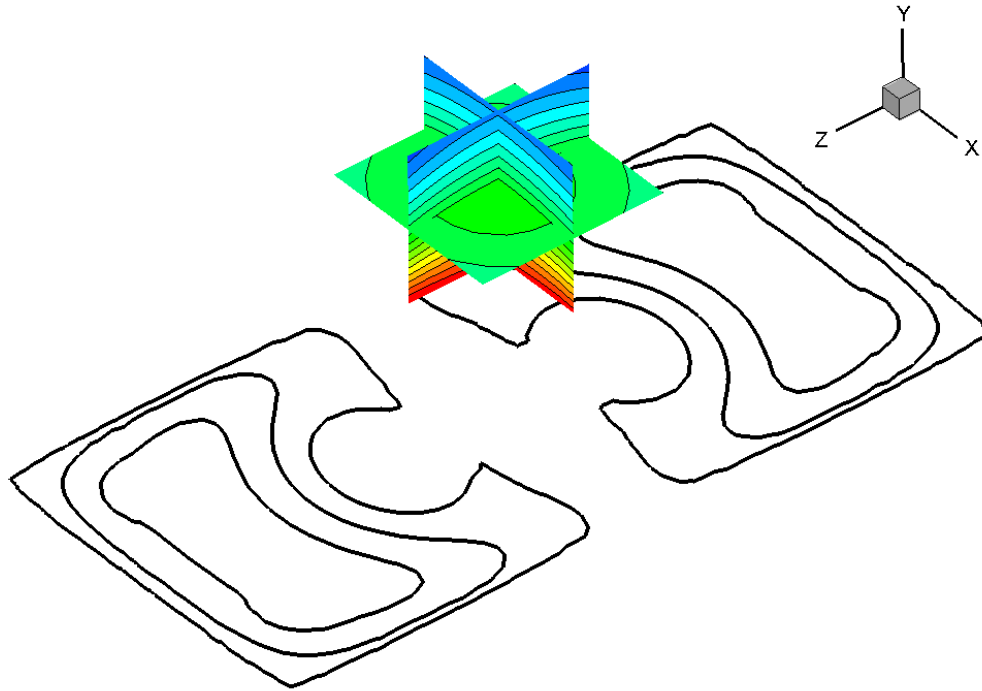


Figure 4.12: Wire pattern of the flat gradient coil and the magnetic flux density in the ROI.

If we use AWG-20 copper wire and assume a resistance of $R=1\Omega$, then each groove contains sixteen turns. A gradient strength of this coil is 17.13 G/cm/100A. The coil inductance is 474 μ H.

To examine the coil performance we choose 5×4×5 cm cube with its center at (0,6,0) cm. Results are shown in the Table 4.

Table 4: Performance of the flat coil shown in Figure 4.12.

	Q_x	U_x
5×4×5 cm cube	0.890	0.302

We notice that the performance of the flat coil is much worse than that of the crescent coil. This can be explained by geometrical reasons: it is much simpler to generate a necessary field distribution if there is a good access to the ROI from both sides.

4.6 Flat Coils

In this section we design and numerically compare the performance of four types of flat gradient coils: (a) G_x gradient coil, (b) G_y gradient coil, (c) unbalanced G_z gradient coil, (d) balanced G_z gradient coil. All four coils have the same mesh shown in Figure 4.13.

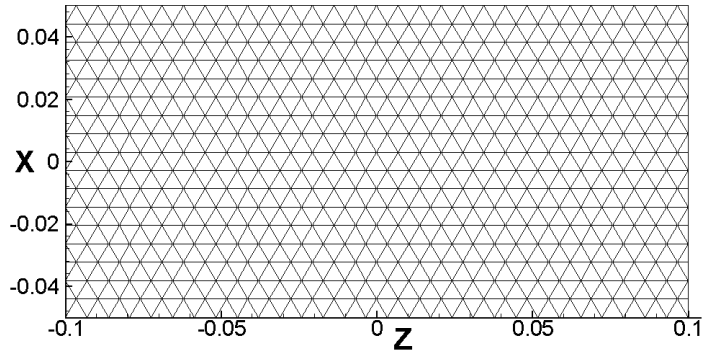


Figure 4.13: Mesh of the flat gradient coil. All dimensions are given in [m].

We prescribe the magnetic field in the ROI of a $6 \times 6 \times 6$ cm cube located 6 cm above the gradient coil. We perform the simulation in the range of α from 10^{-10} to 10^{-4} . Figures 4.14- 4.17 show the evolution of the stream function for G_x , G_y , G_z (unbalanced) and G_z (balanced) gradient coils.

All the coils share a similar dependence on parameter α . When α is small (approximately 10^{-9}), the gradient uniformity term in the cost function Φ dominates. The distribution of the stream function $\varphi(\mathbf{r})$ is more complicated: high frequency spatial harmonics play a significant role. In order to accurately find $\varphi(\mathbf{r})$, we need to use a very refined mesh. Moreover, to approximate the stream function by a discrete wire pattern,

we would need to use higher values of N_{level} (number of subdivisions in the interval $[\varphi_{min}, \varphi_{max}]$). As we move up to higher values of α (approximately 10^{-4}), high spatial frequencies of $\varphi(\mathbf{r})$ decrease and the stream function distribution becomes smoother. As a consequence, we may use lower values of N_{level} to determine the discrete wire pattern.

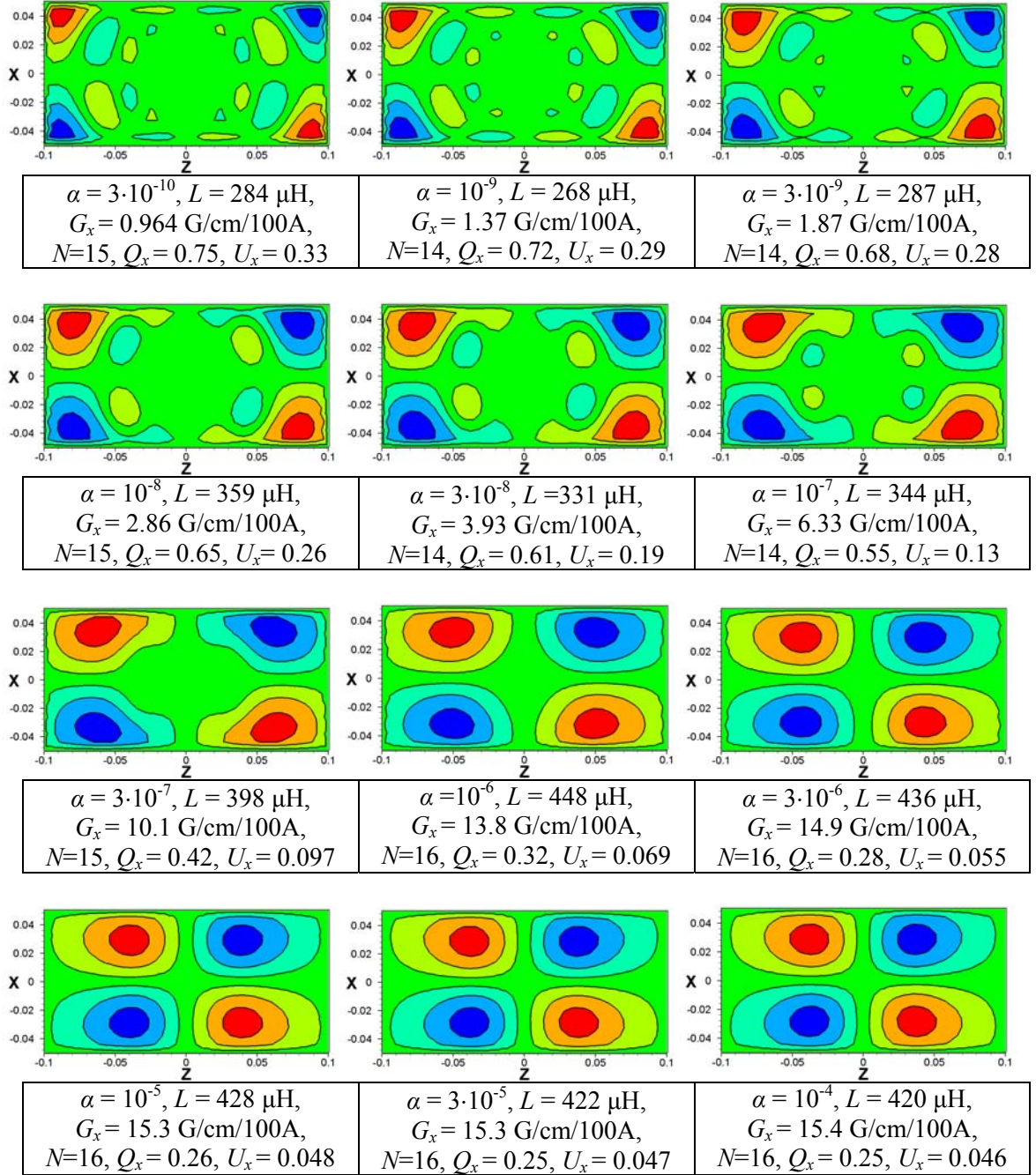


Figure 4.14: G_x gradient coil stream function pattern for different α values. All spatial dimensions are given in [m].

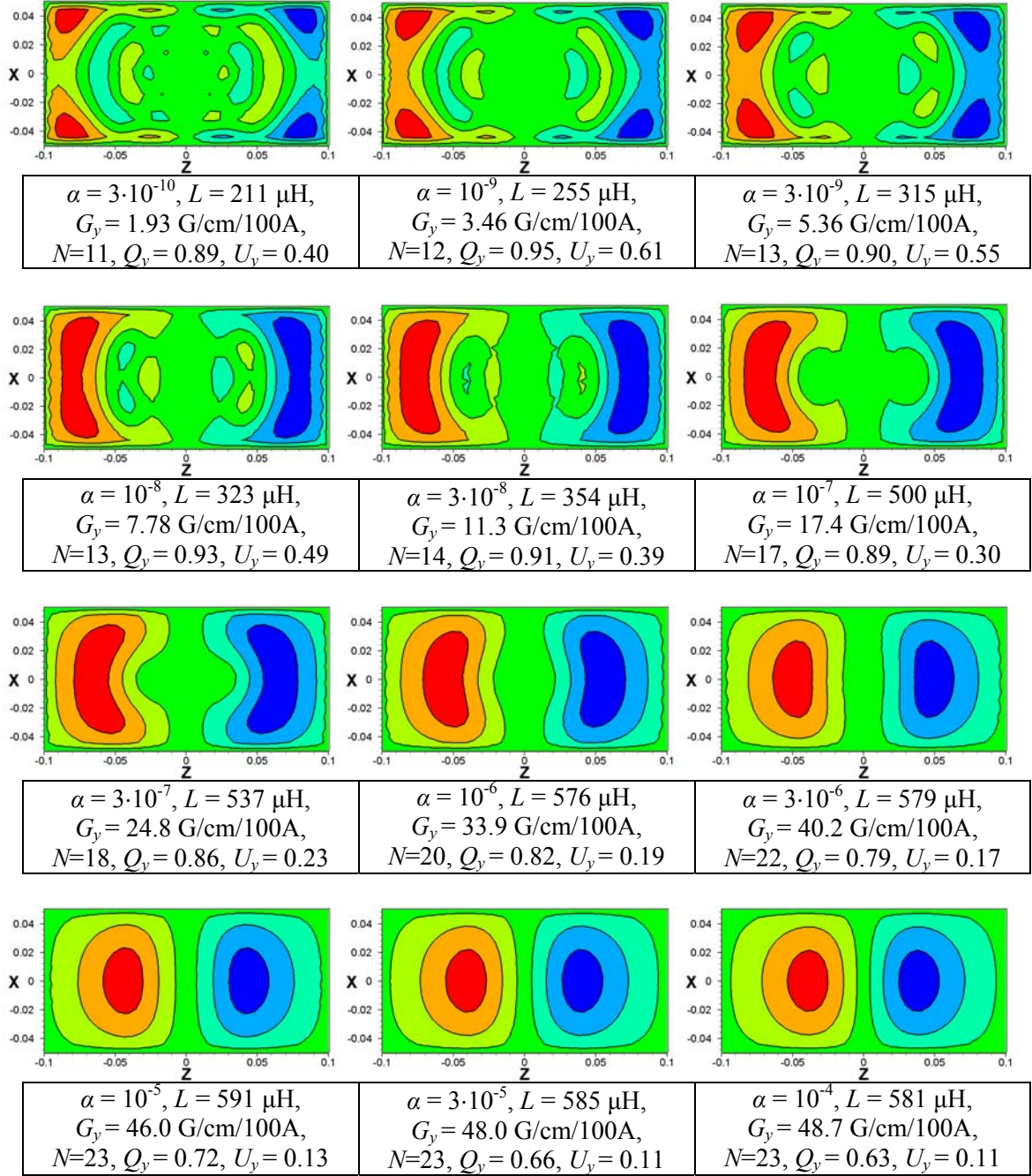


Figure 4.15: G_y gradient coil stream function pattern for different α values. All spatial dimensions are given in [m].

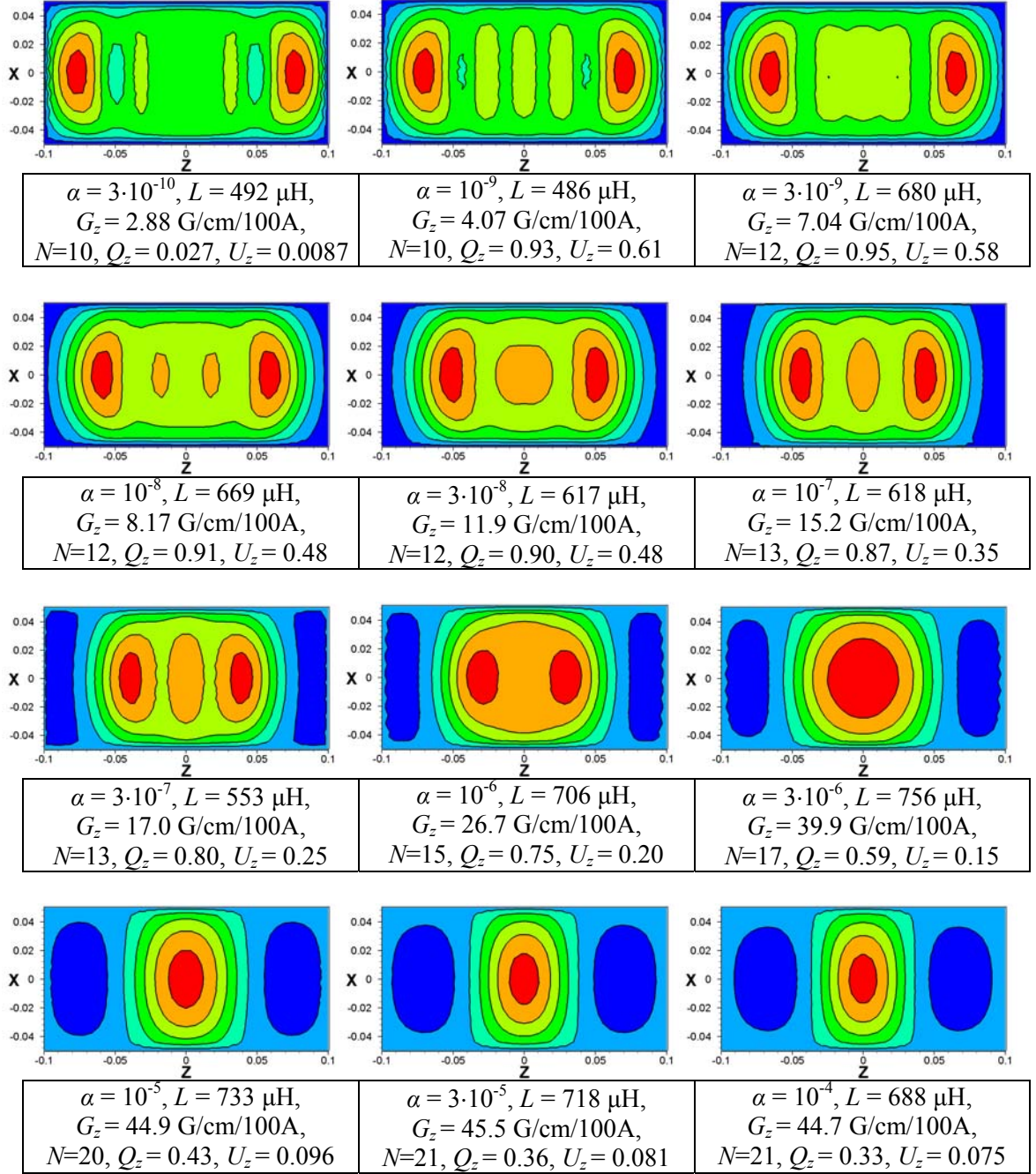


Figure 4.16: G_z unbalanced gradient coil stream function pattern for different α values. All spatial dimensions are given in [m].

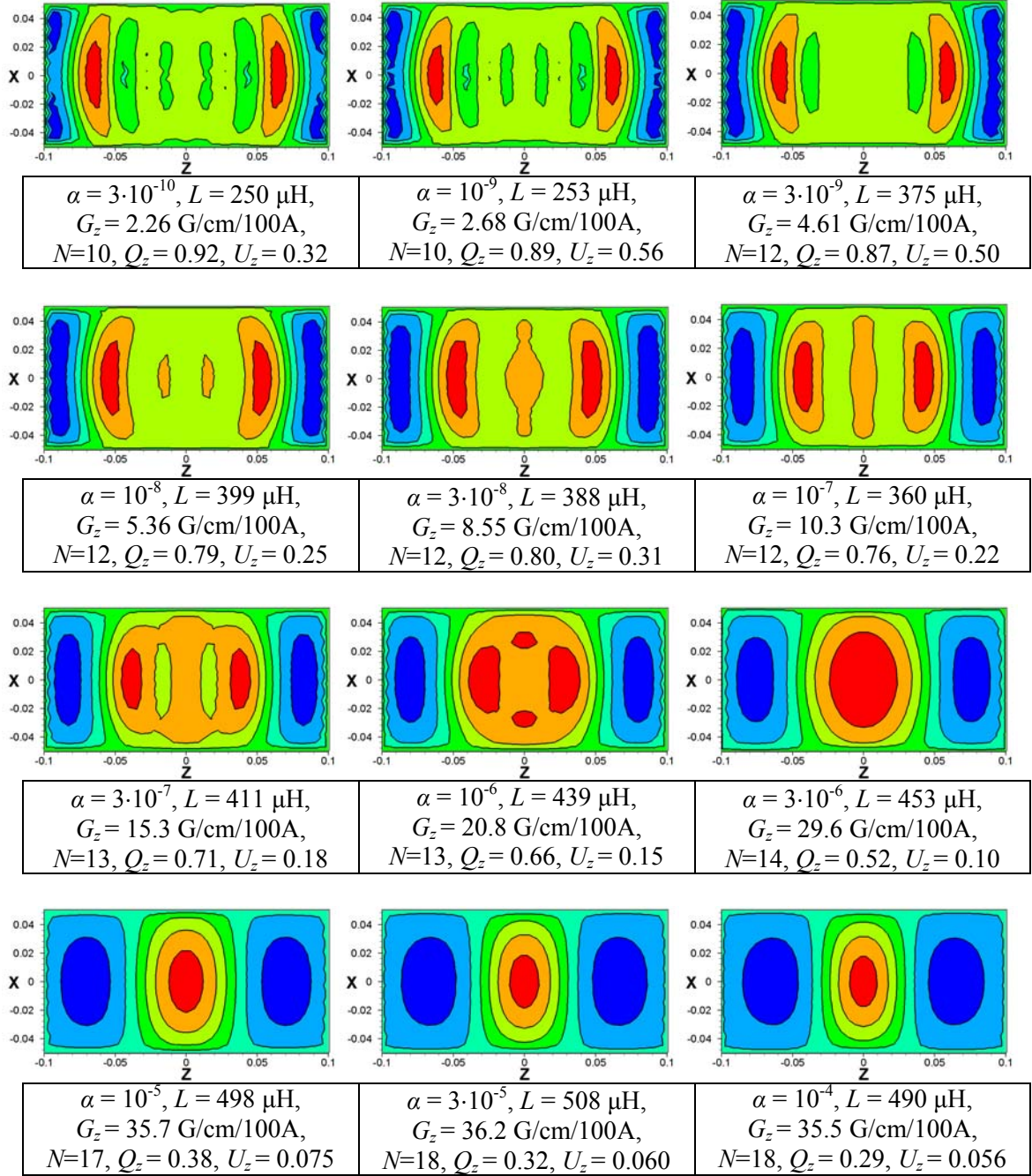


Figure 4.17: G_z balanced gradient coil stream function pattern for different α values. All spatial dimensions are given in [m].

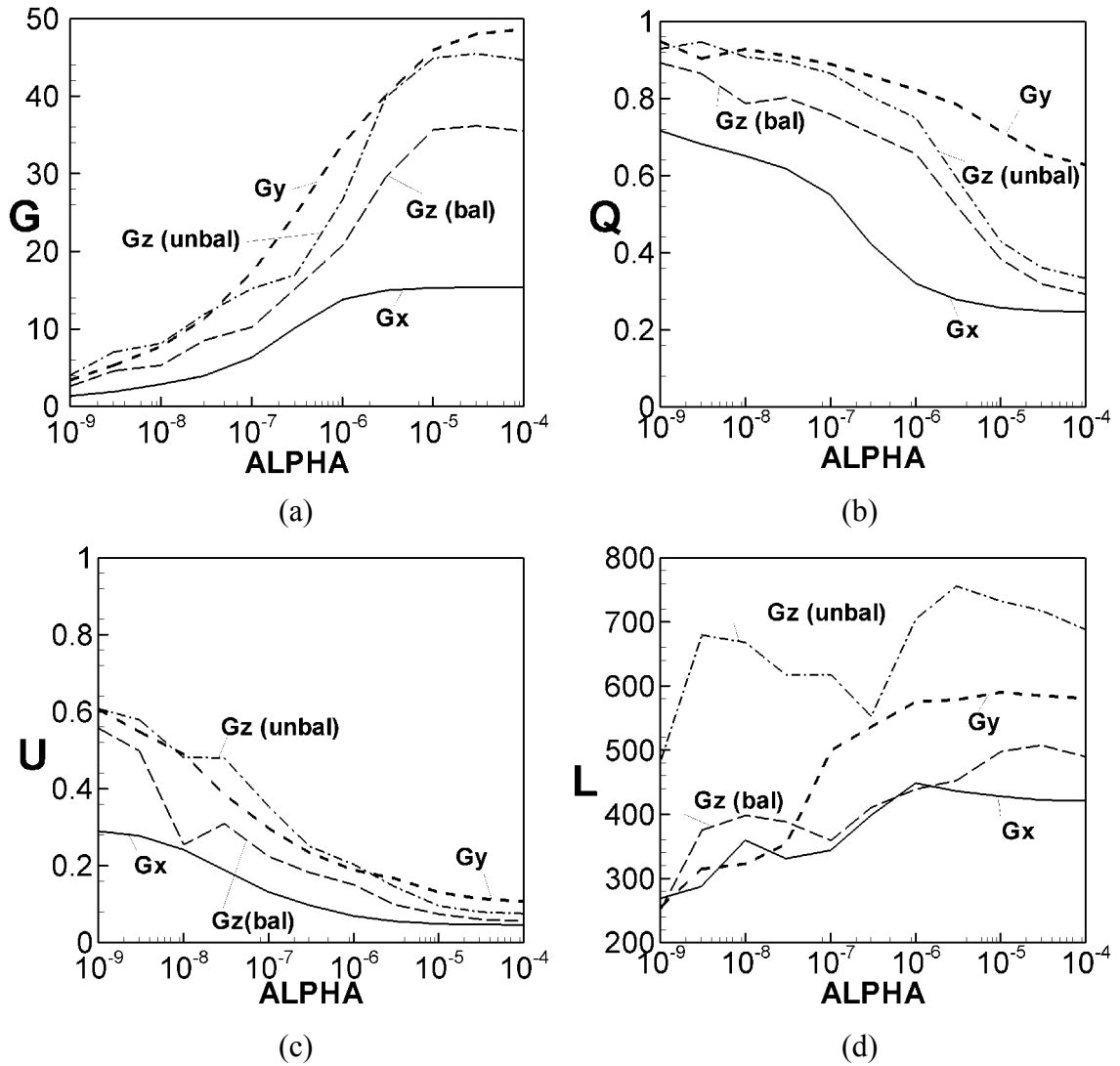


Figure 4.18: Dependence of the gradient coil characteristics on parameter α . (a) Gradient strength G in units of $[G/cm/100A]$, (b) parasitic quality factor Q , (c) gradient uniformity U , (d) inductance L in units of $[\mu H]$.

We recall that for all discrete wire patterns shown in Figures 4.14 – 4.17, we required $R \approx 1.0\Omega$. The following observations can be made based on these figures:

- When decreasing the value of α the wire paths tend to move away from the center of the coil. Conversely, for high α the wire paths are close to the center of the coil.

- This implies that for low α we can expect low values of the field gradient G and high gradient uniformity (high Q and U). For high α , we can expect high field gradient and low gradient uniformity.

Figure 4.18 confirms this prediction. Indeed, when α increases from 10^{-9} to 10^{-4} , the gradient strength increases approximately from $1-4\text{ G/cm/100 A}$ to $15-45\text{ G/cm/100 A}$. At the same time, the value of parasitic quality factor Q drops from $0.70-0.95$ to $0.25-0.65$. Value of field uniformity U drops from $0.30-0.55$ to $0.05-0.10$.

As we observe from these results, G_y and the unbalanced G_z gradient coils provide higher gradients of the magnetic field with higher field uniformity when compared with the G_x and balanced G_z coils. From this we conclude that the given shape is not effective for the G_x coil. Furthermore, there is an apparent trade-off: after forcing the G_z coil to be balanced (torque-free), we lose in gradient strength and field uniformity.

4.7 Comparison of the Least Squares Method and the Stream Function Method

The Stream Function Method uses parameter α to control the balance between gradient strength and gradient uniformity. In Section 4.6, simulations are performed for the flat G_y gradient coil. We can use these results to plot the dependence of the parasitic quality

factor on the gradient strength per unit resistance (see Figure 4.19). This figure also contains results for the four G_y gradient coils considered in Chapter 3.

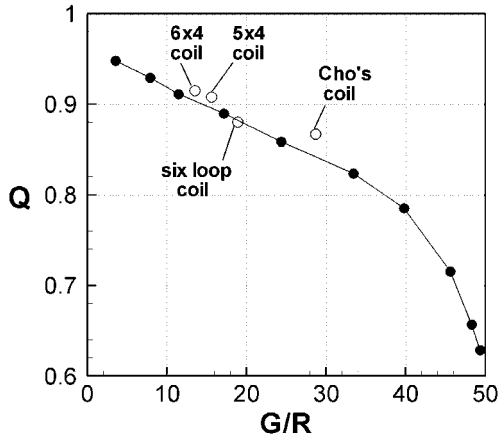


Figure 4.19: Dependence of parasitic quality factor Q on gradient strength per unit resistance $[G/cm/100A/\Omega]$.

We observe that the coils designed in Chapter 3 remain close to the curve that is based on the designs obtained from the Stream Function Method. It once again demonstrates the trade-off between gradient strength and gradient uniformity. A symbol corresponding to the Cho's gradient coil lies higher than the Stream Function curve. A likely explanation of this effect is the following: the Stream Function Method attempts to minimize the magnetic energy (inductance) of the coil, while the Least Squares Method does not have any control over the coil's inductance. The inductance per unit resistance squared for the Stream Function Method (approx. $550 \mu H/\Omega^2$) is better than the same value for the Cho's coil (approx. $1080 \mu H/\Omega^2$). In general, coils designed by the Stream Function Method are characterized by lower values of inductance.

4.8 Shielding

In this paragraph we introduce a secondary coil (shield) in the design. Specifically, we consider the structure depicted in Figure 4.20. The need for a shielded design is well documented as the eddy currents induced in the main bore of the magnet can significantly affect the gradient uniformity.

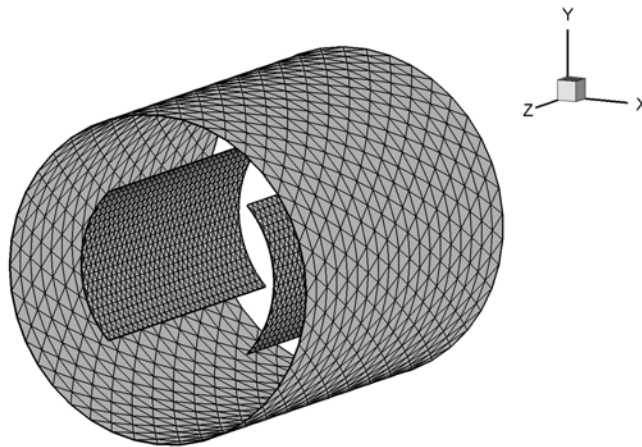


Figure 4.20: Primary and secondary coils.

The primary coil (crescent coil) is located inside the secondary coil (cylindrical coil) and is the same configuration as the coil shown in Figure 4.7. It consists of two plates of size 20×10 cm each and with radius $R = 6.5$ cm. The secondary coil is a cylinder of 25 cm in length and 10 cm in radius.

In our first simulation we use $\alpha = 10^{-7}$ and $\beta = 0$. The results of this simulation for the G_x coil are shown in Figure 4.21.

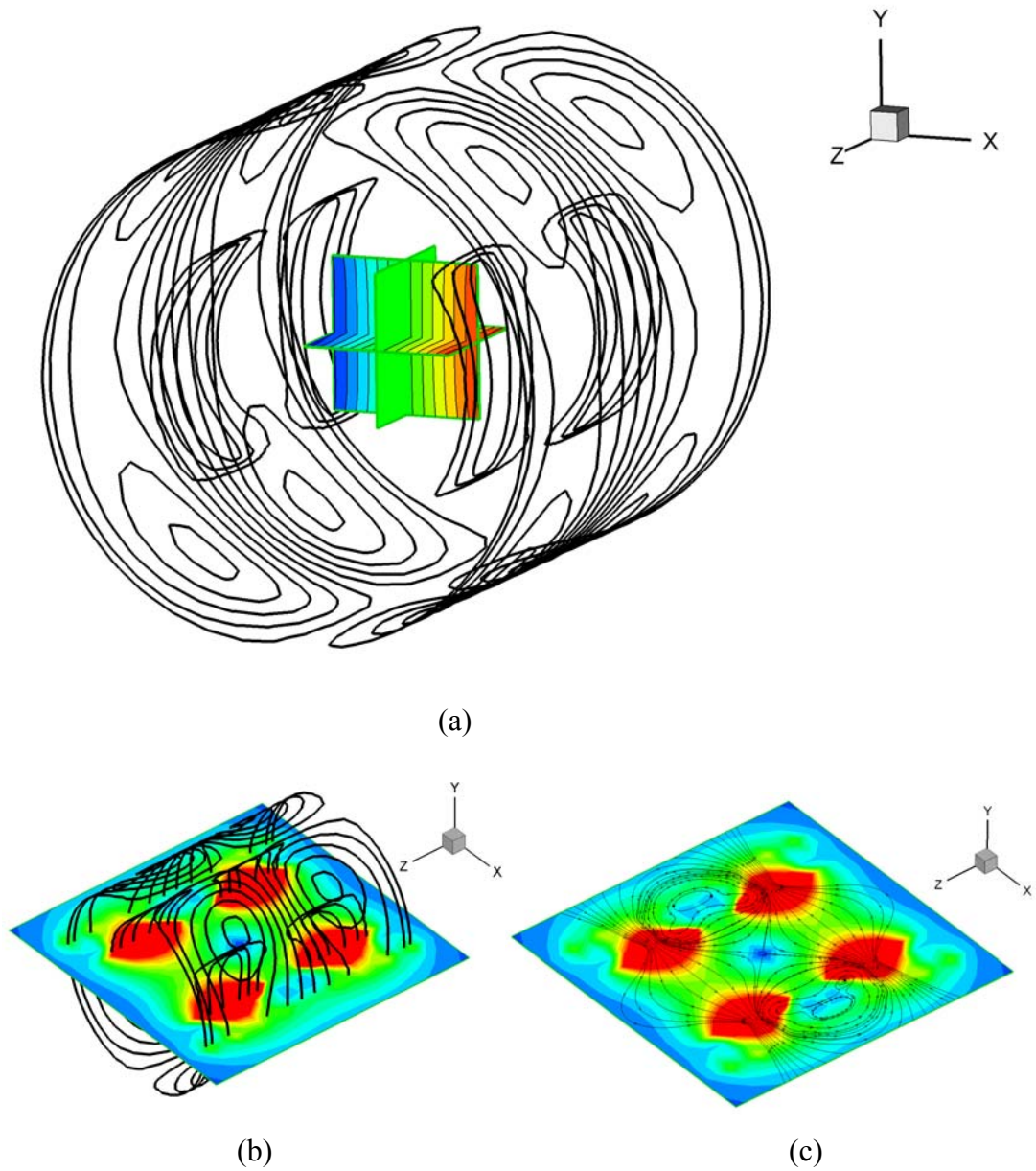


Figure 4.21: G_x coil with $\alpha = 10^{-7}$ and $\beta = 0$. (a) Wire pattern and z -component of the magnetic flux density, (b) wire pattern and absolute value of magnetic flux density, (c) streamlines of the magnetic flux density.

We see that these results differ from the results obtained with the primary coil only, see Figure 4.7. The degree of shielding is controlled by parameter β . The shielded coil has the following parameters: $G_x = 41.12 \text{ G/cm/100A}$, resistance equals 1.0Ω (primary),

and 1.1Ω (secondary), and the inductance is $485 \mu\text{H}$. There are nine AWG-20 wires in each groove of the primary coil, and three AWG-20 wires in each groove of the secondary coil. The values for the field uniformity in a $6 \times 6 \times 6$ cm ROI are $Q_x = 0.967$ and $U_x = 0.471$. In this example, the shielding is effectively “turned off” because $\beta = 0$. It is important to understand that simply putting β to zero does not force the currents in the shield to become zero: the shield still participates in creating the prescribed magnetic field in the ROI. Currents flowing in the secondary coil “help” to produce the required linear magnetic field.

In our second example we use parameters $\alpha = 10^{-7}$ and $\beta = 0.1$. By using the non-zero value of β we attempt to limit the magnetic flux through the surface of the secondary coil. Results of these simulations are shown in Figure 4.22.

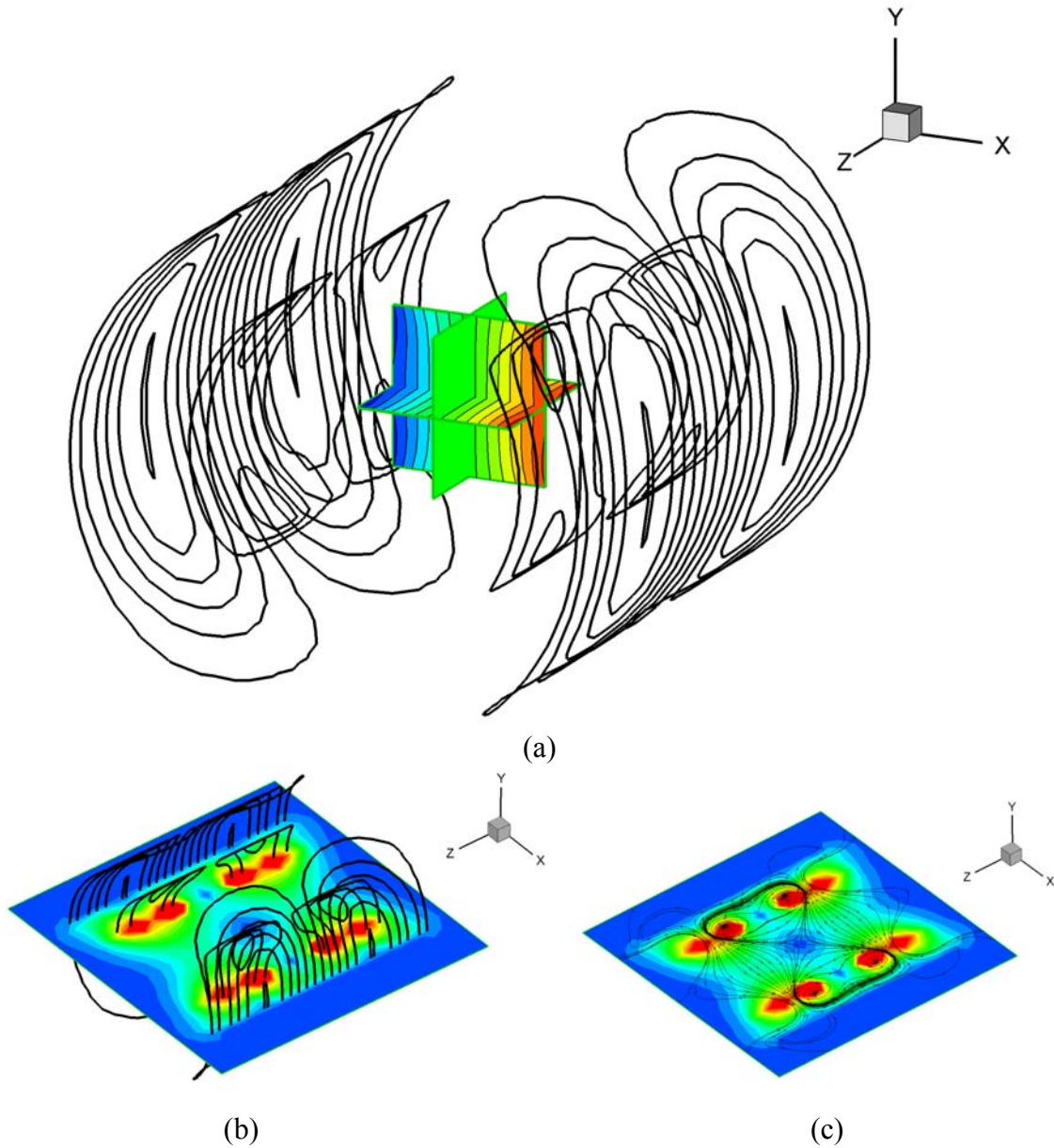


Figure 4.22: G_x coil with $\alpha = 10^{-7}$ and $\beta = 0.1$. (a) Wire pattern and z -component of the magnetic flux density, (b) wire pattern and absolute value of magnetic flux density, (c) streamlines of the magnetic flux density.

The coil has the following parameters: $G_x = 23.91 \text{ G/cm/100A}$, resistance equals $0.98 \text{ } \Omega$ (primary), and $0.29 \text{ } \Omega$ (secondary), and the inductance is $227 \text{ } \mu\text{H}$. There are nine AWG-20 wires in each groove of the primary coil, and one AWG-20 wire in each groove

of the secondary coil. The values for the field uniformity in a $6 \times 6 \times 6$ cm ROI are $Q_x = 0.927$ and $U_x = 0.318$. We observe that only a few magnetic field lines leave the secondary coil. As an attempt to measure the shielding effect we compare the magnetic field outside the secondary coil, for example, at a point (0.15, 0, 0) cm. The ratio of the absolute values of the magnetic field for the shielded coils with $\beta = 0.1$ and $\beta = 0$ is 0.0061. In other words, the magnetic field for the coil shown in Figure 4.22 is only 0.61% of the magnetic field for coil shown in Figure 4.21. Moreover, the ratio of the absolute values of the magnetic field for the shielded coil with $\beta = 0.1$ and a coil without a shield (see Figure 4.9) is 0.0177, i.e the shielding degree is 1.77 %. That is the magnetic field for coil shown in Figure 4.22 is 1.77 % of the magnetic field for coil shown in Figure 4.9. As we see, the introduction of a non-zero β helps to retain the magnetic field inside the secondary coil. As a disadvantage, the coil with $\beta = 0.1$ yields a lower gradient G_x and lower values of field uniformity Q_x and U_x . Also, we notice that the coil with $\beta = 0.1$ has a lower inductance, which makes it easier to switch.

Table 5: Effects of the shield on the performance of the crescent gradient coil.

Coil	G_x [G/cm/100A]	R , [Ω], (primary + secondary)	L , [μH]	Q_x	U_x
Crescent unshielded (Figure 4.9).	27.96	1.035+0	263	0.943	0.366
Crescent shielded with $\beta = 0$ (Figure 4.21). Shielding effect is zero.	41.12	1.014+1.098	484	0.967	0.471
Crescent shielded with $\beta = 0.1$ (Figure 4.22).	23.91	0.980+0.293	227	0.927	0.318

We observe that the shielding effect is achieved at the expense of lower gradient strength and lower gradient uniformity.

4.9 Graphic User Interface

Originally, a console version of the code for the gradient coil design was developed. As an output, it produces data files suitable for viewing in TECPLOT software. TECPLOT is a scientific data visualization software from Amtec (www.amtec.com). To make the code user-friendlier we decided to create a GUI for the coil designing software (Gradient Coil Designer).



Figure 4.23: Gradient Coil Designer.

As a first step, we create a new project document and give it a name, for example, “coil.grd”. After this we proceed to menu “Geometry” and choose either to load an external a mesh file or to create one of five possible meshes:

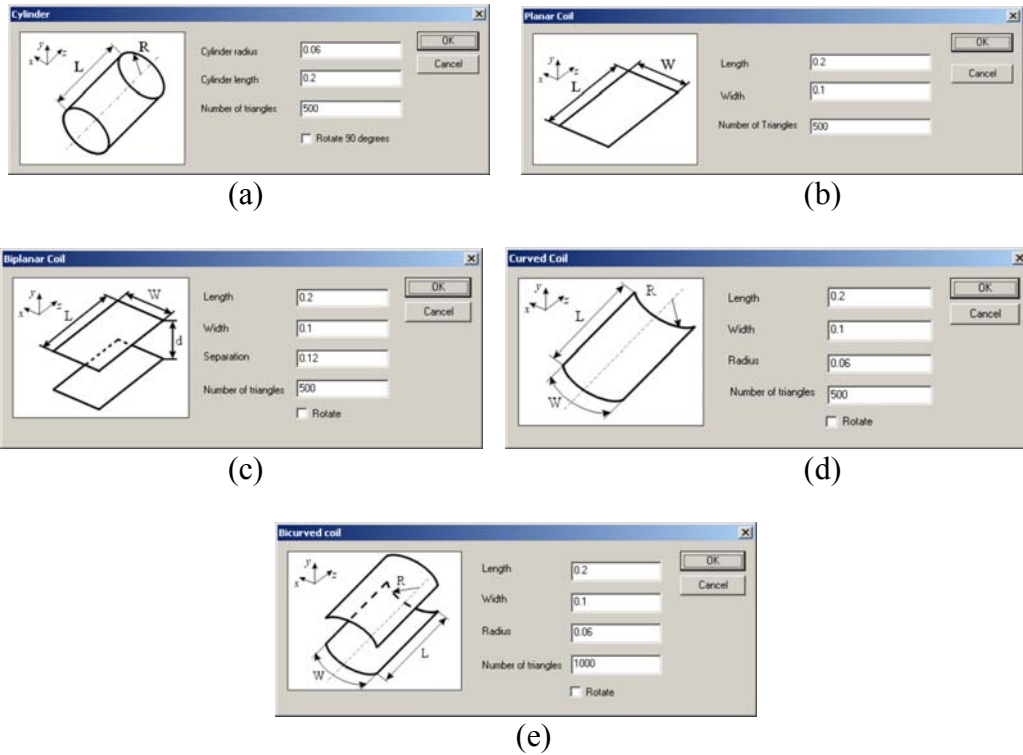


Figure 4.24: Five typical gradient coil configuration templates.

For instance, if we create a biplanar coil with 0.2 m in length, 0.1 m in width, 0.12 m separation between the plates, and with approximately 1000 triangle patches, option Figure 4.24(c) yields the mesh shown in Figure 4.25.

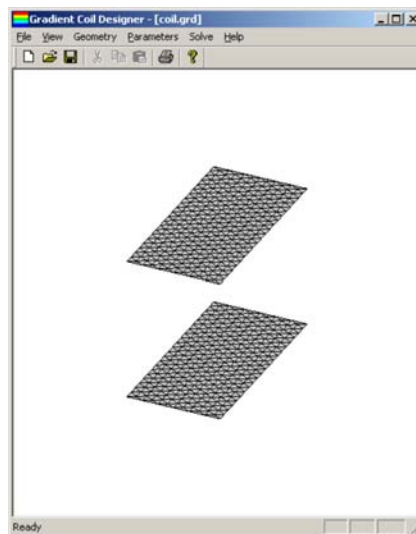
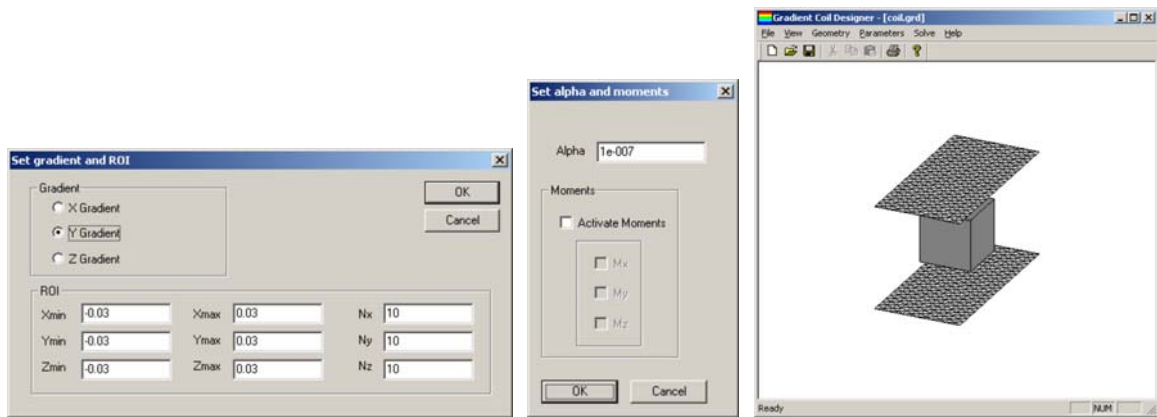


Figure 4.25: Biplanar mesh based on template Figure 4.24(c).

After creating the mesh we can invoke menu “Parameters / Gradient”. In the dialog window we choose “Y-Gradient”. We set the region of interest as $x_{\min}=-0.03$ m, $x_{\max}=0.03$ m, $y_{\min}=-0.03$ m, $y_{\max}=0.03$ m, $z_{\min}=-0.03$ m, $z_{\max}=0.03$ m. The number of points in x , y , z directions are by default set to $N_x = N_y = N_z = 10$. We then go to “Parameters / Moment” and set $\alpha = 10^{-7}$. As a result, we will be able to see the Region of Interest.



(a) (b) (c)
Figure 4.26: (a) Gradient dialog window, (b) moment dialog window, (c) region of interest.

After submitting all these settings, we can execute the program (menu “Solve / Run”) to obtain the distribution of the stream function shown in Figure 4.27.

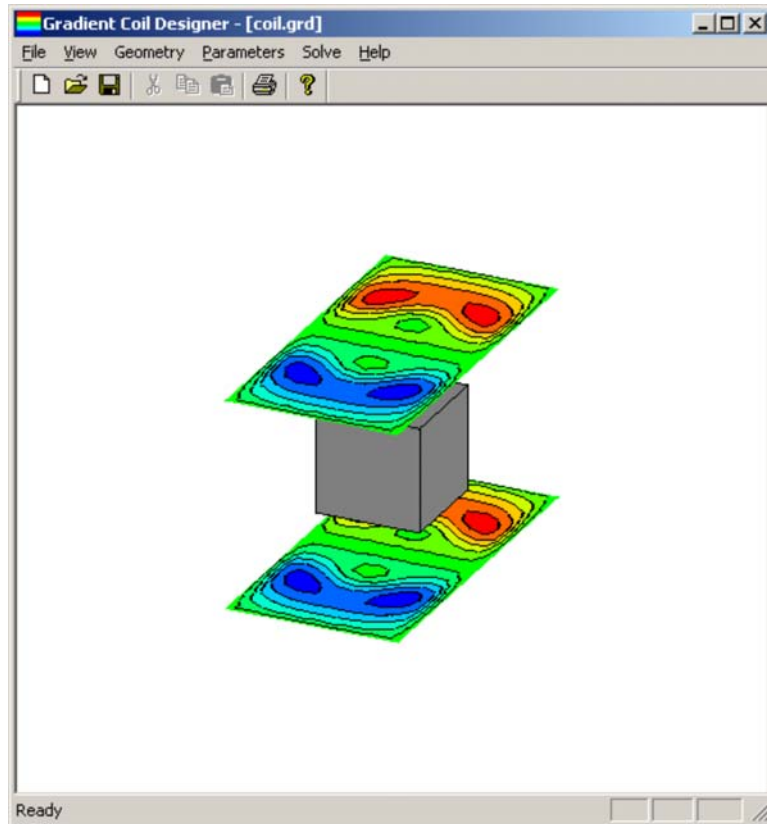


Figure 4.27: Stream function distribution over the coil surface.

After the stream function is established, we go to “Solve / Postprocessing”, enter AWG of 20, resistance of 1.0Ω , and number of levels 6.

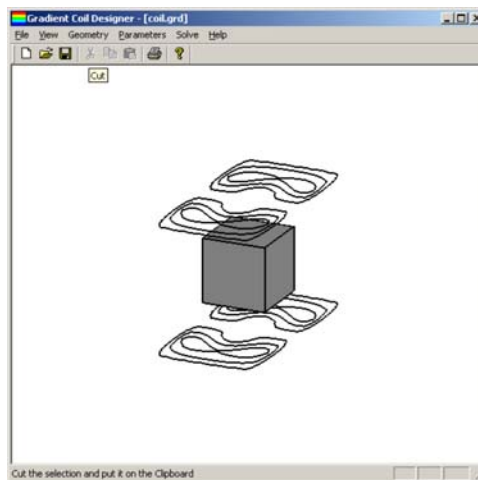


Figure 4.28: Layout of the gradient coil.

In this example the current flow on the surface is approximated by six levels of the stream function. We next go to “Solve / Magnetic Field” and enter the region where we desire to find the z -component of the magnetic field. By default, it is the same as the Region of Interest.

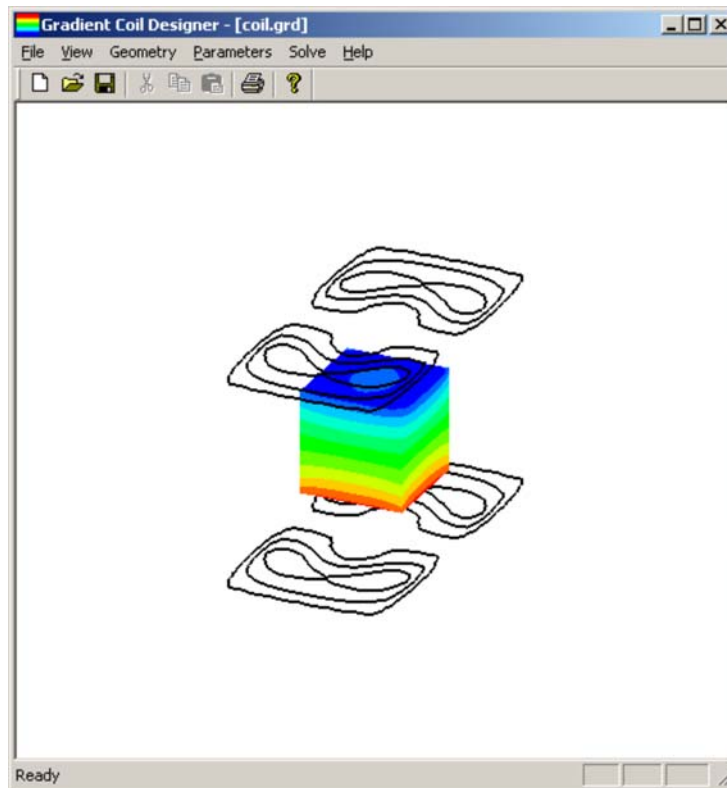


Figure 4.29: z -component of the magnetic flux density in the Region of Interest.

On each face of the cube we observe the distribution of the magnetic field. This helps us to judge the magnetic field uniformity. Also, the program creates files “info1.dat”, “info2.dat” and “info3.dat”. They contain the information about input and output parameters. For example, for this coil, we obtain $G_y=24.58$ G/cm/100A, $R=1.034$ Ω , $L=249$ μ H, number of turns is nine, $Q_y=0.934$, $U_y=0.362$.

The Graphical User Interface simplifies the interaction with the program. However, it can be executed only under Windows platform, in contrary to the console version (both Windows and Unix). Finally, the current GUI version does not provide us with the possibility of changing the weight function $W(\mathbf{r}_k)$. Also, this version does not have a shielding option. Even though all these programming issues can be addressed at a later time, the development of GUI is not the main topic of our research.

4.10 Coil Construction

To test the presented ideas, a set of gradient coils has been constructed and tested in a commercial MRI scanner.

(a) G_x coil

For the G_x coil we have machined a G-10 cylindrical former with 6" OD (15.24 cm), 5" ID (12.7 cm), 1' length (30.48 cm). The grooves are milled in the outer surface of the former. The groove depth is chosen to be 6 mm and the width is 4 mm. The copper wiring is approximately in the middle of the groove (3 mm from the outer surface). The radius of the copper wiring is therefore $15.24\text{cm}/2 - 0.3\text{cm} = 7.32\text{ cm}$. Each plate has the size of $24 \times 12\text{cm}$. For the coil simulations, the following parameters are used: ROI of $8 \times 8 \times 8\text{ cm}$ in the center of the cylinder, parameter $\alpha = 10^{-7}$, weight function $1 + \frac{2|x|}{4\text{cm}}$, and wire gauge of AWG-20. Six levels of the stream function are employed as seen in Figure 4.30.

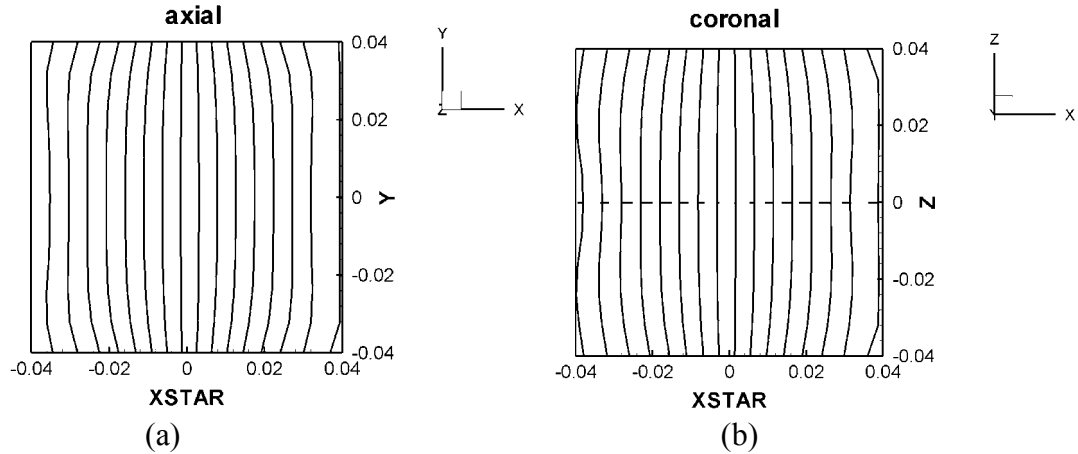


Figure 4.31: Distortions of the G_x coil, (a) axial plane, (b) coronal plane. All dimensions are given in [m].

The simulations provide us with the following coil parameters: resistance of $R=1.14\Omega$, inductance of $L=260\ \mu\text{H}$, eight AWG-20 wires are in each groove, and the gradient strength of $G=21.4\ \text{G/cm}/100\text{A}=2.14\ \text{mT/m/A}$. The measured values of resistance and inductance are $R=1.18\Omega$ and $L=268\ \mu\text{H}$. The grooves were milled in the cylindrical G-10 former as shown in Figure 4.32.

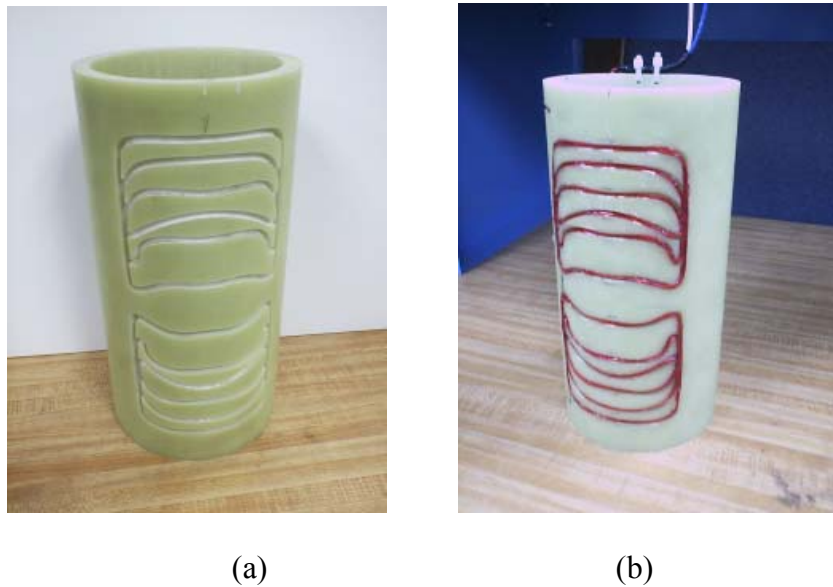


Figure 4.32: (a) Former of the G_x coil, (b) wiring in the G_x coil former.

(b) G_y coil

For the G_y coil we chose a cylindrical acrylic former with 7" OD (17.78 cm), 6.25" ID (15.88 cm), 1' length (30.48 cm). The grooves are again milled in the outer surface of the former. The groove depth is chosen to be 4 mm, and the width is 3 mm. The copper wiring is approximately 3 mm deep from the outer surface. The radius of the copper wiring is therefore $17.78\text{cm}/2 - 0.3\text{cm} \approx 8.60\text{ cm}$. For the coil simulations, the following parameters are used: ROI of $6 \times 6 \times 6\text{ cm}$ in the center of the cylinder, parameter α is $3 \cdot 10^{-8}$, weight function $1 + \frac{|z|}{3\text{cm}}$, and wire gauge is AWG-20. Twelve levels of the stream function are employed, as depicted in Figure 4.33.

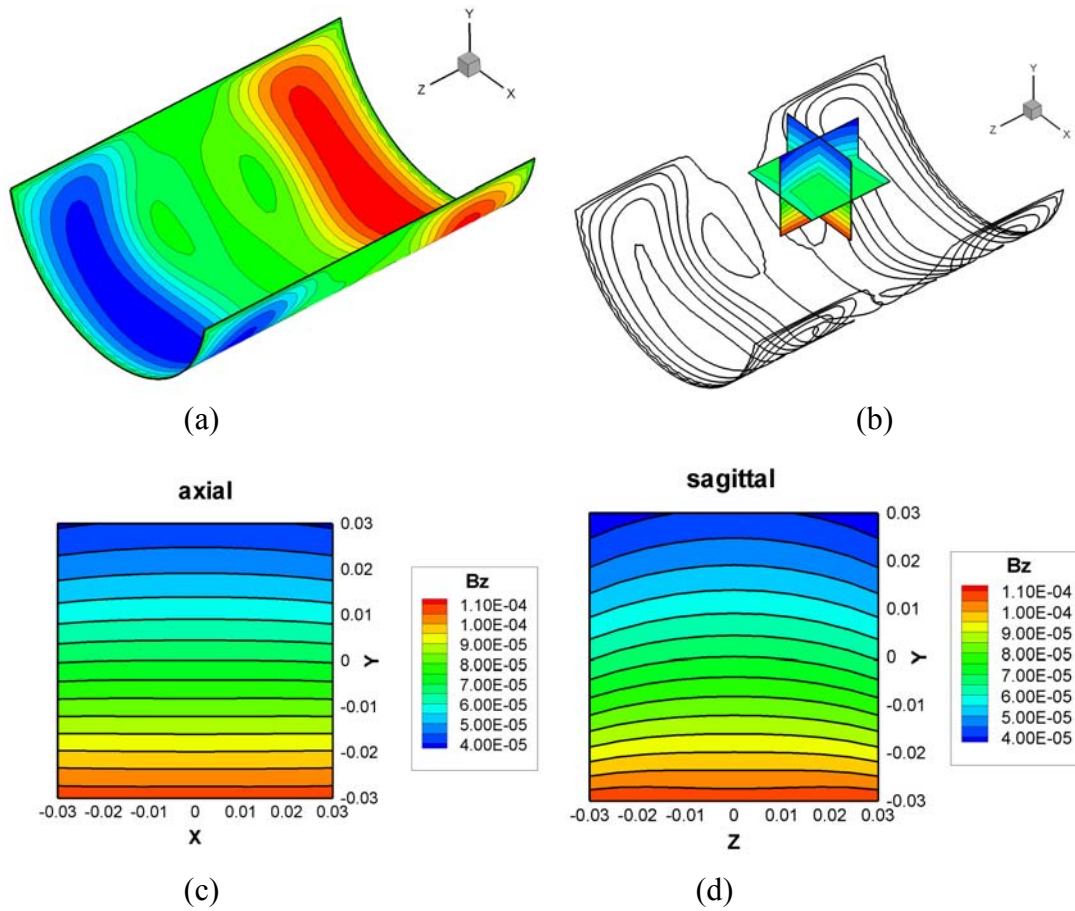


Figure 4.33: G_y coil, (a) stream function distribution, (b) wiring and magnetic flux density B_z [T], (c) magnetic flux density B_z [T] in the axial plane, (d) magnetic flux density B_z [T] in the sagittal plane. All spatial dimensions are in [m].

Figure 4.34 shows the distortions introduced by the G_y gradient coil. We observe that the distortions in the xy -plane are significant. This arises from the fact that the G_y coil is intrinsically non-symmetrical.

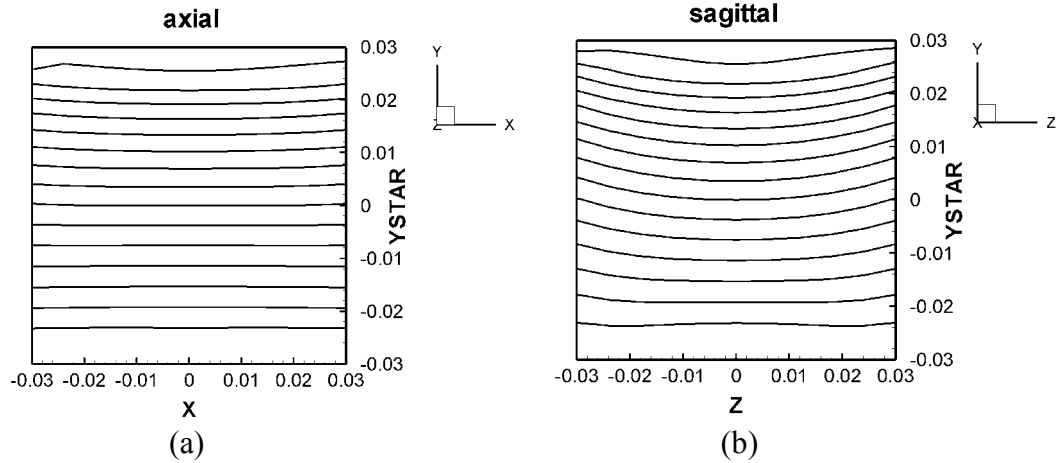


Figure 4.34: Distortions of the G_y coil, (a) axial plane, (b) sagittal plane. All dimensions are given in [m].



Figure 4.35: Wirings of G_y and G_z coils in the acrylic former.

The simulations yield the following coil parameter results: resistance of $R=1.14\Omega$, inductance of $L=318\ \mu\text{H}$, five AWG-20 wires in each groove, and the gradient strength of $G=11.7\ \text{G/cm}/100\text{A}=1.17\ \text{mT/m/A}$. The measured values of resistance and inductance

are: $R=1.20 \Omega$, $L=327 \mu\text{H}$. The grooves were milled in the cylindrical acrylic former as shown in Figure 4.35.

(c) G_z coil

The G_z coil was placed on the same former as the G_y coil: 7" OD (17.78 cm), 6.25" ID (15.88 cm). The grooves are again milled in the outer surface of the former. The groove depth was chosen to be 4 mm and the width was 4 mm. The copper wiring is approximately 3 mm deep from the outer surface. The radius of the copper wiring is the same as for the G_y coil: $17.78\text{cm}/2-0.3\text{cm} \approx 8.60 \text{ cm}$. For the coil simulations, the following parameters are used: ROI of $6 \times 6 \times 6 \text{ cm}$ is in the center of the cylinder, parameter $\alpha = 3 \cdot 10^{-8}$, weight function is unity, and wire gauge is AWG-20. Three levels of the stream function are used (see Figure 4.36).

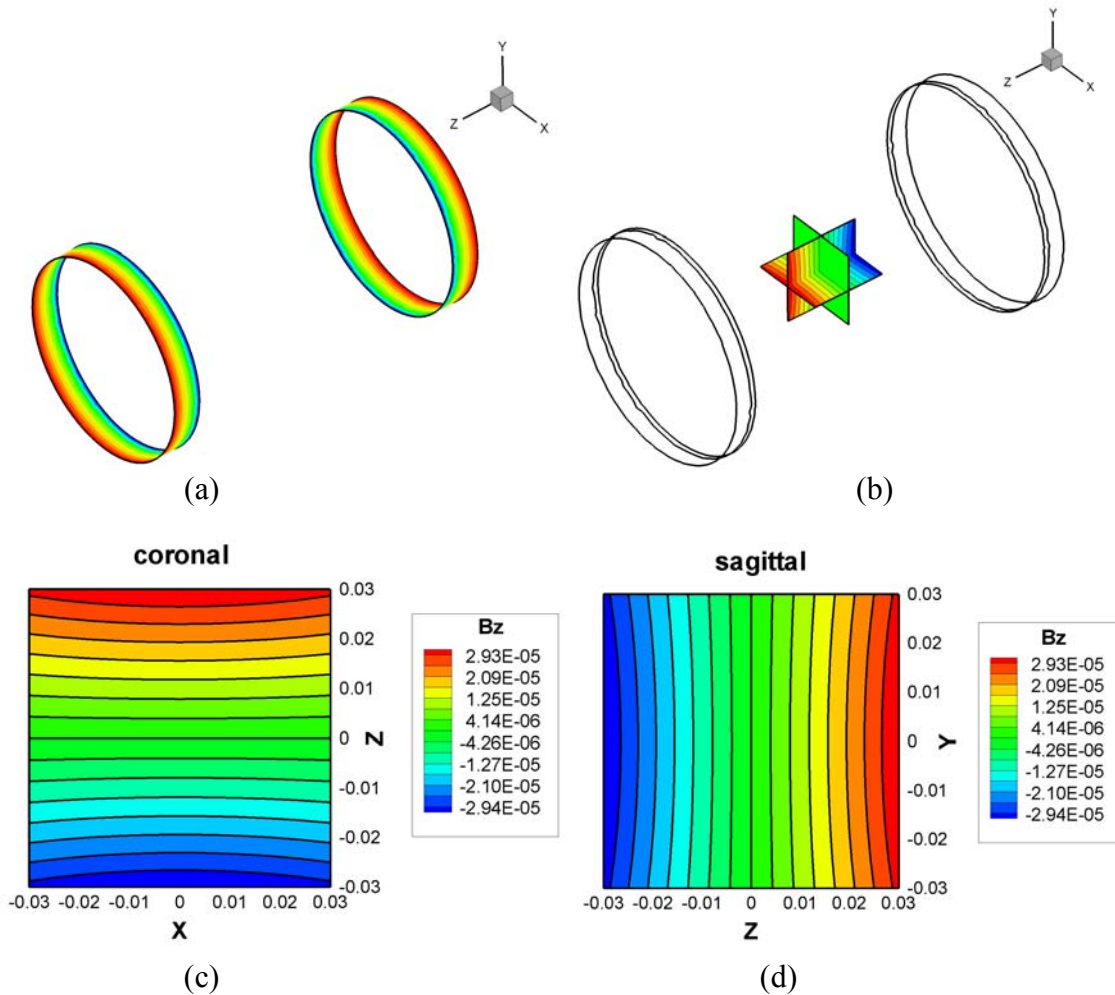


Figure 4.36: G_z coil, (a) stream function distribution, (b) wiring and magnetic flux density B_z [T], (c) magnetic flux density B_z [T] in the xz -plane, (d) magnetic flux density B_z [T] in the yz -plane. All spatial dimensions are in [m].

Figure 4.37 shows the distortions introduced by the G_z gradient coil in the xz and yz planes.

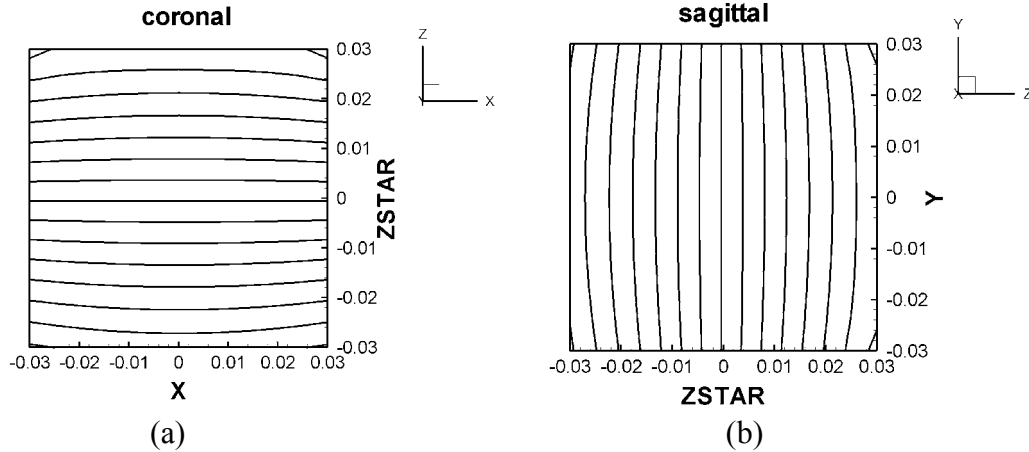


Figure 4.37: Distortions of the G_z coil, (a) coronal plane, (b) sagittal-plane.

The simulations yield the following coil parameters: resistance of $R=1.08\ \Omega$, inductance of $L=556\ \mu\text{H}$, ten AWG-20 wires are placed in each groove, and the gradient strength is $G=10.6\ \text{G/cm}/100\text{A}=1.06\ \text{mT/m/A}$. The measured values of resistance and inductance are $R=1.16\ \Omega$ and $L=575\ \mu\text{H}$. The grooves are cut in the cylindrical acrylic former as shown in Figure 4.35.

The performance characteristics of all three gradient coils are summarized in the Table 6 below:

Table 6: Characteristics of the manufactured coils.

	G , [G/cm/100A]	R , [Ω]	L , [μH]	Q (ROI $3\times 3\times 3$ cm)	U (ROI $3\times 3\times 3$ cm)
G_x coil	21.4	1.18	268	0.981	0.632
G_y coil	11.7	1.20	327	0.909	0.384
G_z coil	10.6	1.16	575	0.970	0.707

We observe that the G_x gradient coil has the strongest field. This can be explained by the fact that this coil has a smaller radius, i.e. the wiring is closer to the ROI. The G_y coil has the lowest field uniformity because of its shape: this coil accesses the ROI only from one side.

4.11 Experimental Results

The three individual gradient coils were combined into a single gradient set as shown in Figure 4.38.



Figure 4.38: Photographs of the gradient set.

This coil design was tested in a commercial 4.7T Bruker MRI scanner with 40cm bore, as shown in Figure 4.39.

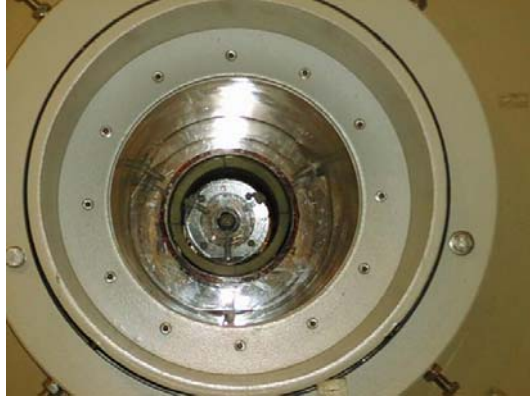


Figure 4.39: Gradient coil set in the magnetic bore.

The electric performance of the coils is tested by applying rectangular current pulses to the gradient coils as seen in Figure 4.40.

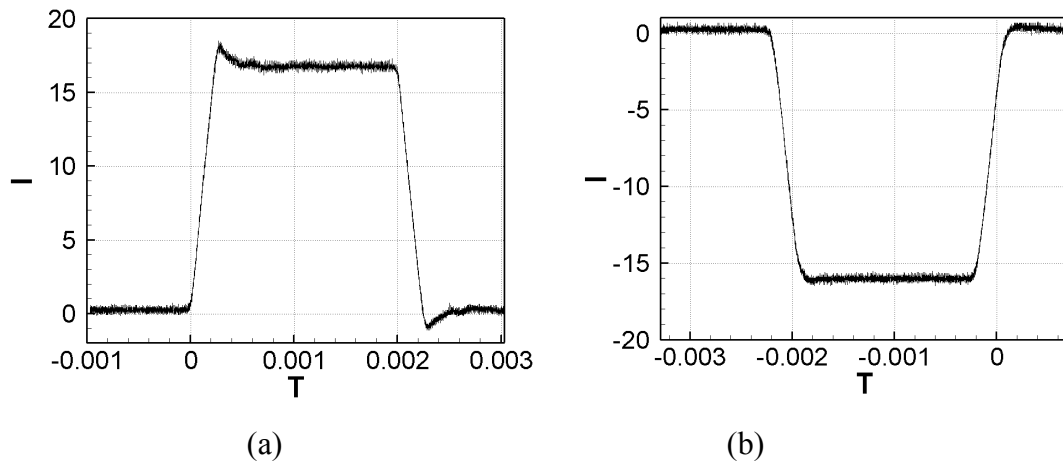


Figure 4.40: (a) Pulse applied to the G_y gradient coil, (b) pulse applied to the G_z gradient coil. Current is measured in [A]. Time is given in [s].

Both coils demonstrate a rise time that compares well with their respective time constants $\tau = L/R$. For the G_y gradient coil it is $\tau = 280 \mu\text{s}$, and for the G_z gradient coil it is $\tau = 500 \mu\text{s}$.

The first set of experiments is performed with a phantom shown in Figure 4.41. A dual coil RF system (volume coil and surface coil) is used during the experiment. The surface coil with the phantom is put in the volume coil and the entire setup is placed into

the gradient coil set as seen in Figure 4.39. Phantom is a water-filled tube of length 4.5” and of diameter 1”.



Figure 4.41: Phantom used in the experiment.

The MR parameters for this set of experiments are: matrix size is 256×256 , pulse sequence is spin echo, acquisition time is 1 min 4 sec, $T_R = 250$ ms, $T_e = 15$ ms, slice thickness is 2 mm, and one averaging is applied. The RF surface coil is employed as a receiver coil.

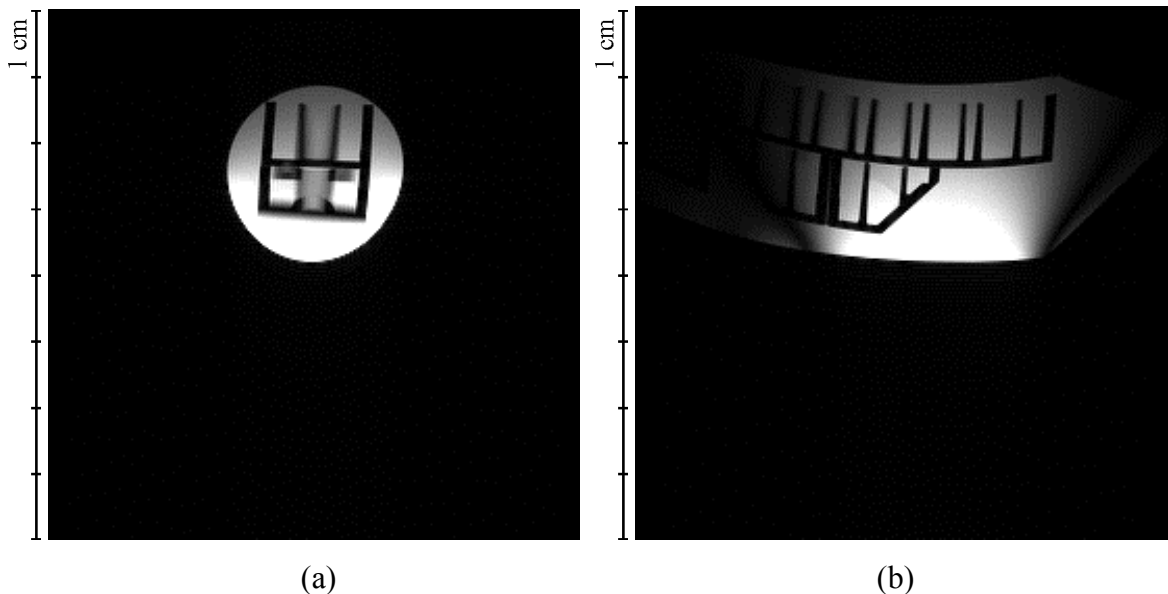


Figure 4.42: Image of the phantom (Figure 4.41) with the surface coil as a receiver coil (a) axial plane (xy -plane), (b) sagittal plane (yz -plane).

In a second experiment the surface coil was disconnected and the RF volume coil was used as transmit/receive coil. The image of the phantom is shown in Figure 4.43.

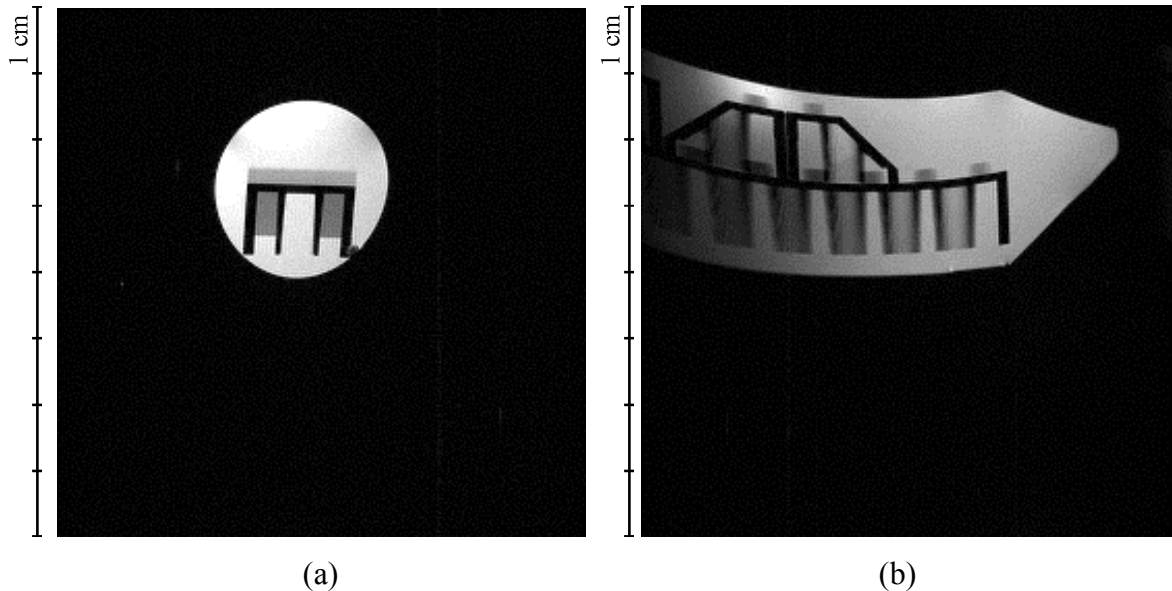


Figure 4.43: Image of the phantom (Figure 4.41) with the volume coil as the receiver coil (a) axial plane (xy -plane), (b) sagittal plane (yz -plane).

It is interesting to compare the image shown in Figure 4.43(b) with the theoretically predicted figure of distortions shown in Figure 4.34(b). For this purpose, we superimpose these two images as shown in Figure 4.44.

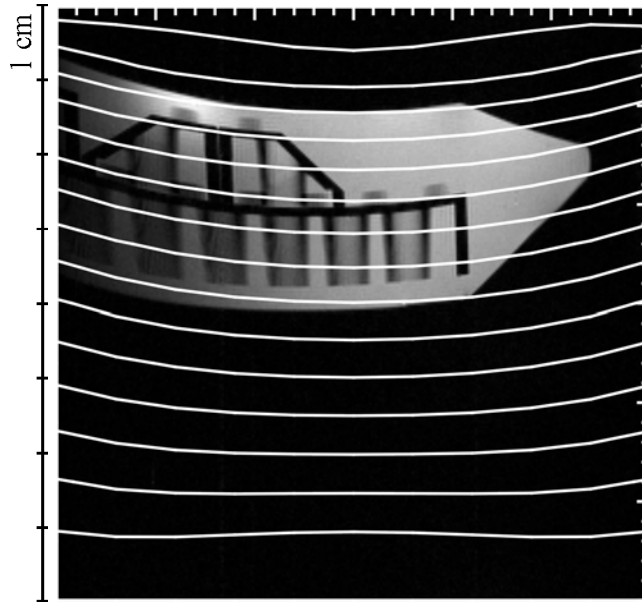


Figure 4.44: Superposition of the image of the phantom (Figure 4.41) with the figure of distortions in a sagittal plane (yz -plane).

We notice that the curvature of the phantom compares well with the curvature of the constant field lines.

In the third experiment we used a spin echo pulse sequence to image a rat brain (see Figure 4.45). The parameters for this experiment are the same as the ones used for the phantom: matrix is 256×256 , pulse sequence is spin echo sequence, acquisition time is 1 min 04 sec, $T_R = 250$ ms, $T_e = 15$ ms, slice thickness is 2 mm, and one averaging. The first image shows the axial plane, the second image shows the sagittal plane.

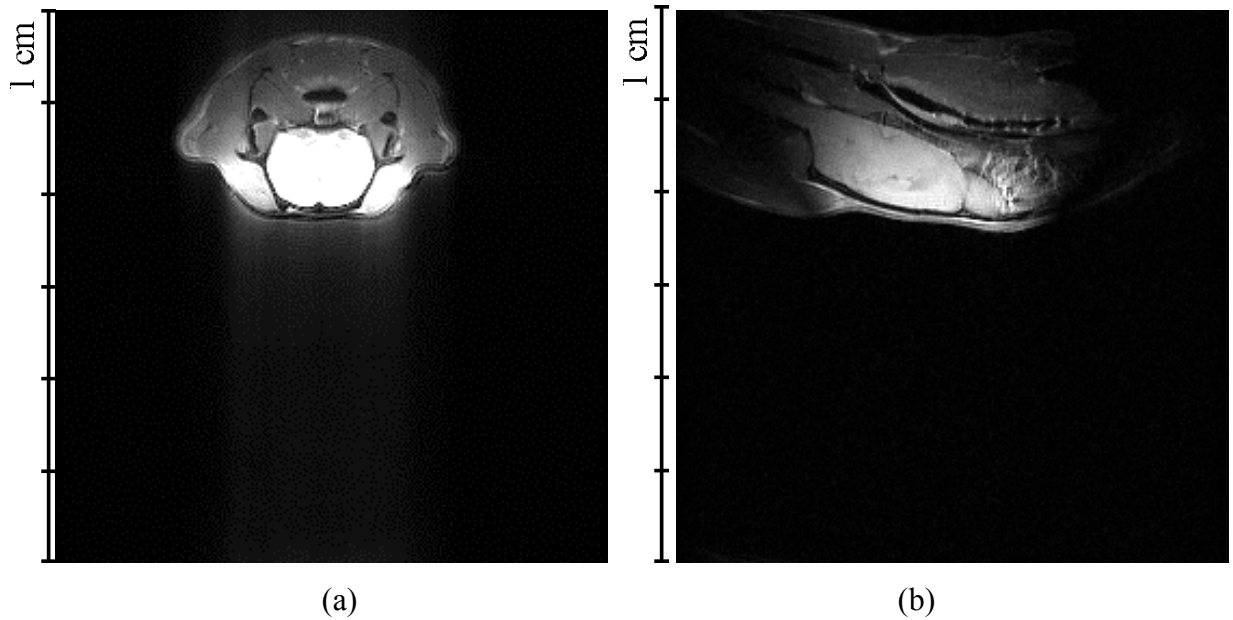


Figure 4.45: Image of the rat with the surface coil as the receiver coil (a) axial plane (xy -plane), (b) sagittal plane (yz -plane).

The fourth experiment involves a fast spin echo sequence (see Figure 4.46). Parameters for this experiment are: matrix size is 256×256 , fast spin echo sequence, four echoes per excitation, acquisition time is 2 min 12 sec, $T_R = 2$ s, $T_e = 60$ ms, slice thickness is 1.4 mm.



Figure 4.46: Image of the rat with the surface coil as the receiver coil in the axial plane.

4.12 Chapter Summary

This chapter presents a new stream function method for the design of single- and multi-surface gradient coils. The method is formulated and implemented in such a form as to make it applicable to a wide variety of shapes and geometries. As soon as the triangular mesh of the chosen structure is established, it can be fed into the design algorithm in order to find all possible rotational current elements. Values of all these individual currents are optimized to minimize the cost function, which is the combination of the gradient uniformity term, the magnetic energy term, and a shielding term. As an option, torque-free coils can be designed by considering corresponding Lagrange multipliers. The wire paths are laid out along the chosen levels of the stream function. Given the size

of the wire and the desired resistance, the coil inductance and the magnetic field strength are automatically determined. To demonstrate the success of the theoretical approach, two crescent (both shielded and unshielded) G_x gradient coils and flat gradient coils are designed.

A console version of the general-purpose program for the gradient coil design is developed and successfully tested. To ease the interaction with the program, a graphic user interface is developed. Results from the program can be directly used for automatic machining of the coil.

To verify this approach and reduce it to practice, three coils (G_x , G_y , G_z) have been designed, manufactured and tested. For each one of the three coils, the calculated values of resistance and inductance demonstrate good agreement with the measured ones.

Chapter 5

Formulation of Method of Moments for Arbitrary-Shaped Surfaces and Inhomogeneous Biological Bodies

This chapter proposes a new frequency domain formulation for the Method of Moments that is capable of simultaneously incorporating highly conductive surfaces and biological entities. Both surfaces and 3D bodies are discretized into triangular patches for the surfaces and tetrahedra for the volume. To describe current flow over the surface we employ Rao-Wilton-Glisson basis functions as discussed in 5.2.2 .

For the case of 3D biological bodies, solenoidal (divergence-free) basis functions are employed. The numerical predictions obtained by this new formulation compare very well with a canonical analytic solution of an EM wave incident upon a dielectric sphere.

5.1 Theoretical Considerations

In order to solve the set of Maxwell equations, scalar and vector potentials Φ and \mathbf{A} are introduced to describe the electric field \mathbf{E} and the magnetic flux density \mathbf{B} :

$$\mathbf{E} = -\nabla\Phi - j\omega\mathbf{A}, \quad \mathbf{B} = \nabla \times \mathbf{A}. \quad (5.1)$$

In free space, the solutions for the potentials under the Lorentz gauge assumption are readily found in the form

$$\mathbf{A}(\mathbf{r}) = \frac{\mu_0}{4\pi} \int_{V'} \frac{\mathbf{J}(\mathbf{r}') e^{-jk|\mathbf{r}-\mathbf{r}'|}}{|\mathbf{r}-\mathbf{r}'|} dV', \quad \Phi(\mathbf{r}) = -\frac{1}{4\pi\epsilon_0 j\omega} \int_{V'} \frac{\nabla' \cdot \mathbf{J}(\mathbf{r}') e^{-jk|\mathbf{r}-\mathbf{r}'|}}{|\mathbf{r}-\mathbf{r}'|} dV'. \quad (5.2)$$

In an effort to deal with 3D biological bodies, a new, but powerful vector field representation can be introduced by defining a special vector $\tilde{\mathbf{J}} = j\omega(\mathbf{D} - \epsilon_0\mathbf{E}) + \mathbf{J}$. This allows Ampere's law to be re-written in the form:

$$\nabla \times \mathbf{H} = j\omega\epsilon_0\mathbf{E} + j\omega(\mathbf{D} - \epsilon_0\mathbf{E}) + \mathbf{J} = j\omega\epsilon_0\mathbf{E} + \tilde{\mathbf{J}}, \quad (5.3)$$

where vector $\tilde{\mathbf{J}}$ plays the role of an equivalent current density. Based on the definition of this new vector $\tilde{\mathbf{J}}$ one concludes that the solution for potentials is given by:

$$\mathbf{A}(\mathbf{r}) = \frac{\mu_0}{4\pi} \int_{V'} \frac{\tilde{\mathbf{J}}(\mathbf{r}') e^{-jk|\mathbf{r}-\mathbf{r}'|}}{|\mathbf{r}-\mathbf{r}'|} dV', \quad \Phi(\mathbf{r}) = -\frac{1}{4\pi\epsilon_0 j\omega} \int_{V'} \frac{\nabla' \cdot \tilde{\mathbf{J}}(\mathbf{r}') e^{-jk|\mathbf{r}-\mathbf{r}'|}}{|\mathbf{r}-\mathbf{r}'|} dV'. \quad (5.4)$$

From (5.1) we state that the electric field is given by:

$$\mathbf{E}(\mathbf{r}) = \frac{1}{4\pi\epsilon_0 j\omega} \int_{V'} \nabla' \cdot \tilde{\mathbf{J}}(\mathbf{r}') \nabla \varphi(\mathbf{r}, \mathbf{r}') dV' - j\omega \frac{\mu_0}{4\pi} \int_{V'} \tilde{\mathbf{J}}(\mathbf{r}') \varphi(\mathbf{r}, \mathbf{r}') dV', \quad (5.5)$$

where $\varphi(\mathbf{r}, \mathbf{r}') = \frac{e^{-jk|\mathbf{r}-\mathbf{r}'|}}{|\mathbf{r}-\mathbf{r}'|}$ is the free-space Green's function. For the subsequent

discussion, we are considering three types of objects: a current carrying ring excitation loop, a conductive surface, and a 3D biological body as generically depicted in Figure 5.1. The current loop is employed to act as a finite source that excites the system.

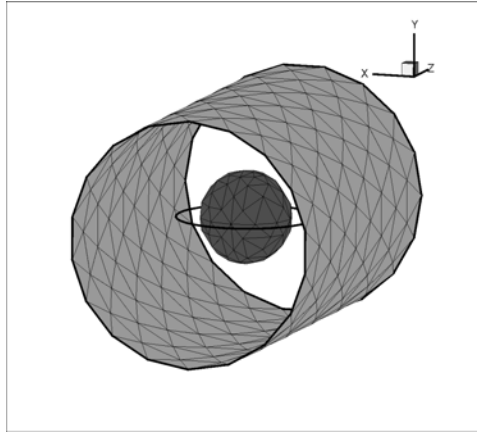


Figure 5.1: Generic problem configuration featuring conductive surface, a ring excitation (current loop), and a biological body.

As explained in detail below, the excitation loop can be subdivided into line segments, the surface can be discretized into triangular patches, and the 3D body can be discretized into tetrahedra.

5.2 Basis Functions

5.2.1 Discretization of a thin wire

All points and line intervals are uniquely enumerated and a 1D current element consists of one line interval. In this formulation, the number of elements is the same as the number of intervals. The convention is such that current flows from the left to the right point of the line interval as shown in Figure 5.2.



Figure 5.2: 1D current element with current flow direction.

We associate a basis function $\mathbf{f}_n^L(\mathbf{r})$ with each of the elements. The function is defined as a unit vector directed from the left point to the right point. Mathematically, this fact can be expressed by the expression:

$$\mathbf{f}_n^L(\mathbf{r}) = \frac{\mathbf{l}}{|\mathbf{l}|}, \quad (5.6)$$

where \mathbf{l} is the vector directed from left point to right point. The basis function \mathbf{f}_n^L is used to approximate the interval current. The total current flow in the entire loop Ω is therefore approximated as

$$\mathbf{J}^L = \sum_{n=1}^N I_n^L \mathbf{f}_n^L(\mathbf{r}), \quad (5.7)$$

where I_n^L is the net current (in [A]) through connected edges, \mathbf{J}^L is vector of current (in [A]), N is the number of elements.

5.2.2 Discretization of a perfectly conductive surface

Here again, all points, edges and triangles are uniquely enumerated. We next consider a generic RWG element n as consisting of two triangles, referred to as “left” T_n^+ and “right” T_n^- , and sharing a common edge. In this formulation the number of elements is equal to the number of non-boundary edges. Current flows from the left vertex point to the opposite edge of the triangle. It then passes to the edge of right triangle and converges into right vertex point as illustrated in Figure 5.3.

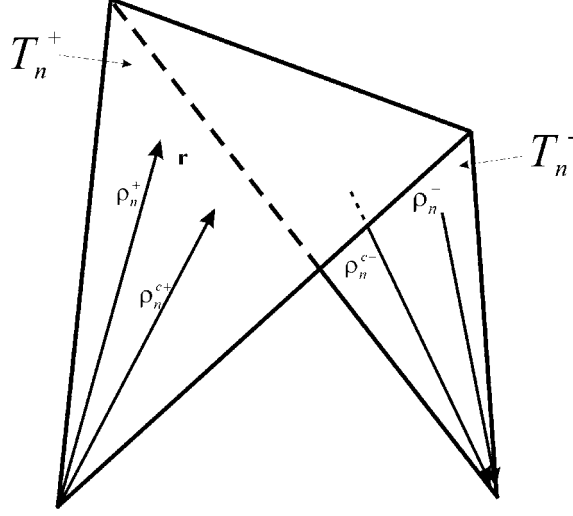


Figure 5.3: RWG current element consisting of two triangles T_n^+ and T_n^- and sharing a common edge. The vectors ρ_n^\pm and $\rho_n^{c\pm}$ reside in the surfaces A^\pm and refer to observation and centroid points, respectively.

We now associate a basis function $\mathbf{f}_n^S(\mathbf{r})$ with each of the surface elements. For the left triangle T_n^+ it is defined as a vector field radially diverging from the left vertex point. On the right triangle T_n^- it is a vector field radially converging into right vertex point.

Mathematically, this fact can be expressed by the following expression

$$\mathbf{f}_n^S(\mathbf{r}) = \begin{cases} \left(\frac{1}{2A_n^+}\right) \cdot \rho_n^+ & \mathbf{r} \text{ in } T_n^+ \\ \left(\frac{1}{2A_n^-}\right) \cdot \rho_n^- & \mathbf{r} \text{ in } T_n^- \\ 0, & \text{otherwise} \end{cases}, \quad (5.8)$$

where A_n^\pm is the area of triangle T_n^\pm . It is noted that subscripts refer to elements, while superscripts refer to triangles. The basis function \mathbf{f}_n^S is used to approximately represent the surface current. In other words, current is flowing from the left to the right triangle. The surface divergence of \mathbf{f}_n^S , which is proportional to the surface charge density associated with the basis element, is

$$\nabla_S \mathbf{f}_n^S = \begin{cases} 1/A_n^+ \mathbf{r} & \text{in } T_n^+ \\ -1/A_n^- \mathbf{r} & \text{in } T_n^- \\ 0, & \text{otherwise} \end{cases} \quad (5.9)$$

The surface current density on S may be approximated as

$$\mathbf{J}^S = \sum_{n=1}^N I_n^S \mathbf{f}_n^S(\mathbf{r}), \quad (5.10)$$

where I_n^S is the net current (in Amperes) through connected edges, \mathbf{J}^S is vector of the surface current (in [A/m]), N is the number of elements.

5.2.3 Discretization of a 3D body

Here again we can discretize the body into tetrahedra and enumerate all the points, edges, and faces in a similar manner as before. A solenoidal element consists of all tetrahedra sharing the same edge. The basis function associated with the edge \mathbf{l} is only non-zero in each tetrahedron that neighbors with this edge as depicted in Figure 5.4.

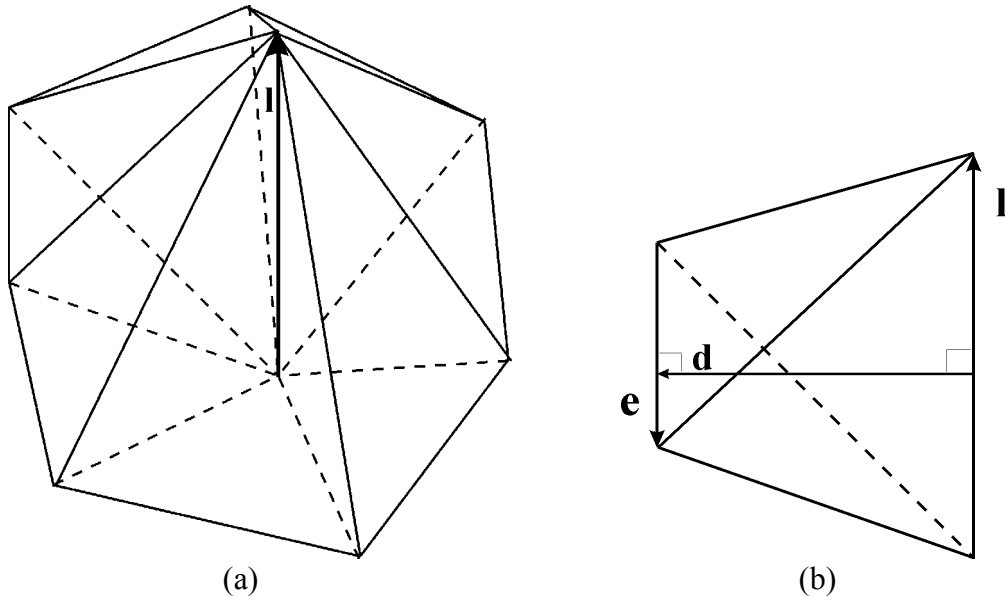


Figure 5.4: (a) An edge \mathbf{l} residing within a particular volume and all neighboring tetrahedra $\Delta_i (i=1,2,\dots,N)$, (b) the same edge \mathbf{l} showing the connectivity to one of the tetrahedra.

As seen in Figure 5.4(b), the edge \mathbf{l} can be related to the tetrahedron via vectors \mathbf{e} and \mathbf{d} . While vector \mathbf{e} is opposite to edge \mathbf{l} , indicating a counterclockwise rotation, and vector \mathbf{d} is the minimum distance from \mathbf{l} to \mathbf{e} . This convention permits the definition of a basis function $\mathbf{f}^V(\mathbf{r})$ within the tetrahedron as follows:

$$\mathbf{f}^V(\mathbf{r}) = \frac{\mathbf{e}}{3V}, \quad (5.11)$$

where V is the volume of the tetrahedron. The direction of $\mathbf{f}^V(\mathbf{r})$ is aligned with vector \mathbf{e} . This basis function is divergence-free, i.e. $\nabla \cdot \mathbf{f}^V(\mathbf{r}) = 0$. The total flux of this function through the faces that share the edge \mathbf{l} is unity. More generally, we define $\mathbf{f}_n^V(\mathbf{r})$ as follows:

$$\mathbf{f}_n^V(\mathbf{r}) = \begin{cases} \frac{\mathbf{e}_{n\Delta_1}}{3V_{n\Delta_1}}, & \text{if } \mathbf{r} \text{ is in } \Delta_1 \\ \dots & \dots \\ \frac{\mathbf{e}_{n\Delta_N}}{3V_{n\Delta_N}}, & \text{if } \mathbf{r} \text{ is in } \Delta_N. \end{cases} \quad (5.12)$$

To better elucidate the rotational property of the vector field, Figure 5.5 depicts a top-down view onto the elemental geometry shown in Figure 5.4(a). Here vector \mathbf{l} is directed out of the plane.

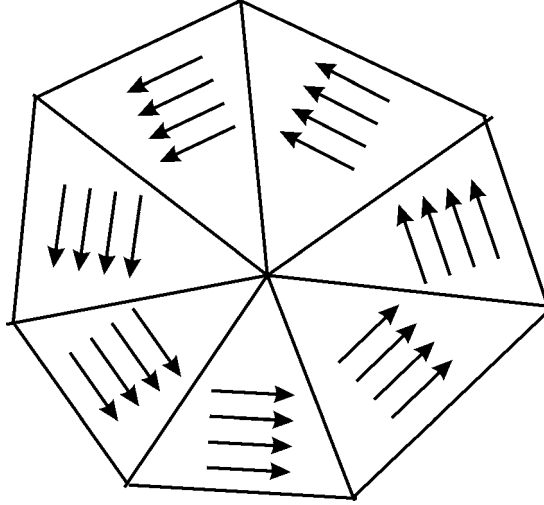


Figure 5.5: Top-down view of the solenoidal element which depict the divergence-free property of $\mathbf{f}^V(\mathbf{r})$.

Furthermore, index N is the number of tetrahedra neighboring edge \mathbf{l} , and $\Delta_1, \Delta_2, \dots, \Delta_N$ is the global numbering scheme for these tetrahedra. It is convenient to use these basis functions to describe a divergence-free vector \mathbf{C} in the 3D body via

$$\mathbf{C} = \sum_{n=1}^{N_e} C_n^V \mathbf{f}_n^V(\mathbf{r}), \quad (5.13)$$

where C_n^V is the net flux of vector \mathbf{C} through the faces included in the element; and N_e is the total number of elements throughout the discretization domain. The divergence-free vector \mathbf{C} is introduced from the following equations:

$$\text{div}(\mathbf{D}) = \rho \quad (5.14)$$

and

$$\text{div}(\mathbf{J}) = -j\omega\rho. \quad (5.15)$$

By multiplying (5.14) by $j\omega$ and adding (5.15) we obtain:

$$\text{div}(j\omega\mathbf{D} + \mathbf{J}) = 0. \quad (5.16)$$

We define vector \mathbf{C} as:

$$\mathbf{C} = j\omega\mathbf{D} + \mathbf{J}. \quad (5.17)$$

Obviously, (5.17) satisfies:

$$\text{div}(\mathbf{C}) = 0. \quad (5.18)$$

Number of rotational basis functions obviously equals the total number of edges in the 3D structure. Not all the function are, however, linearly independent. It can be shown that the number of linearly independent rotational basis functions equals total number of faces minus number of tetrahedra. A specially designed algorithm helps us to identify the linearly independent basis functions. In numerical simulations, only these functions are used.

5.3 Total Electric Field

The entire problem configuration consists of a loop coil, a perfectly conductive surface, a 3D conductive body, and an incident EM wave. The total electric field can be cast as consisting of the following contributions:

$$\begin{aligned} \mathbf{E}(\mathbf{r}) = & \mathbf{E}_{inc}(\mathbf{r}) - j\omega \frac{\mu_0}{4\pi} \int_{L'} \mathbf{J}^L(\mathbf{r}') \phi(\mathbf{r}, \mathbf{r}') dL' \\ & + \frac{1}{4\pi\epsilon_0 j\omega} \int_{S'} \nabla' \cdot \mathbf{J}^S(\mathbf{r}') \nabla \phi(\mathbf{r}, \mathbf{r}') dS' - j\omega \frac{\mu_0}{4\pi} \int_{S'} \mathbf{J}^S(\mathbf{r}') \phi(\mathbf{r}, \mathbf{r}') dS' \\ & + \frac{1}{4\pi\epsilon_0 j\omega} \int_{V'} \nabla' \cdot (\tilde{\mathbf{J}}^V(\mathbf{r}')) \nabla \phi(\mathbf{r}, \mathbf{r}') dV' - j\omega \frac{\mu_0}{4\pi} \int_{V'} \tilde{\mathbf{J}}^V(\mathbf{r}') \phi(\mathbf{r}, \mathbf{r}') dV'. \end{aligned} \quad (5.19)$$

Here, L is the line integration over the coil, S is the integration over perfectly conductive surface, and V is the integration over the 3D body. It is important to express vectors \mathbf{E} and $\tilde{\mathbf{J}}$ in terms of \mathbf{C} :

$$\mathbf{C} = j\omega\mathbf{D} + \mathbf{J} = j\omega\epsilon_r\epsilon_0\mathbf{E} + \sigma\mathbf{E}, \quad \text{or} \quad \Rightarrow \quad \mathbf{E} = \frac{\mathbf{C}}{j\omega\epsilon_r\epsilon_0 + \sigma} = k_1(\mathbf{r})\mathbf{C}, \quad (5.20)$$

and

$$\tilde{\mathbf{J}} = j\omega(\mathbf{D} - \varepsilon_0\mathbf{E}) + \mathbf{J} = \mathbf{C} - j\omega\varepsilon_0\mathbf{E} = \mathbf{C} \left(1 - \frac{j\omega\varepsilon_0}{j\omega\varepsilon_r\varepsilon_0 + \sigma} \right) = k_2(\mathbf{r})\mathbf{C}, \quad (5.21)$$

where the definitions of $k_1(\mathbf{r})$ and $k_2(\mathbf{r})$ can be inferred from Eq. (5.20) and (5.21).

Restating the electric field in terms of \mathbf{C} leads to the form:

$$\begin{aligned} -\mathbf{E}_{inc}(\mathbf{r}) &= \mathbf{E}_L(\mathbf{r}) + \mathbf{E}_S(\mathbf{r}) + \mathbf{E}_V(\mathbf{r}) - \mathbf{E}(\mathbf{r}) = \mathbf{E}_L(\mathbf{r}) + \mathbf{E}_S(\mathbf{r}) + \mathbf{E}_V(\mathbf{r}) - k_1(\mathbf{r})\mathbf{C} \\ &= -j\omega \frac{\mu_0}{4\pi} \int_{L'} \mathbf{J}^L(\mathbf{r}') \varphi(\mathbf{r}, \mathbf{r}') dL' \\ &+ \frac{1}{4\pi\varepsilon_0 j\omega} \int_{S'} \nabla' \cdot \mathbf{J}^S(\mathbf{r}') \nabla \varphi(\mathbf{r}, \mathbf{r}') dS' - j\omega \frac{\mu_0}{4\pi} \int_{S'} \mathbf{J}^S(\mathbf{r}') \varphi(\mathbf{r}, \mathbf{r}') dS' \\ &+ \frac{1}{4\pi\varepsilon_0 j\omega} \int_{V'} \nabla' \cdot (k_2(\mathbf{r}')\mathbf{C}^V(\mathbf{r}')) \nabla \varphi(\mathbf{r}, \mathbf{r}') dV' - j\omega \frac{\mu_0}{4\pi} \int_{V'} k_2(\mathbf{r}')\mathbf{C}^V(\mathbf{r}') \varphi(\mathbf{r}, \mathbf{r}') dV' - \mathbf{E}(\mathbf{r}). \end{aligned} \quad (5.22)$$

Here $\mathbf{E}_L(\mathbf{r})$, $\mathbf{E}_S(\mathbf{r})$, $\mathbf{E}_V(\mathbf{r})$ are contributions from the thin wire, perfectly conductive surface, and the 3D body. Expression (5.22) can be simplified as:

$$-\mathbf{E}_{inc}(\mathbf{r}) - \mathbf{E}_L(\mathbf{r}) = \mathbf{E}_S(\mathbf{r}) + \mathbf{E}_V(\mathbf{r}) - \mathbf{E}(\mathbf{r}) = \mathbf{E}_S(\mathbf{r}) + \mathbf{E}_V(\mathbf{r}) - k_1(\mathbf{r})\mathbf{C}. \quad (5.23)$$

$$\begin{aligned} -\mathbf{E}_{inc}(\mathbf{r}) - \mathbf{E}_L(\mathbf{r}) &= \\ &= \frac{1}{4\pi\varepsilon_0 j\omega} \int_{S'} \nabla' \cdot \mathbf{J}^S(\mathbf{r}') \nabla \varphi(\mathbf{r}, \mathbf{r}') dS' - j\omega \frac{\mu_0}{4\pi} \int_{S'} \mathbf{J}^S(\mathbf{r}') \varphi(\mathbf{r}, \mathbf{r}') dS' \\ &+ \frac{1}{4\pi\varepsilon_0 j\omega} \int_{V'} (\tilde{\nabla}' k_2(\mathbf{r}') \cdot \mathbf{C}^V(\mathbf{r}')) \nabla \varphi(\mathbf{r}, \mathbf{r}') dV' - j\omega \frac{\mu_0}{4\pi} \int_{V'} k_2(\mathbf{r}')\mathbf{C}^V(\mathbf{r}') \varphi(\mathbf{r}, \mathbf{r}') dV' - \mathbf{E}(\mathbf{r}), \end{aligned} \quad (5.24)$$

where advantage is taken of the fact that $\nabla \cdot \mathbf{C}(\mathbf{r}) = 0$.

5.4 Matrix Representation and Testing of the Formulation

Our goal is now to convert (5.24) into a linear matrix equation by using the aforementioned basis functions as testing functions. We intend to arrive at a matrix equation in the generic form

$$\begin{matrix} \mathbf{f}_m^S(\mathbf{r}) \\ \mathbf{f}_m^V(\mathbf{r}) \end{matrix} \begin{pmatrix} \overbrace{\mathbf{D}^{SS}} & \overbrace{\mathbf{D}^{SV}} \\ \hline \overbrace{\mathbf{D}^{VS}} & \overbrace{\mathbf{D}^{VV}} \end{pmatrix} \begin{pmatrix} \mathbf{I}^S \\ \mathbf{C}^V \end{pmatrix} = - \begin{pmatrix} \mathbf{D}^{S-Inc} \\ \mathbf{D}^{V-Inc} \end{pmatrix} - \begin{pmatrix} \mathbf{D}^{SL} \\ \mathbf{D}^{VL} \end{pmatrix} \begin{pmatrix} \mathbf{I}^L \end{pmatrix}$$

where the constituent terms will be defined further below. As will be seen, superscripts L, S, V in the vector terms stand for line, surface, and volume integral contributions, whereas double superscripts indicate “self-terms” (SS and VV), and “cross-terms” (SV, VS, SL, VL). Current vector \mathbf{I}^L is considered known. As a result, there is no need to test this equation for the electric field with the linear line functions $\mathbf{f}_m^L(\mathbf{r})$ as defined in (5.6).

5.4.1 Testing with surface current function $\mathbf{f}_m^S(\mathbf{r})$

Here we take the scalar product of \mathbf{E} with $\mathbf{f}_m^S(\mathbf{r})$ and carry out a surface integration, recognizing that for this case the $E_{\text{tang}} = 0$ boundary condition must be enforced. There are three terms, which can be integrated as follows:

$$\int_S \mathbf{f}_m^S(\mathbf{r}) \cdot \mathbf{E}_L(\mathbf{r}) dS = \sum_{\substack{n\text{-over} \\ \text{linear} \\ \text{elements}}} I_n^L \left\{ -j\omega \frac{\mu_0}{4\pi} \iint_{L L'} \mathbf{f}_m^S(\mathbf{r}) \cdot \mathbf{f}_n^L(\mathbf{r}') \phi(\mathbf{r}, \mathbf{r}') dL' dS \right\} = \sum_{\substack{n\text{-over} \\ \text{linear} \\ \text{elements}}} D_{mn}^{SL} I_n^L, \quad (5.25)$$

$$\begin{aligned} & \int_S \mathbf{f}_m^S(\mathbf{r}) \cdot \mathbf{E}_S(\mathbf{r}) dS = \\ & = \sum_{\substack{n\text{-over} \\ \text{surface} \\ \text{elements}}} I_n^S \left\{ \frac{1}{4\pi\epsilon_0 j\omega} \iint_{S S'} \nabla' \cdot \mathbf{f}_n^S(\mathbf{r}') (\mathbf{f}_m^S(\mathbf{r}) \cdot \nabla \phi(\mathbf{r}, \mathbf{r}')) dS' dS - j\omega \frac{\mu_0}{4\pi} \iint_{S S'} \mathbf{f}_m^S(\mathbf{r}) \cdot \mathbf{f}_n^S(\mathbf{r}') \phi(\mathbf{r}, \mathbf{r}') dS' dS \right\} \\ & = \sum_{\substack{n\text{-over} \\ \text{surface} \\ \text{elements}}} I_n^S \left\{ -\frac{1}{4\pi\epsilon_0 j\omega} \iint_{S S'} \nabla' \cdot \mathbf{f}_n^S(\mathbf{r}') \nabla \cdot \mathbf{f}_m^S(\mathbf{r}) \phi(\mathbf{r}, \mathbf{r}') dS' dS - j\omega \frac{\mu_0}{4\pi} \iint_{S S'} \mathbf{f}_m^S(\mathbf{r}) \cdot \mathbf{f}_n^S(\mathbf{r}') \phi(\mathbf{r}, \mathbf{r}') dS' dS \right\} \quad (5.26) \\ & = \sum_{\substack{n\text{-over} \\ \text{surface} \\ \text{elements}}} D_{mn}^{SS} I_n^S, \end{aligned}$$

$$\begin{aligned}
& \int_S \mathbf{f}_m^S(\mathbf{r}) \cdot \mathbf{E}_V(\mathbf{r}) dS = \\
& = \sum_{\substack{n\text{-over} \\ \text{volume} \\ \text{elements}}} C_n^V \left\{ \frac{1}{4\pi\epsilon_0 j\omega} \int \int_{S'} (\bar{\nabla}' k_2(\mathbf{r}') \cdot \mathbf{f}_n^V(\mathbf{r}')) (\mathbf{f}_m^S(\mathbf{r}) \cdot \nabla \varphi(\mathbf{r}, \mathbf{r}')) dV' dS - j\omega \frac{\mu_0}{4\pi} \int \int_{S'} \mathbf{f}_m^S(\mathbf{r}) \cdot \mathbf{f}_n^V(\mathbf{r}') k_2(\mathbf{r}') \varphi(\mathbf{r}, \mathbf{r}') dV' dS \right\} \\
& = \sum_{\substack{n\text{-over} \\ \text{volume} \\ \text{elements}}} C_n^V \left\{ -\frac{1}{4\pi\epsilon_0 j\omega} \int \int_{S'} (\bar{\nabla}' k_2(\mathbf{r}') \cdot \mathbf{f}_n^V(\mathbf{r}')) \nabla \cdot \mathbf{f}_m^S(\mathbf{r}) \varphi(\mathbf{r}, \mathbf{r}') dV' dS - j\omega \frac{\mu_0}{4\pi} \int \int_{S'} \mathbf{f}_m^S(\mathbf{r}) \cdot \mathbf{f}_n^V(\mathbf{r}') k_2(\mathbf{r}') \varphi(\mathbf{r}, \mathbf{r}') dV' dS \right\} \quad (5.27) \\
& = \sum_{\substack{n\text{-over} \\ \text{volume} \\ \text{elements}}} C_n^V \left\{ \frac{1}{4\pi\epsilon_0 j\omega} \int \int_{S'} k_2(\mathbf{r}') (\mathbf{f}_n^V(\mathbf{r}') \cdot \mathbf{n}_{\delta V'}) \nabla \cdot \mathbf{f}_m^S(\mathbf{r}) \varphi(\mathbf{r}, \mathbf{r}') d\delta V' dS - j\omega \frac{\mu_0}{4\pi} \int \int_{S'} \mathbf{f}_m^S(\mathbf{r}) \cdot \mathbf{f}_n^V(\mathbf{r}') k_2(\mathbf{r}') \varphi(\mathbf{r}, \mathbf{r}') dV' dS \right\} \\
& = \sum_{\substack{n\text{-over} \\ \text{volume} \\ \text{elements}}} D_{mn}^{SV} C_n^V .
\end{aligned}$$

5.4.2 Testing with volume function $\mathbf{f}_m^V(\mathbf{r})$

Here the scalar product of \mathbf{E}_L with $k_2(\mathbf{r})\mathbf{f}_m^V(\mathbf{r})$ is carried out as follows:

$$\begin{aligned}
\int_V k_2(\mathbf{r}) \mathbf{f}_m^V(\mathbf{r}) \cdot \mathbf{E}_L(\mathbf{r}) dV & = \sum_{\substack{n\text{-over} \\ \text{linear} \\ \text{elements}}} I_n^L \left\{ -j\omega \frac{\mu_0}{4\pi} \int \int_{V'} k_2(\mathbf{r}) \mathbf{f}_m^V(\mathbf{r}) \cdot \mathbf{f}_n^L(\mathbf{r}') \varphi(\mathbf{r}, \mathbf{r}') dL' dV \right\} \\
& = \sum_{\substack{n\text{-over} \\ \text{linear} \\ \text{elements}}} D_{mn}^{VL} I_n^L .
\end{aligned} \quad (5.28)$$

In a similar way we write down expressions for the integrals $\int_V k_2(\mathbf{r}) \mathbf{f}_m^V(\mathbf{r}) \cdot \mathbf{E}_S(\mathbf{r}) dV$ and

$$\int_V k_2(\mathbf{r}) \mathbf{f}_m^V(\mathbf{r}) \cdot \mathbf{E}_V(\mathbf{r}) dV :$$

$$\begin{aligned}
& \int_V k_2(\mathbf{r}) \mathbf{f}_m^V(\mathbf{r}) \cdot \mathbf{E}_S(\mathbf{r}) dV = \\
& = \sum_{\substack{n\text{-over} \\ \text{surface} \\ \text{elements}}} I_n^S \left\{ \frac{1}{4\pi\epsilon_0 j \omega} \int_{V'} \nabla' \cdot \mathbf{f}_n^S(\mathbf{r}') (k_2(\mathbf{r}) \mathbf{f}_m^V(\mathbf{r}) \cdot \nabla \varphi(\mathbf{r}, \mathbf{r}')) dS' dV - j\omega \frac{\mu_0}{4\pi} \int_{V'} \int_{V'} k_2(\mathbf{r}) \mathbf{f}_m^V(\mathbf{r}) \cdot \mathbf{f}_n^S(\mathbf{r}') \varphi(\mathbf{r}, \mathbf{r}') dS' dV \right\} \\
& = \sum_{\substack{n\text{-over} \\ \text{surface} \\ \text{elements}}} I_n^S \left\{ \frac{1}{4\pi\epsilon_0 j \omega} \int_{S'} \nabla' \cdot \mathbf{f}_n^S(\mathbf{r}') \int_{\delta V'} k_2(\mathbf{r}) (\mathbf{f}_m^V(\mathbf{r}) \cdot \mathbf{n}_{\delta V'}) \varphi(\mathbf{r}, \mathbf{r}') d\delta V dS' - \frac{1}{4\pi\epsilon_0 j \omega} \int_{V'} \nabla' \cdot \mathbf{f}_n^S(\mathbf{r}') \nabla \cdot (k_2(\mathbf{r}) \mathbf{f}_m^V(\mathbf{r})) \varphi(\mathbf{r}, \mathbf{r}') dS' dV \right. \\
& \quad \left. - j\omega \frac{\mu_0}{4\pi} \int_{V'} \int_{V'} k_2(\mathbf{r}) \mathbf{f}_m^V(\mathbf{r}) \cdot \mathbf{f}_n^S(\mathbf{r}') \varphi(\mathbf{r}, \mathbf{r}') dS' dV \right\} \tag{5.29}
\end{aligned}$$

$$\begin{aligned}
& = \sum_{\substack{n\text{-over} \\ \text{surface} \\ \text{elements}}} I_n^S \left\{ \frac{1}{4\pi\epsilon_0 j \omega} \int_{S'} \nabla' \cdot \mathbf{f}_n^S(\mathbf{r}') \int_{\delta V'} (k_2(\mathbf{r}) \mathbf{f}_m^V(\mathbf{r}) \cdot \mathbf{n}_{\delta V'}) \varphi(\mathbf{r}, \mathbf{r}') d\delta V dS' - j\omega \frac{\mu_0}{4\pi} \int_{V'} \int_{V'} k_2(\mathbf{r}) \mathbf{f}_m^V(\mathbf{r}) \cdot \mathbf{f}_n^S(\mathbf{r}') \varphi(\mathbf{r}, \mathbf{r}') dS' dV \right\} \\
& = \sum_{\substack{n\text{-over} \\ \text{surface} \\ \text{elements}}} D_{mn}^{VS} I_n^S, \\
& \int_V k_2(\mathbf{r}) \mathbf{f}_m^V(\mathbf{r}) \cdot \mathbf{E}_V(\mathbf{r}) dV - \int_V k_2(\mathbf{r}) \mathbf{f}_m^V(\mathbf{r}) \cdot \mathbf{E}(\mathbf{r}) dV \\
& = \sum_{\substack{n\text{-over} \\ \text{volume} \\ \text{elements}}} C_n^V \left\{ \frac{1}{4\pi\epsilon_0 j \omega} \int_{V'} (\nabla' k_2(\mathbf{r}') \cdot \mathbf{f}_n^V(\mathbf{r}')) (k_2(\mathbf{r}) \mathbf{f}_m^V(\mathbf{r}) \cdot \nabla \varphi(\mathbf{r}, \mathbf{r}')) dV' dV - j\omega \frac{\mu_0}{4\pi} \int_{V'} \int_{V'} \mathbf{f}_m^V(\mathbf{r}) \cdot \mathbf{f}_n^V(\mathbf{r}') k_2(\mathbf{r}) k_2(\mathbf{r}') \varphi(\mathbf{r}, \mathbf{r}') dV' dV \right. \\
& \quad \left. - \int_V k_1(\mathbf{r}) k_2(\mathbf{r}) (\mathbf{f}_m^V(\mathbf{r}) \cdot \mathbf{f}_n^V(\mathbf{r})) dV \right\} \\
& = \sum_{\substack{n\text{-over} \\ \text{volume} \\ \text{elements}}} C_n^V \left\{ \frac{1}{4\pi\epsilon_0 j \omega} \int_{V'} (\nabla' k_2(\mathbf{r}') \cdot \mathbf{f}_n^V(\mathbf{r}')) \int_{\delta V'} (k_2(\mathbf{r}) \mathbf{f}_m^V(\mathbf{r}) \cdot \mathbf{n}_{\delta V'}) \varphi(\mathbf{r}, \mathbf{r}') d\delta V dV' \right. \\
& \quad - \frac{1}{4\pi\epsilon_0 j \omega} \int_{V'} \int_{V'} (\nabla' k_2(\mathbf{r}') \cdot \mathbf{f}_n^V(\mathbf{r}')) \nabla \cdot (k_2(\mathbf{r}) \mathbf{f}_m^V(\mathbf{r})) \varphi(\mathbf{r}, \mathbf{r}') dV' dV \\
& \quad \left. - j\omega \frac{\mu_0}{4\pi} \int_{V'} \int_{V'} k_2(\mathbf{r}') k_2(\mathbf{r}) \mathbf{f}_m^V(\mathbf{r}) \cdot \mathbf{f}_n^V(\mathbf{r}') \varphi(\mathbf{r}, \mathbf{r}') dV' dV - \int_V k_1(\mathbf{r}) k_2(\mathbf{r}) (\mathbf{f}_m^V(\mathbf{r}) \cdot \mathbf{f}_n^V(\mathbf{r})) dV \right\} \tag{5.30} \\
& = \sum_{\substack{n\text{-over} \\ \text{volume} \\ \text{elements}}} C_n^V \left\{ \frac{1}{4\pi\epsilon_0 j \omega} \int_{V'} (\nabla' k_2(\mathbf{r}') \cdot \mathbf{f}_n^V(\mathbf{r}')) \int_{\delta V'} (k_2(\mathbf{r}) \mathbf{f}_m^V(\mathbf{r}) \cdot \mathbf{n}_{\delta V'}) \varphi(\mathbf{r}, \mathbf{r}') d\delta V dV' \right. \\
& \quad \left. - j\omega \frac{\mu_0}{4\pi} \int_{V'} \int_{V'} k_2(\mathbf{r}') k_2(\mathbf{r}) \mathbf{f}_m^V(\mathbf{r}) \cdot \mathbf{f}_n^V(\mathbf{r}') \varphi(\mathbf{r}, \mathbf{r}') dV' dV - \int_V k_1(\mathbf{r}) k_2(\mathbf{r}) (\mathbf{f}_m^V(\mathbf{r}) \cdot \mathbf{f}_n^V(\mathbf{r})) dV \right\} \\
& = \sum_{\substack{n\text{-over} \\ \text{volume} \\ \text{elements}}} C_n^V \left\{ - \frac{1}{4\pi\epsilon_0 j \omega} \int_{\delta V'} k_2(\mathbf{r}) k_2(\mathbf{r}') (\mathbf{f}_m^V(\mathbf{r}') \cdot \mathbf{n}_{\delta V'}) \int_{\delta V'} (\mathbf{f}_m^V(\mathbf{r}) \cdot \mathbf{n}_{\delta V'}) \varphi(\mathbf{r}, \mathbf{r}') d\delta V d\delta V' \right. \\
& \quad \left. - j\omega \frac{\mu_0}{4\pi} \int_{V'} \int_{V'} k_2(\mathbf{r}) k_2(\mathbf{r}') \mathbf{f}_m^V(\mathbf{r}) \cdot \mathbf{f}_n^V(\mathbf{r}') \varphi(\mathbf{r}, \mathbf{r}') dV' dV - \int_V k_2(\mathbf{r}) k_1(\mathbf{r}) (\mathbf{f}_m^V(\mathbf{r}) \cdot \mathbf{f}_n^V(\mathbf{r})) dV \right\} \\
& = \sum_{\substack{n\text{-over} \\ \text{volume} \\ \text{elements}}} D_{mn}^{VV} C_n^V.
\end{aligned}$$

5.5 Discretization

The system of equations can now be cast in the form

$$\begin{pmatrix} \mathbf{D}^{SS} & \mathbf{D}^{SV} \\ \mathbf{D}^{VS} & \mathbf{D}^{VV} \end{pmatrix} \cdot \begin{pmatrix} \mathbf{I}^S \\ \mathbf{C}^V \end{pmatrix} = - \begin{pmatrix} \mathbf{D}^{S-Inc} \\ \mathbf{D}^{V-Inc} \end{pmatrix} - \begin{pmatrix} \mathbf{D}^{SL} \\ \mathbf{D}^{VL} \end{pmatrix} \mathbf{I}^L, \quad (5.31)$$

where \mathbf{I}^S , \mathbf{C}^V are unknown vectors quantifies and sub-matrices \mathbf{D} are defined in (5.25) - (5.30). This system can be driven with current elements, a voltage source, an incident wave, or a combination of the three. In this formulation all linear elements have the same current. Defining

$$\mathbf{Z} = \begin{pmatrix} \mathbf{D}^{SS} & \mathbf{D}^{SV} \\ \mathbf{D}^{VS} & \mathbf{D}^{VV} \end{pmatrix} \quad \text{and} \quad \mathbf{b} = - \begin{pmatrix} \mathbf{D}^{S-Inc} \\ \mathbf{D}^{V-Inc} \end{pmatrix} - \begin{pmatrix} \mathbf{D}^{SL} \\ \mathbf{D}^{VL} \end{pmatrix} \mathbf{I}^L \quad (5.32)$$

one obtains

$$\mathbf{Z} \begin{pmatrix} \mathbf{I}^S \\ \mathbf{C}^V \end{pmatrix} = \mathbf{b}. \quad (5.33)$$

Solving these equations, the surface current \mathbf{I}^S can be determined over the perfectly conductive surface as well as the values \mathbf{C}^V in the volume domain. The numerical evaluation of the integral contributions is found to be

$$D_{mn}^{SL} = -j\omega \frac{\mu_0}{4\pi} \int \int_{S'L'} \mathbf{f}_m^S(\mathbf{r}) \cdot \mathbf{f}_n^L(\mathbf{r}') \varphi(\mathbf{r}, \mathbf{r}') dL' dS \approx -j\omega \frac{\mu_0}{4\pi} \frac{1}{2} \left(\frac{\boldsymbol{\rho}_m^{c+} \cdot \mathbf{l}_n}{r_{m^+n}} + \frac{\boldsymbol{\rho}_m^{c-} \cdot \mathbf{l}_n}{r_{m^-n}} \right). \quad (5.34)$$

Here, $r_{m^\pm n}$ are distances from left/right triangles of the surface element to the linear element. Furthermore, the D_{mn}^{SS} sub-matrix is

$$\begin{aligned}
D_{mn}^{SS} &= -\frac{1}{4\pi\epsilon_0 j\omega} \int_S \int_{S'} \nabla' \cdot \mathbf{f}_n^S(\mathbf{r}') \nabla \cdot \mathbf{f}_m^S(\mathbf{r}) \varphi(\mathbf{r}, \mathbf{r}') dS' dS \\
&\quad - j\omega \frac{\mu_0}{4\pi} \int_S \int_{S'} \mathbf{f}_m^S(\mathbf{r}) \cdot \mathbf{f}_n^S(\mathbf{r}') \varphi(\mathbf{r}, \mathbf{r}') dS' dS \\
&\approx -\frac{1}{4\pi\epsilon_0 j\omega} \left(\frac{1}{r_{m^+n^+}} - \frac{1}{r_{m^+n^-}} - \frac{1}{r_{m^-n^+}} + \frac{1}{r_{m^-n^-}} \right) \\
&\quad - j\omega \frac{\mu_0}{4\pi} \frac{1}{2 \cdot 2} \left(\frac{\mathbf{p}_m^{c^+} \cdot \mathbf{p}_n^{c^+}}{r_{m^+n^+}} + \frac{\mathbf{p}_m^{c^+} \cdot \mathbf{p}_n^{c^-}}{r_{m^+n^-}} + \frac{\mathbf{p}_m^{c^-} \cdot \mathbf{p}_n^{c^+}}{r_{m^-n^+}} + \frac{\mathbf{p}_m^{c^-} \cdot \mathbf{p}_n^{c^-}}{r_{m^-n^-}} \right).
\end{aligned} \tag{5.35}$$

Here, $r_{m^\pm n^\pm}$ are distances from left/right triangles of the m^{th} surface element to the left/right triangles of the n^{th} surface element. For the two-dimensional integration over the same triangle, (5.35) becomes singular since distances $r_{m^\pm n^\pm}$ are zero. However, following a procedure outline in [23], we can obtain closed-form expressions for the integrals containing these singularities. Sub-matrix D_{mn}^{SS} is given by

$$\begin{aligned}
D_{mn}^{SV} &= \frac{1}{4\pi\epsilon_0 j\omega} \int_S \int_{\delta V'} k_2(\mathbf{r}') [\mathbf{f}_n^V(\mathbf{r}') \cdot \mathbf{n}_{\delta V'}] \nabla \cdot \mathbf{f}_m^S(\mathbf{r}) \varphi(\mathbf{r}, \mathbf{r}') d\delta V' dS \\
&\quad - j\omega \frac{\mu_0}{4\pi} \int_S \int_{V'} \mathbf{f}_m^S(\mathbf{r}) \cdot \mathbf{f}_n^V(\mathbf{r}') k_2(\mathbf{r}') \varphi(\mathbf{r}, \mathbf{r}') dV' dS \\
&\approx \frac{1}{4\pi\epsilon_0 j\omega} \sum_{i=1}^{N_n} k_{2\Delta_i} \left[-\frac{1}{r_{m^+(n\Delta_i)^+}} + \frac{1}{r_{m^+(n\Delta_i)^-}} + \frac{1}{r_{m^-(n\Delta_i)^+}} - \frac{1}{r_{m^-(n\Delta_i)^-}} \right] \\
&\quad - j\omega \frac{\mu_0}{4\pi} \sum_{i=1}^{N_n} k_{2\Delta_n} \frac{1}{3} \cdot \frac{1}{2} \left(\frac{\mathbf{p}_m^{c^+} \cdot \mathbf{e}_{n\Delta_i}}{r_{m^+\Delta_i}} + \frac{\mathbf{p}_m^{c^-} \cdot \mathbf{e}_{n\Delta_i}}{r_{m^-\Delta_i}} \right).
\end{aligned} \tag{5.36}$$

Here, δV is the integration over the boundaries of the Δ_i^{th} tetrahedron, $r_{m^\pm(n\Delta_i)^\pm}$ are distances from left/right triangles of the m^{th} surface element to the source/sink faces associated with the n^{th} volume element and the Δ_i^{th} tetrahedron, respectively. Also, $r_{m^\pm n}$ are distances from left/right triangles of the m^{th} surface element to the center point of the Δ_i^{th} tetrahedron. In addition,

$$D_m^{S-inc} = \int_S \mathbf{f}_m^S(\mathbf{r}) \cdot \mathbf{E}_{inc}(\mathbf{r}) dS \approx \frac{\mathbf{p}^{c^+} \cdot \mathbf{E}_{inc}^{c^+}}{2} + \frac{\mathbf{p}^{c^-} \cdot \mathbf{E}_{inc}^{c^-}}{2} \tag{5.37}$$

and

$$D_{mn}^{VL} = -j\omega \frac{\mu_0}{4\pi} \int_V \int_{V'} k_2(\mathbf{r}) \mathbf{f}_m^V(\mathbf{r}) \cdot \mathbf{f}_n^L(\mathbf{r}') \varphi(\mathbf{r}, \mathbf{r}') dL' dV \approx -j\omega \frac{\mu_0}{4\pi} \sum_{i=1}^{N_m} \frac{1}{3} \cdot k_{2\Delta_i} \frac{\mathbf{e}_{m\Delta_i} \cdot \mathbf{l}_n}{r_{\Delta_i n}}. \quad (5.38)$$

Here, $r_{\Delta_i n}$ are distances from the Δ_i^{th} tetrahedron to the n^{th} linear current element.

Moreover,

$$\begin{aligned} D_{mn}^{VS} &= \frac{1}{4\pi\epsilon_0 j\omega} \int_{S'} \nabla' \cdot \mathbf{f}_n^S(\mathbf{r}') \int_{\delta V} [k_2(\mathbf{r}) \mathbf{f}_m^V(\mathbf{r}) \cdot \mathbf{n}_{\delta V}] \varphi(\mathbf{r}, \mathbf{r}') d\delta V dS' \\ &\quad - j\omega \frac{\mu_0}{4\pi} \int_V \int_{S'} k_2(\mathbf{r}) \mathbf{f}_m^V(\mathbf{r}) \cdot \mathbf{f}_n^S(\mathbf{r}') \varphi(\mathbf{r}, \mathbf{r}') dS' dV \\ &\approx \frac{1}{4\pi\epsilon_0 j\omega} \sum_{i=1}^{N_m} k_{2\Delta_i} \left[-\frac{1}{r_{(m\Delta_i)^+ n^+}} + \frac{1}{r_{(m\Delta_i)^+ n^-}} + \frac{1}{r_{(m\Delta_i)^- n^+}} - \frac{1}{r_{(m\Delta_i)^- n^-}} \right] \\ &\quad - j\omega \frac{\mu_0}{4\pi} \sum_{i=1}^{N_m} \frac{1}{3} \cdot \frac{1}{2} k_{2\Delta_i} \left(\frac{\mathbf{p}^{c+} \cdot \mathbf{e}_{m\Delta_i}}{r_{\Delta_i n^+}} + \frac{\mathbf{p}^{c-} \cdot \mathbf{e}_{m\Delta_i}}{r_{\Delta_i n^-}} \right). \end{aligned} \quad (5.39)$$

In (5.39) distances $r_{(m\Delta_i)^\pm n^\pm}$ are lengths from source/sink faces associated with the m^{th} volume element and the Δ_i^{th} tetrahedron to the left/right triangles of the n^{th} surface element. Moreover, $r_{\Delta_i n^\pm}$ are distances from the center of the Δ_i^{th} tetrahedron to the left/right triangles of the n^{th} surface element. Finally,

$$\begin{aligned} D_{mn}^{VV} &= -\frac{1}{4\pi\epsilon_0 j\omega} \int_{V'} k_2(\mathbf{r}') [\mathbf{f}_n^V(\mathbf{r}') \cdot \mathbf{n}_{\delta V'}] \int_{\delta V} k_2(\mathbf{r}) [\mathbf{f}_m^V(\mathbf{r}) \cdot \mathbf{n}_{\delta V}] \varphi(\mathbf{r}, \mathbf{r}') d\delta V d\delta V' \\ &\quad - j\omega \frac{\mu_0}{4\pi} \int_V \int_{V'} k_2(\mathbf{r}') k_2(\mathbf{r}) \mathbf{f}_m^V(\mathbf{r}) \cdot \mathbf{f}_n^V(\mathbf{r}') \varphi(\mathbf{r}, \mathbf{r}') dV' dV - \int_V k_1(\mathbf{r}) k_2(\mathbf{r}) [\mathbf{f}_m^V(\mathbf{r}) \cdot \mathbf{f}_n^V(\mathbf{r})] dV \\ &\approx -\frac{1}{4\pi\epsilon_0 j\omega} \sum_{i=1}^{N_m} \sum_{j=1}^{N_n} k_{2\Delta_i} k_{2\Delta_j} \left[\frac{1}{r_{(m\Delta_i)^+ (n\Delta_j)^+}} - \frac{1}{r_{(m\Delta_i)^+ (n\Delta_j)^-}} - \frac{1}{r_{(m\Delta_i)^- (n\Delta_j)^+}} + \frac{1}{r_{(m\Delta_i)^- (n\Delta_j)^-}} \right] \\ &\quad - j\omega \frac{\mu_0}{4\pi} \sum_{i=1}^{N_m} \sum_{j=1}^{N_n} k_{2\Delta_i} k_{2\Delta_j} \frac{1}{3} \cdot \frac{1}{3} \cdot \frac{\mathbf{e}_{m\Delta_i} \cdot \mathbf{e}_{n\Delta_j}}{r_{\Delta_i \Delta_j}} \\ &\quad - \sum_{i=1}^{N_m} \sum_{j=1}^{N_n} \delta(\Delta_i = \Delta_j) k_{1\Delta_j} k_{2\Delta_j} \frac{1}{3V_{\Delta_i}} \cdot \frac{1}{3V_{\Delta_j}} \cdot (\mathbf{e}_{m\Delta_i} \cdot \mathbf{e}_{n\Delta_j}) V_{\Delta_i}. \end{aligned} \quad (5.40)$$

In (5.40) $r_{(m\Delta_i)^\pm(n\Delta_j)^\pm}$ are distances from the source/sink faces associated with the m^{th} volume element and the Δ_i^{th} tetrahedron to the source/sink faces associated with the n^{th} volume element and the Δ_j^{th} tetrahedron. Moreover, $r_{\Delta_i\Delta_j}$ are distances from the Δ_i^{th} tetrahedron to the Δ_j^{th} tetrahedron. Again, we face the problem of two-dimensional integration over the same tetrahedron or over the same face. The program implementation is such that if no analytic expressions for the double volume integral exist, they are evaluated numerically. This can be efficiently done by breaking the tetrahedra into smaller ones and performing the summation. Self-integrals over faces were calculated using expressions developed in [23]. Volume-volume self-integrals are evaluated numerically by subdividing each tetrahedron into smaller ones. Testing the incident field with the volume basis function yields

$$D_m^{V-Inc} = \int_V k_2(\mathbf{r}) \mathbf{f}_m^V(\mathbf{r}) \cdot \mathbf{E}_{inc}(\mathbf{r}) dV \approx \sum_{i=1}^{N_m} k_{2\Delta_i} \frac{(\mathbf{e}_{m\Delta_i} \cdot \mathbf{E}_{inc})}{3}. \quad (5.41)$$

5.6 Validation of the Formulation

To test the presented method, we compared it with the scattering problem of an incident plane EM wave on a dielectric sphere. This problem was fundamentally solved by Mie [24]-[25] by using separation of variables (see Appendix A). For our simulations we consider a sphere containing 887 nodes and 4013 tetrahedra. This results in 5285 edges and 4399 unknowns. For our numerical analysis we choose the following parameters: radius of the sphere $a = 0.02$ m, frequency $f = 200$ MHz, relative dielectric constant

$\epsilon_r = 2$, and conductivity $\sigma = 0.0\text{S/m}$. For the plane wave traveling in the positive z -direction it is assumed that electric field is in x -direction and $E_0 = 1.0\text{V/m}$.

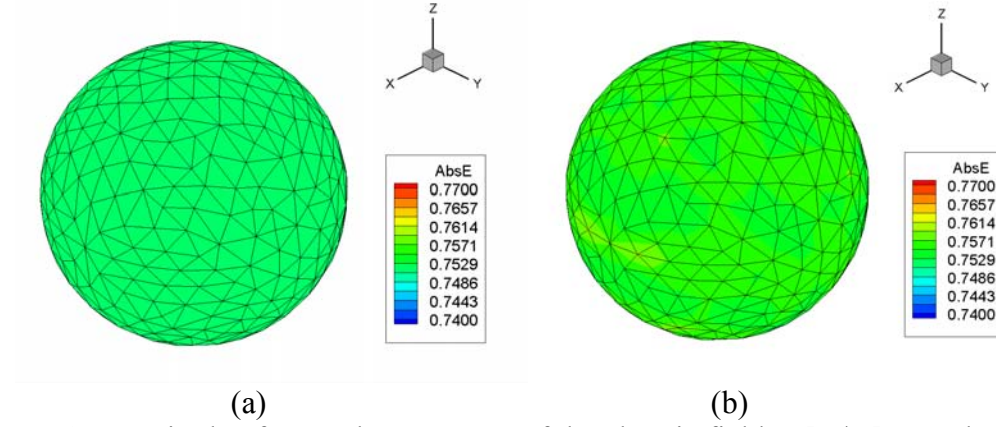


Figure 5.6: Magnitude of normal component of the electric field \mathbf{E} [V/m] over the surface of the sphere ($f = 200\text{MHz}$, $\epsilon_r = 2$, $\sigma = 0.0\text{S/m}$). (a) exact Mie series solution, and (b) MoM prediction.

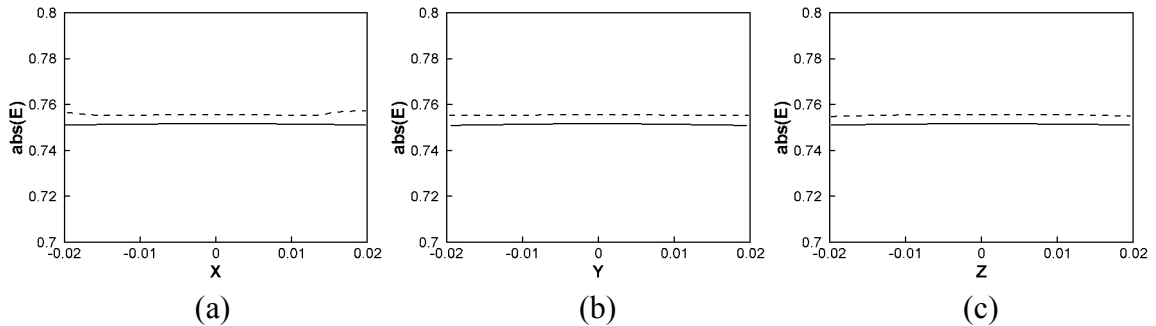
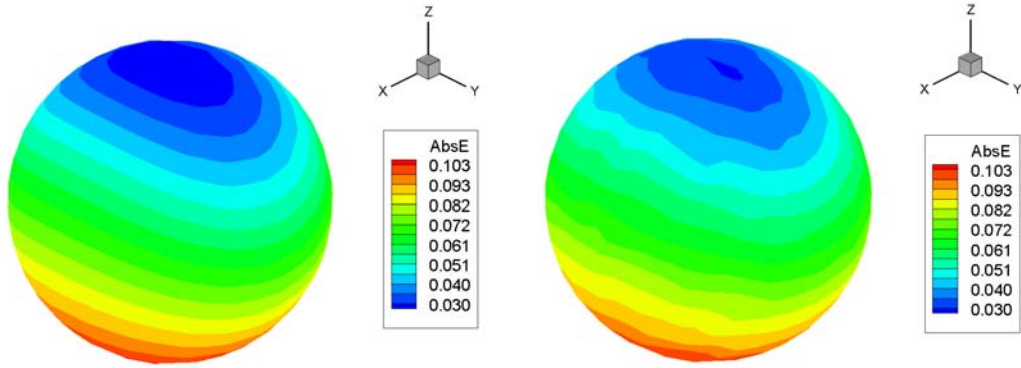


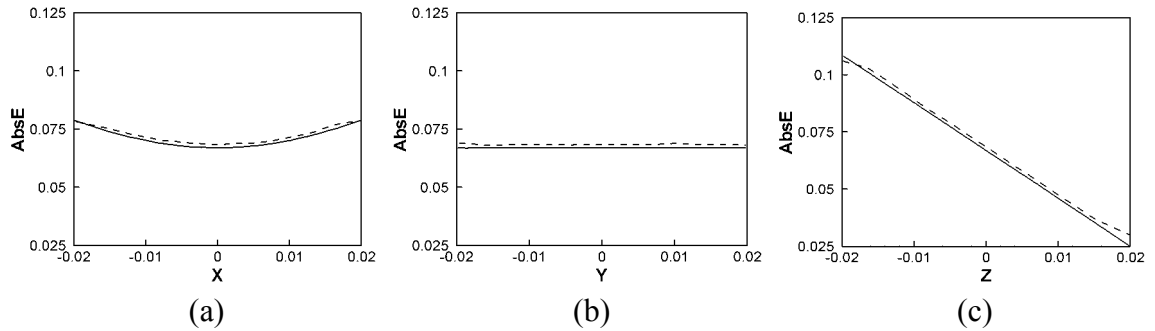
Figure 5.7: Magnitude of the electric field \mathbf{E} [V/m] on the surface of the sphere ($f = 200\text{MHz}$, $\epsilon_r = 2$, and $\sigma = 0.0\text{S/m}$). Comparison of exact (solid line) with MoM solutions (dashed line) along the a) x , b) y , and c) z – axes, respectively. All spatial dimensions are in [m].

As depicted in Figure 5.6(a), we observe that the absolute value of \mathbf{E} is approximately 0.75V/m . Discretization and numerical errors are responsible for small deviations of the MoM approach from the analytical series solution. The numerical solution is well behaved and provides us with the values of electric field \mathbf{E} that are close to the exact solution.

We next consider the case when we have a non-zero conductance. All parameters remain the same, except that the conductivity is now $\sigma = 0.5\text{S/m}$. Figures 5.8 and 5.9 depict the corresponding electric field over the sphere.



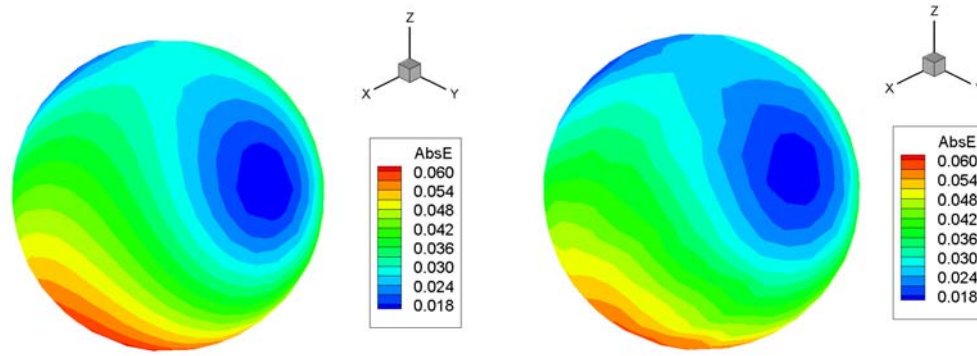
(a) (b)
Figure 5.8: Magnitude of the electric field \mathbf{E} [V/m] on the surface of a sphere ($f = 200\text{MHz}$, $\epsilon_r = 2$, $\sigma = 0.5\text{S/m}$). (a) exact Mie solution, (b) MoM prediction.



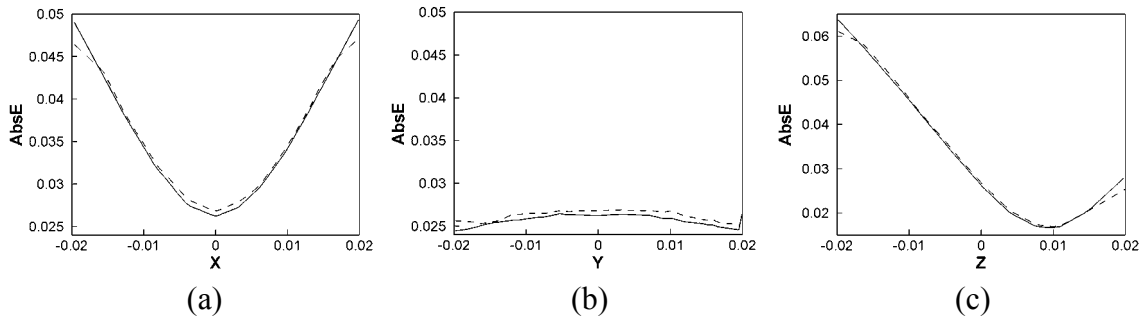
(a) (b) (c)
Figure 5.9: Magnitude of the electric field \mathbf{E} [V/m] on the surface of a sphere ($f = 200\text{MHz}$, $\epsilon_r = 2$, $\sigma = 0.5\text{S/m}$). Comparison of the exact Mie series solution (solid line) with MoM prediction (dashed line) along the a) x -, b) y -, and c) z - axes. All spatial dimensions are in [m].

It is seen that in the exact series solution the electric field of the plane wave attenuates when propagating inside the sphere (in positive z -direction). Clearly, MoM is able to describe the attenuation effect accurately.

Next we consider a similar simulation with higher values of ε and σ . In particular, $\varepsilon_r = 80$, $\sigma = 1.0$ S/m. Biological bodies such as brain tissue have similar values of the electric permittivity and conductance.



(a) (b)
 Figure 5.10: Magnitude of the electric field \mathbf{E} [V/m] on the surface of a sphere ($f = 200$ MHz, $\varepsilon_r = 80$, $\sigma = 1.0$ S/m). (a) exact Mie solution, (b) MoM prediction.



(a) (b) (c)
 Figure 5.11: Magnitude of the electric field \mathbf{E} [V/m] on the surface of a sphere ($f = 200$ MHz, $\varepsilon_r = 80$, $\sigma = 1.0$ S/m). Comparison of the exact Mie series solution (solid line) with MoM prediction (dashed line) along the a) x -, b) y -, and c) z - axes. All spatial dimensions are in [m].

Again we notice good agreement between the exact Mie solution and the MoM solution. As we observe, the electric field inside the body is attenuated rather significantly: its maximum is about 6% of the incident electric field.

These simulations generally demonstrate a good performance of our MoM formulation. Approximately 309MB of double precision memory are necessary to perform these three simulations. As soon as the matrix is symmetric, only 154MB of memory is required. Solutions are typically computed within 25 minutes on a PC Pentium 4 computer with 1.5 GHz processor speed.

5.7 Additional Examples

(a) Gradient Coil inside the Magnet Bore

This arrangement consists of a six-loop G_y gradient coil of Figure 3.20 and a metallic cylinder of 10 cm in radius (both systems are seen in Figure 5.12). The cylinder mesh has 544 nodes and 1020 triangle patches.

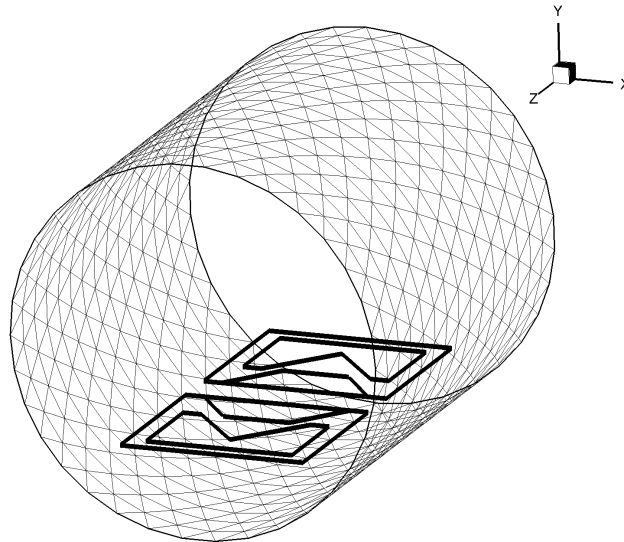


Figure 5.12: Gradient coil of Figure 3.20 inside a metallic cylinder.

We apply a current of 1A to the gradient coil at a frequency of 200 MHz. The high frequency current induces eddy currents on the surface of the metallic cylinder. The current distribution on the cylinder is shown in Figure 5.13.

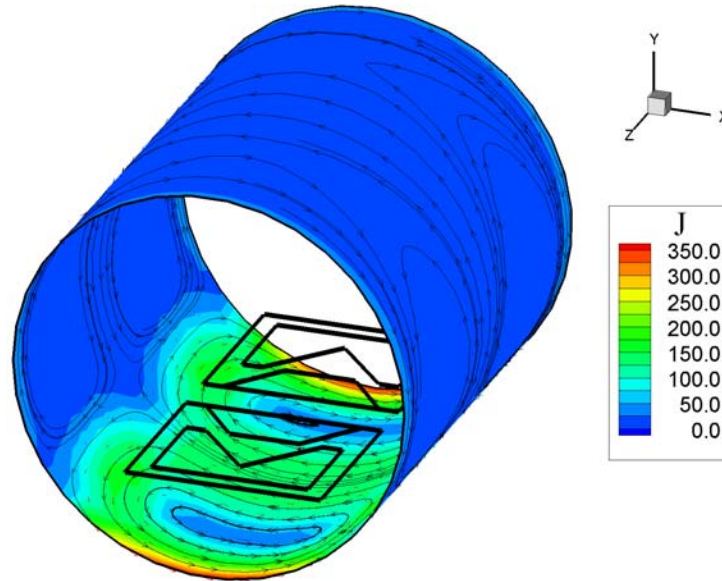


Figure 5.13: Distribution of surface current density \mathbf{J} [A/m] induced in the magnet bore.

In this figure, a color code represents the magnitude of the current induced on the cylinder wall. The direction of current flow is denoted by current streamlines. We observe that the induced currents approximately follow the same pattern as the current in the gradient coil.

(b) Gradient Coil and a Load inside the Magnet Bore

Here, we have a gradient coil and a biological load inside the magnet bore (see Figure 5.14). As in the previous example, the cylinder mesh has 544 nodes and 1020 triangle patches. Load is a dielectric sphere with $R = 2\text{ cm}$, $\epsilon_r = 2$, $\sigma = 0\text{ S/m}$. The mesh for the sphere has 106 nodes and 302 tetrahedra.

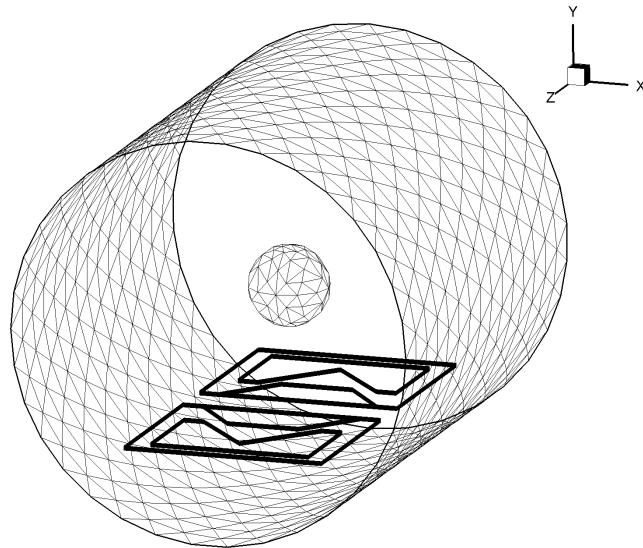


Figure 5.14: Gradient coil and a biological load inside the metallic cylinder.

Again, we execute our simulation at a frequency of 200 MHz. The gradient coil excites currents in the magnetic bore and polarization currents in the dielectric sphere as seen in Figure 5.15.

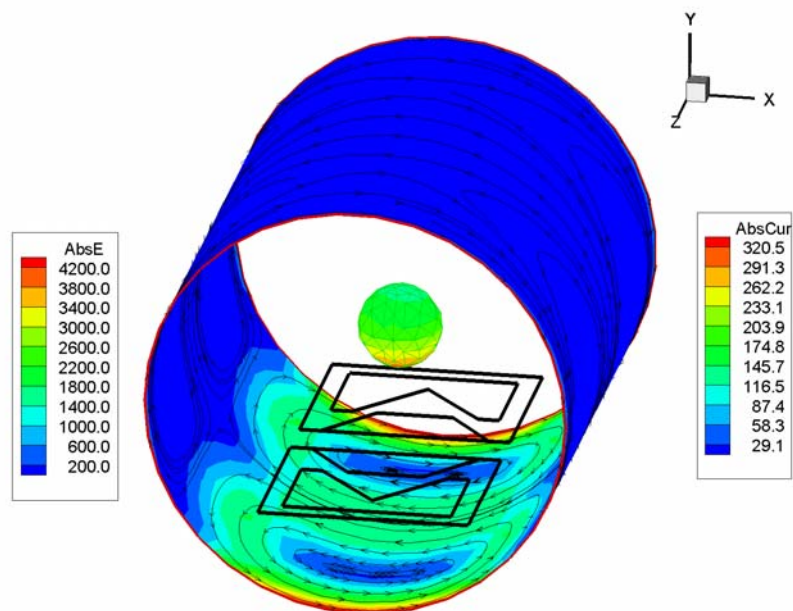


Figure 5.15: Surface current density \mathbf{J} [A/m] induced in the metallic cylinder and distribution of the electric field \mathbf{E} [V/m] on the sphere.

There are no conductance currents induced in the sphere because $\sigma = 0.0$ S/m. Polarization currents (as well as electric field) are mostly flowing back and forth along the x -axis. This can be easily explained based on Maxwell's equations. The magnetic field from the G_y gradient coil is mostly directed along the z -axis and it has a gradient along the y -axis. Curl of the magnetic field is, therefore, directed along the x -axis. According to $\nabla \times \mathbf{H} = \sigma \mathbf{E} + j\omega \epsilon \mathbf{E}$, the electric field is collinear to the curl of magnetic field. Therefore, \mathbf{E} is directed along the x -axis (see Figure 5.16).

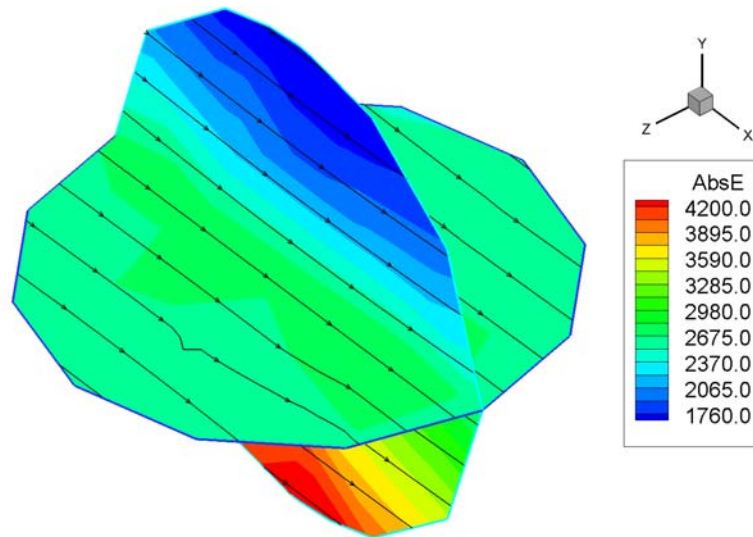


Figure 5.16: Electric field \mathbf{E} [V/m] distribution inside the sphere.

We also observe that we obtain a higher current in the lower part of the load. This makes sense, as this part is closer to the gradient coil.

(c) TEM resonator

In MRI, TEM resonators are used to provide pulses of high frequency magnetic fields. A TEM resonator [27] consists of multiple copper strips and an outer copper shield. In this example the strips have a length of 0.1524 m and a width of 0.00635 m. The shield has a

radius of 0.0527 m and height of 0.1524 m. The mesh for the TEM resonator is shown in Figure 5.17. This mesh has 4836 nodes and 680 triangles, which results in 10560 unknowns.

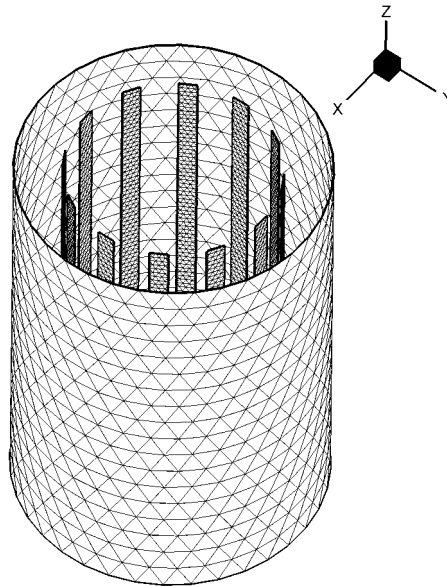


Figure 5.17: Mesh of TEM resonator.

Furthermore, each strip is connected to the shield by two lumped capacitors. There are, therefore, twenty-four capacitors in the resonator. A voltage source of 1 V was applied in series with one of the capacitors to act as the excitation element. Figure 5.18 demonstrates how to introduce lumped elements and a voltage feed into the system of linear equations for the MoM.

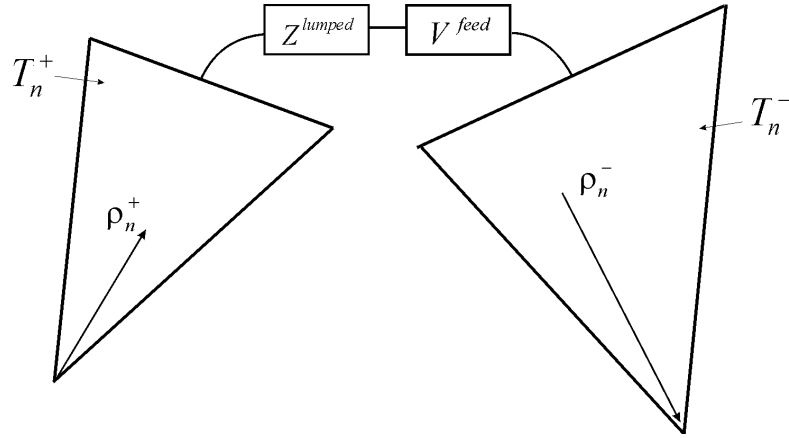


Figure 5.18: Introducing lumped elements into the MoM formulation.

Triangles T_n^+ and T_n^- represent the left and right triangles of the n^{th} surface current element. As it follows from Eq. (5.26), the coefficient D_{nn}^{SS} represent an impedance of the m^{th} element with a negative sign. Therefore, in order to take into account the lumped impedance Z^{lumped} , we have to subtract Z^{lumped} from the value of D_{nn}^{SS} . Furthermore, to introduce a feed voltage V^{feed} into the system, we have to subtract V^{feed} from the value of right-hand side vector b_n .

The resonator is tuned to 200 MHz. Simulations were performed to find the resonant value of the capacitors: $C = 10.59$ pF. Each simulation involves solving a 10560×10560 matrix. Filling in the matrix and solving it takes about 20 minutes on a 1.5 GHz Pentium 4 computer. The current distribution for the resonance is shown in Figure 5.19.

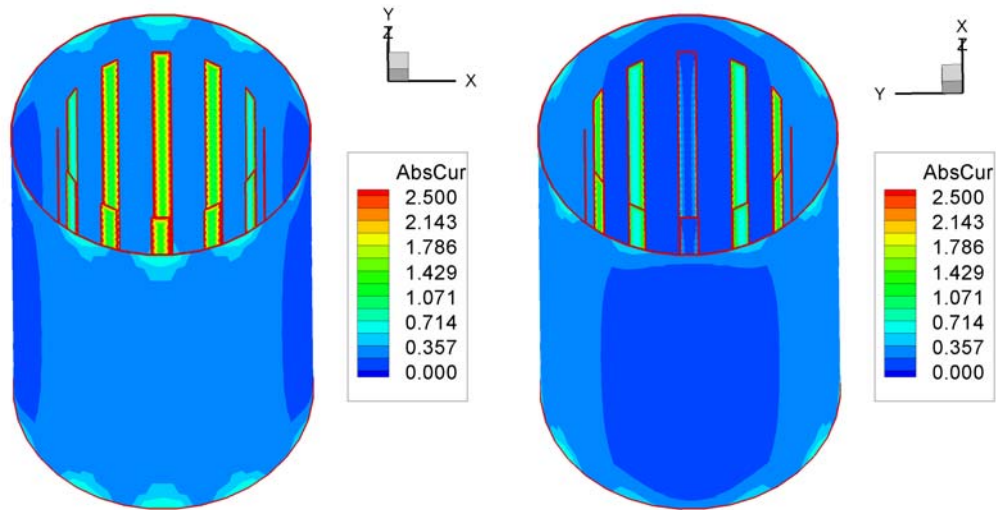


Figure 5.19: Surface current density \mathbf{J} [A/m] induced in the TEM resonator.

We then determine the magnetic field inside the resonator. Figure 5.20 shows the magnetic field in the xy -plane in the middle of the TEM resonator. It is gratifying to observe that the magnetic field is highly uniform in the center of the resonator.

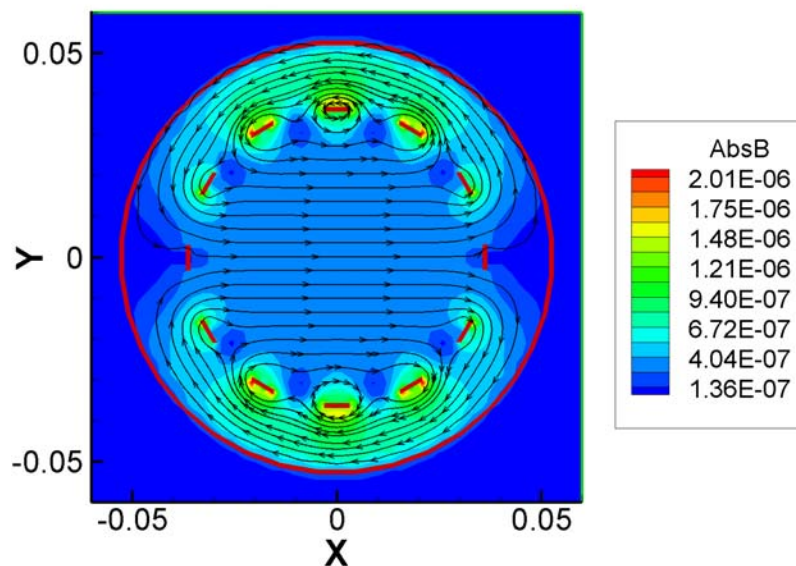


Figure 5.20: Absolute value and streamlines of the magnetic field \mathbf{B} [T] at a cross-section inside the volume coil. All spatial dimensions are given in [m].

5.8 Effect of Gradient Coils on a Biological Insert

We can now place a biological insert in the ROI for the gradient coil. The insert is a sphere having a radius of 2 cm, $\epsilon_r = 80$ and $\sigma = 1 \text{ S/m}$. These values of ϵ_r and σ are typical for animal brain tissue. For our simulations, we use a frequency of $f = 10 \text{ kHz}$, which is a typical operating frequency for gradient coils. We investigate the G_x gradient coil first. The electric field arising in the biological insert is shown in Figure 5.21. The maximum value of the electric field in the body is found to be 0.0158 V/m .

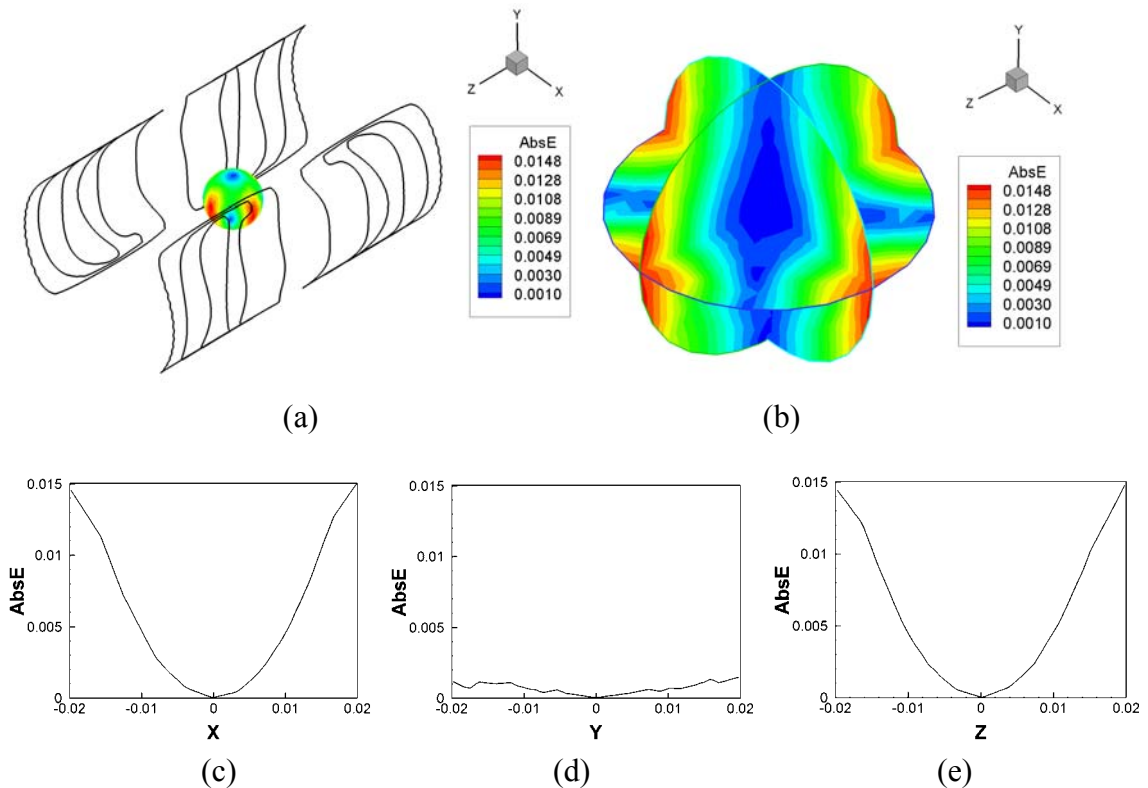


Figure 5.21: Electric field \mathbf{E} [V/m] created by the G_x gradient coil: (a) biological body inside the coil, (b) three cross-sections of the body, (c) electric field along the x -axis, (d) electric field along the y -axis, (e) electric field along the z -axis. All dimensions spatial are given in [m].

The electric field created in the body by the G_y gradient coil is shown in Figure 5.22.

The maximum value of the electric field in the body is 0.0496 V/m, and it is significantly higher than for the G_y gradient coil.

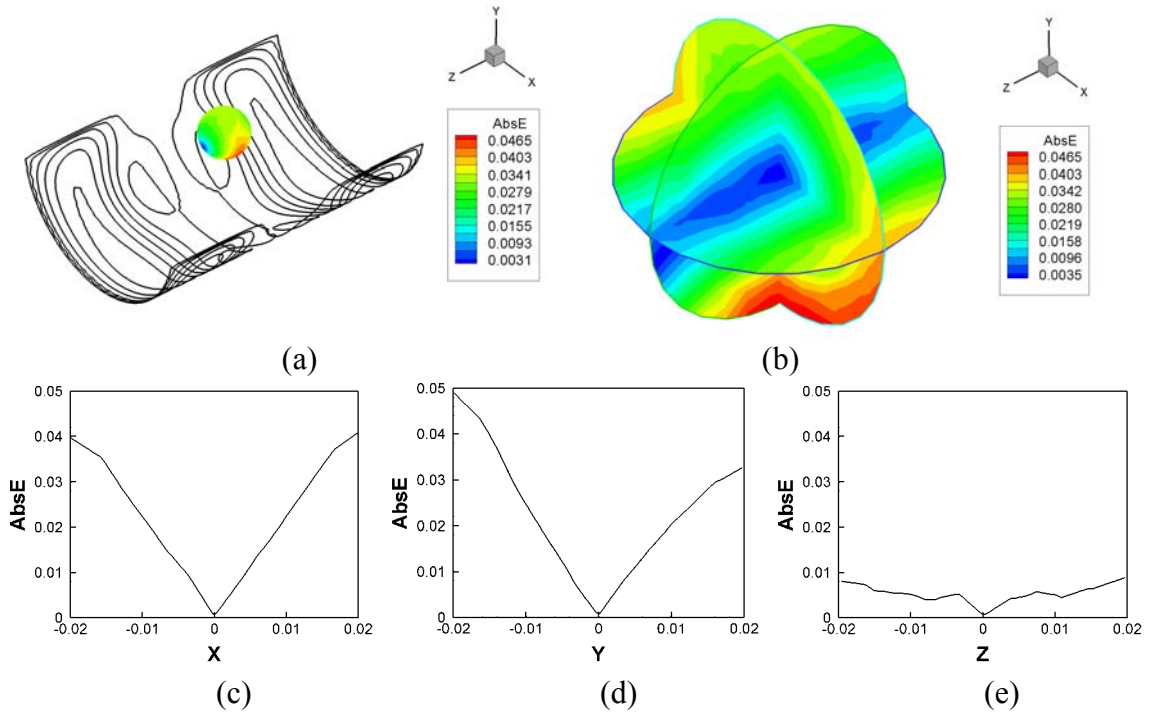


Figure 5.22: Electric field \mathbf{E} [V/m] created by the G_y gradient coil: (a) biological body inside the coil, (b) three cross-sections of the body, (c) electric field along the x -axis, (d) electric field along the y -axis, (e) electric field along the z -axis. All dimensions spatial are given in [m].

Figure 5.23 demonstrates the body inside the G_z gradient coil. As soon as the loops of this coil are placed far from the body, the maximum electric field, 0.0059 V/m, is relatively strong.

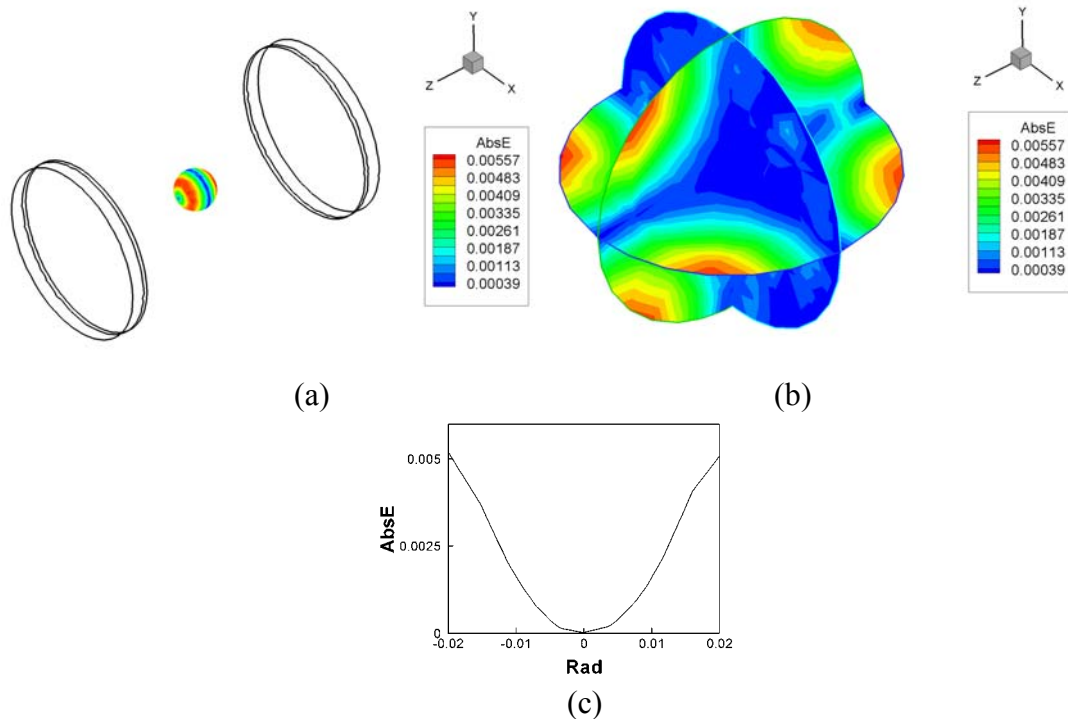


Figure 5.23: Electric field \mathbf{E} [V/m] created by the G_z gradient coil: (a) biological body inside the coil, (b) three cross-sections of the body, (c) electric field along the line passing through the center of the sphere and directed as along the (1,1,1) vector. All dimensions spatial are given in [m].

5.9 Chapter Summary

In this work we have shown that solenoidal basis functions can be successfully used to approximate the value of a new vector \mathbf{C} , which is a linear combination of the displacement and current density vectors. This special vector has the desirable property of being divergence-free, even if material properties in the solution domain are spatially dependent. Based on this new vector quantity a MoM approach is formulated and implemented. The resulting system of linear equations for the unknown current values can efficiently be computed for both the conductive surface and the edges associated with the 3D volumetric mesh.

An initial comparison with the exact Mie solution for an incident plane wave shows good agreement with the numerical solution. However, more detailed simulations with complex geometries are required to investigate the accuracy and computational efficiency of this new formulation. In addition, we tested the formulation with two examples involving a gradient coil inside a metallic cylinder (magnet bore) with and without a biological load. It is seen that high-frequency current oscillations in the gradient coil cause currents in the magnet bore and currents (polarization currents and/or conductance currents) in the biological load. Furthermore, the effect of the three designed and manufactured gradient coils on biological bodies is studied.

Chapter 6

Conclusions and Recommendations

6.1 Summary and Conclusions

In this dissertation we embarked on developing a new computational approach to design and optimize gradient coils for MRI. Specific accomplishments of the research include:

1. A static least-squares method is devised to design flat (surface) gradient coils. The formulation is based on prescribing the magnetic field a particular region of interest. The approach limits its applicability to low numbers of elementary current loops. Two G_y gradient coils (5×4 and 6×4 loop configurations) were designed and their performance was compared to that of a G_y surface gradient coil reported in the literature. It was shown that these coils generally provide better gradient uniformity, although the gradient strengths tend to be smaller. As a result, a fundamental strength-uniformity trade-off has to be made.

2. In an attempt to improve upon the least-squares method, we employed a “trial-and-error” approach to design a so-called six-loop G_y gradient coil. This coil was

constructed and its performance was tested in an MRI 4.7T system. Images obtained with a phantom and a marmoset brain compare well with a commercial gradient coil.

3. A novel stream function methodology is then formulated with the intent to generalize the current loop concept. The surface current is approximated using numerical rotational current elements. The current elements are obtained from the triangular mesh generated with a mesh generator. The formulation is based on the minimization of a cost function that comprises terms involving gradient uniformity, magnetic energy, shielding, and zero-momentum constraints. The simulations yield important coil characteristics such as resistance, inductance and gradient strength. As examples, several gradient coils were designed: a two-plate curved (crescent) G_x gradient coil; a flat G_y gradient coil with holes; a set of flat rectangular coils (G_x coil, G_y coil, G_z unbalanced coil, and G_z balanced coil); and a two-plate curved (crescent) G_x shielded gradient coil. It was shown that adjusting parameters for the magnetic energy and shielding enable an elaborate trade-off investigation between gradient uniformity, inductance, and gradient strength. In case of flat rectangular coils, the effect of the adjustment parameter for the magnetic energy term and its impact on the coil layout can be studied.

4. To ease the interaction with the program, a Graphic User Interface was developed. A software package called “Gradient Coil Designer” was written in Visual C++. All necessary components such as simple mesh generation, geometry file generation, matrix solver, postprocessing, magnetic field calculation are parts of this package as libraries. The results of the simulations can be saved to a project file and loaded from it. However, the GUI in its current version does not include a shielding option.

Finally, three gradient coils (comprising a gradient set) were designed and manufactured around an existing microstrip RF coil. The gradient coils were fitted inside a 4.7T MRI scanner and tested. Images of a phantom and of a rat brain were obtained. The performance of the gradient set, even at a reduced current strength, can be regarded a success: the observed distortions was found to be in agreement with the numerical predictions.

In an effort to quantify the dynamic interaction with the magnet bore and the RF coil, a novel Method of Moment formulation is finally developed. It includes a system consisting of a line current source (only for excitation), a highly conductive surface, and a 3D biological body characterized by values of electric permittivity and conductance. In addition, as excitation either a voltage source applied to the conductive surface or an incident electromagnetic wave can be employed. The current for the conductive surface is approximated by using RWG current elements, and the electric field in the 3D body is approximated by edge-based rotational basis functions. The formulation was tested with a so-called Mie series solution, which is an analytical solution of Maxwell's equations for the problem of an electromagnetic wave illuminating a uniform, dielectric sphere. Additional problems solved by this MoM formulation include: a gradient coil residing in the magnet bore, a gradient coil with a biological load inside the magnet bore, and a biological load inside the G_x , G_y and G_z gradient coils.

In summary, this research developed a new design, and a way to build flat as well as curved gradient coils. Moreover, using the Stream Function Method developed in this dissertation, we are able to completely design a gradient set consisting of all three gradient coils. Tests in an MRI scanner confirmed the validity and accuracy of this

approach. The presented Method of Moments formulation helps us to study the effect of rapidly changing magnetic fields, and their effect on a biological body placed inside the gradient coil set.

6.2 Recommendations for Future Work

Based on the practical measurements of the coils in the MRI scanner, it became apparent that a number of issues should be addressed as part of future research efforts. They include:

- The stress distribution in the coil former should be considered. Obviously, shape and material of the former has a major influence on the gradient coils' structural integrity and acoustic noise level.
- The power dissipation in the gradient coils should be considered more comprehensively. A power dissipation term may be introduced into the cost function.
- Based on the results of the power dissipation studies, a cooling mechanism should be designed.
- Since the pulse sequences have temporal responses, a time domain version of the MoM should be explored. It would allow the direct study of transient effect due to the switching of the gradient coils.

References

- [1] V. Bangert, P. Mansfield, "Magnetic Field Gradient Coils for NMR Imaging," *J. Phys. E: Sci. Instrum.*, vol. 15, pp. 235-239, 1982.
- [2] R. Turner, "Gradient Coil Design: a Review of Methods," *Magnetic Resonance Imaging*, vol. 11, pp. 903-920, 1993.
- [3] D.I. Hoult, Oxford University, Ph.D. Thesis, 1977.
- [4] R.C. Compton, "Gradient Coil Apparatus for a Magnetic Resonance System," US Patent 4,456,881. Priority date January 18, 1982.
- [5] K.H. Schweikert, R. Krieg, F. Noack, "A High-Field Air-Cored Magnet Coil Design for Fast-Field-Cycled NMR," *J. Magn. Reson.*, 78, pp. 77-96, 1988.
- [6] E. Wong, A. Jesmanowicz, J.S. Hyde, "Coil optimization for MRI by Conjugate Gradient Descent," *Magn. Res. Med.*, 21, pp. 39-48, 1991.
- [7] R. Turner, "A Target Field Approach to Optimal Coil Design," *J. Phys, D: Appl. Phys.* 19, pp. L147-L151, 1986.
- [8] R. Turner, "Minimum inductance coils," *Journal of Physics E: Sci. Instrum.* 21, pp. 948-952, 1988.
- [9] R. Turner, R.M. Bowley, "Passive Screening of Switched Magnetic Field Gradients," *Journal of Physics E: Sci. Instrum.* 21, pp. 876-879, 1986.
- [10] R. Bowtell, P. Mansfield, "Screened Coil Designs for NMR Imaging in Magnets with Transverse Field Geometry," *Meas. Sci. Technol.*, 1, pp. 431-439, 1990.
- [11] H. Liu, "Finite Size Bi-Planar Gradient Coil for MRI," *IEEE Trans. on Magn.*, vol. 34, No. 4, pp. 2162-2164, July 1998.
- [12] D. Green, R.W. Bowtell, P.G. Morris, "Uniplanar Gradient Coil for Brain Imaging," *Proc. Intl. Soc. Mag. Reson. Med.* 10, 2002.
- [13] J. Leggett, S. Crosier, S. Blackband, B. Beck, R.W. Bowtell, "Multilayer Transverse Gradient Coil Design," *Concepts in Magnetic Resonance Part B*, 16B(1), pp. 38-46, 2003.
- [14] Z.H. Cho, J.H. Yi, "A Novel Type of Surface Gradient Coil," *Journal of Magnetic Resonance*, 94, pp. 471-485, 1991.

- [15] F. Shi, "Optimal Designs of Gradient and RF Coils for Magnetic Resonance Imaging (MRI) Instrument," Ph.D. Dissertation, Worcester Polytechnic Institute, 1996.
- [16] F. Shi, R. Ludwig, "Two- and Three-Dimensional Numerical Analysis of Gradient and Parasitic Gradient Fields of a Three-Channel Surface Gradient Coil for Magnetic Resonance Imaging," IEEE Transactions on Magnetics, vol. 32, no. 1, pp. 195-207, January 1996.
- [17] S.M. Rao, D.R. Wilton and A.W. Glisson, "Electromagnetic Scattering by Surfaces of Arbitrary Shape," IEEE Trans. Antennas Propagat., vol. AP-30, no. 3, pp. 409-418, May 1982.
- [18] S. Rao and D.R. Wilton, "Transient Scattering by Conducting Surfaces of Arbitrary Shape," IEEE Trans. Antennas Propagat., vol. 39, no. 1, pp. 56-61, Jan. 1991.
- [19] S.Y. Chen, W.C. Chew, J-S. Zhao, "Analysis of Low Frequency Scattering from Penetrable Scatterers", IEEE Trans. on Geoscience and Remote Sensing, vol. 39, no. 4, pp. 726-735, April 2001.
- [20] D.H. Schaubert, D.R. Wilton and A.W. Glisson, "A Tetrahedral Modeling Method for Electromagnetic Scattering by Arbitrary Shaped Inhomogeneous Dielectric Bodies," IEEE Trans. Antennas Propagat., vol. AP-32, no. 1, pp. 77-85, Jan. 1984.
- [21] S. Antenor and L. Mendes, "Method of Moments with Solenoidal Basis Functions: An Approach to Analyze the Scattering by Inhomogeneous Dielectrics," Computation in Electromagnetics, 10-12 April 1996, Conference Publication No. 420, © IEEE, 1996.
- [22] L. Mendes and S. Antenor, "A Tridimensional Solenoidal Basis Function to Analyze 3D Scattering of Homogeneous Dielectrics Using the Method of Moments," SBMO/IEEE MTT-S IMOC'95 Proceedings.
- [23] T.F. Eibert and V. Hansen, "On the Calculation of Potential Integrals for Linear Source Distributions on Triangular Domains," IEEE Trans. Antennas Propagat., vol. 43, no. 12, pp. 1499-1502, Dec. 1995.
- [24] Mie, Ann. Physik, vol. 25, 377, 1908.

- [25] J.A. Stratton, "Electromagnetic Theory", McGraw-Hill Book Company, Inc., 1941.
- [26] Paul J. Keller, "Basic Principles of MR Imaging", Department of Magnetic Resonance Research, Barrow Neurological Institute, St. Joseph's Hospital and Medical Center, Phoenix, AZ 85013
- [27] G. Bodganov, R. Ludwig, "Analysis of High-Field RF Coils Using the Method of Lines," vol. 16B, issue 1, pp. 22-37.

Appendix A Mie Series Solution

Mie Series Solution

We consider a sphere of radius a and a plane electromagnetic wave propagating along the z -axis with an electric field component in x -direction.

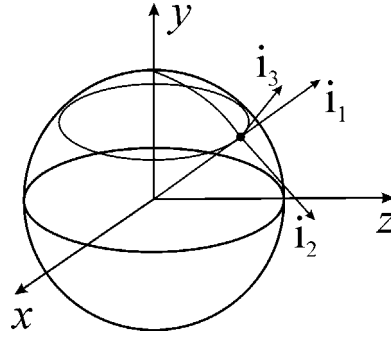


Figure A.1: Spherical system of coordinates.

First of all, unit vectors \mathbf{i}_1 , \mathbf{i}_2 , \mathbf{i}_3 are defined for every point (x, y, z) in the Cartesian system of coordinates. Thus, we determine

$$\mathbf{i}_1 = \begin{pmatrix} x/\sqrt{x^2 + y^2 + z^2} \\ y/\sqrt{x^2 + y^2 + z^2} \\ z/\sqrt{x^2 + y^2 + z^2} \end{pmatrix} \quad (\text{A.1})$$

and

$$\mathbf{i}_2 = \begin{pmatrix} xz/\sqrt{x^2z^2 + y^2z^2 + (x^2 + y^2)^2} \\ yz/\sqrt{x^2z^2 + y^2z^2 + (x^2 + y^2)^2} \\ -(x^2 + y^2)/\sqrt{x^2z^2 + y^2z^2 + (x^2 + y^2)^2} \end{pmatrix} \quad (\text{A.2})$$

Since the basis is orthogonal, the third unit vector is given by

$$\mathbf{i}_3 = \mathbf{i}_1 \times \mathbf{i}_2 \quad (\text{A.3})$$

The expansion of the incident field in spherical wave functions is

$$\mathbf{E}_i = \mathbf{a}_x E_0 e^{j\omega t - jk_z z} = E_0 e^{j\omega t} \sum_{n=1}^{\infty} (-j)^n \frac{2n+1}{n(n+1)} (\mathbf{m}_{o1n}^{(1)} + j\mathbf{n}_{e1n}^{(1)}) \quad (\text{A.4})$$

$$\mathbf{H}_i = \mathbf{a}_x \frac{k_2}{\mu_2 \omega} e^{j\omega t - jk_z z} = -\frac{k_2 E_0}{\mu_2 \omega} e^{j\omega t} \sum_{n=1}^{\infty} (-j)^n \frac{2n+1}{n(n+1)} (\mathbf{m}_{e1n}^{(1)} - j\mathbf{n}_{o1n}^{(1)}) \quad (\text{A.5})$$

where

$$\mathbf{m}_{o1n}^{(1)} = \pm \frac{1}{\sin \theta} j_n(k_2 R) P_n^1(\cos \theta) \frac{\cos \phi}{\sin \theta} \mathbf{i}_2 - j_n(k_2 R) \frac{\partial P_n^1}{\partial \theta} \frac{\sin \phi}{\cos \theta} \mathbf{i}_3 \quad (\text{A.6})$$

$$\begin{aligned} \mathbf{n}_{o1n}^{(1)} &= \frac{n(n+1)}{k_2 R} j_n(k_2 R) P_n^1(\cos \theta) \frac{\sin \phi}{\cos \theta} \mathbf{i}_1 + \frac{1}{k_2 R} [k_2 R j_n(k_2 R)]' \frac{\partial P_n^1}{\partial \theta} \frac{\sin \phi}{\cos \theta} \mathbf{i}_2 \\ &\pm \frac{1}{k_2 R \sin \theta} [k_2 R j_n(k_2 R)]' P_n^1(\cos \theta) \frac{\cos \phi}{\sin \theta} \mathbf{i}_3 \end{aligned} \quad (\text{A.7})$$

Here $j_n(\rho)$ is a spherical Bessel function, $h_n^{(2)}(\rho)$ is a spherical Hankel function, and

$P_n^m(x)$ are associated Legendre functions. Reflected fields are given in the form

$$\mathbf{E}_r = E_0 e^{j\omega t} \sum_{n=1}^{\infty} (-j)^n \frac{2n+1}{n(n+1)} (a_n^r \mathbf{m}_{o1n}^{(3)} + j b_n^r \mathbf{n}_{e1n}^{(3)}) \quad (\text{A.8})$$

$$\mathbf{H}_r = -\frac{k_2 E_0}{\mu_1 \omega} e^{j\omega t} \sum_{n=1}^{\infty} (-j)^n \frac{2n+1}{n(n+1)} (b_n^r \mathbf{m}_{e1n}^{(3)} - j a_n^r \mathbf{n}_{o1n}^{(3)}) \quad (\text{A.9})$$

when $R > a$.

The fields inside the sphere (transmitted fields) are

$$\mathbf{E}_t = E_0 e^{j\omega t} \sum_{n=1}^{\infty} (-j)^n \frac{2n+1}{n(n+1)} (a_n^t \mathbf{m}_{o1n}^{(1)} + j b_n^t \mathbf{n}_{e1n}^{(1)}) \quad (\text{A.10})$$

$$\mathbf{H}_t = -\frac{k_1 E_0}{\mu_1 \omega} e^{j\omega t} \sum_{n=1}^{\infty} (-j)^n \frac{2n+1}{n(n+1)} (b_n^t \mathbf{m}_{e1n}^{(1)} - j a_n^t \mathbf{n}_{o1n}^{(1)}) \quad (\text{A.11})$$

when $R < a$.

Functions $\mathbf{m}_{e1n}^{(3)}$ and $\mathbf{n}_{o1n}^{(3)}$ are obtained by replacing $j_n(k_2 R)$ by $h_n^{(2)}(k_2 R)$ in (A.6) and (A.7). The boundary conditions at $R = a$ are

$$\mathbf{i}_1 \times (\mathbf{E}_i + \mathbf{E}_r) = \mathbf{i}_1 \times \mathbf{E}_t \quad (\text{A.12})$$

$$\mathbf{i}_1 \times (\mathbf{H}_i + \mathbf{H}_r) = \mathbf{i}_1 \times \mathbf{H}_t \quad (\text{A.13})$$

This leads to

$$\begin{aligned} a_n^t j_n(N\rho) - a_n^r h_n^{(2)}(\rho) &= j_n(\rho) \\ a_n^t [N\rho j_n(N\rho)]' - a_n^r [\rho h_n^{(2)}(\rho)]' &= [\rho j_n(\rho)]' \\ N b_n^t j_n(N\rho) - b_n^r h_n^{(2)}(\rho) &= j_n(\rho) \\ b_n^t [N\rho j_n(N\rho)]' - N b_n^r [\rho h_n^{(2)}(\rho)]' &= N [\rho j_n(\rho)]' \end{aligned} \quad (\text{A.14})$$

where $k_1 = Nk_2$, $\rho = k_2 a$, $k_1 a = N\rho$, This system is then solved:

$$\begin{aligned} a_n^r &= -\frac{j_n(N\rho)[\rho j_n(\rho)]' - j_n(N\rho)[N\rho j_n(N\rho)]'}{j_n(N\rho)[\rho h_n^{(2)}(\rho)]' - h_n^{(2)}(\rho)[N\rho j_n(N\rho)]'} \\ b_n^r &= -\frac{j_n(\rho)[N\rho j_n(N\rho)]' - N^2 j_n(N\rho)[\rho j_n(\rho)]'}{h_n^{(2)}(\rho)[N\rho j_n(N\rho)]' - N^2 j_n(N\rho)[\rho h_n^{(2)}(\rho)]'} \\ a_n^t &= \frac{-h_n^{(2)}(\rho)[\rho j_n(\rho)]' + j_n(\rho)[\rho h_n^{(2)}(\rho)]'}{j_n(N\rho)[\rho h_n^{(2)}(\rho)]' - h_n^{(2)}(\rho)[N\rho j_n(N\rho)]'} \\ b_n^t &= \frac{-j_n(\rho)N[\rho h_n^{(2)}(\rho)]' + N h_n^{(2)}(\rho)[\rho j_n(\rho)]'}{h_n^{(2)}(\rho)[N\rho j_n(N\rho)]' - N^2 j_n(N\rho)[\rho h_n^{(2)}(\rho)]'} \end{aligned} \quad (\text{A.15})$$

The spherical Bessel functions are defined as:

$$j_n(z) = \sqrt{\frac{\pi}{2z}} J_{n+\frac{1}{2}}(z) \quad \text{and} \quad h_n^{(2)}(z) = \sqrt{\frac{\pi}{2z}} H_{n+\frac{1}{2}}^{(2)}(z) \quad (\text{A.16})$$

where $J_n(z)$ and $H_n^{(2)}(z)$ are ordinary Bessel functions.

To find the derivatives of the spherical Bessel functions present in (A.15) we use the expression

$$\left(\frac{1}{z} \frac{d}{dz}\right)^m (z^{n+1} f_n(z)) = z^{n-m+1} f_{n-m}(z) \quad (\text{A.17})$$

where $f_n(z)$ can be any function $j_n(z)$, $y_n(z)$, $h_n^{(1)}(z)$, $h_n^{(2)}(z)$. From (A.17) we obtain

$$\begin{aligned} \frac{d}{dz}(zj_n(z)) &= zj_{n-1}(z) - nj_n(z) \\ \frac{d}{dz}(zh_n^{(2)}(z)) &= zh_{n-1}^{(2)}(z) - nh_n^{(2)}(z) \end{aligned} \quad (\text{A.18})$$

The associated Legendre functions can be found from the expression

$$P_n^m(x) = (-1)^m (1-x^2)^{m/2} \left(\frac{d}{dx}\right)^m P_n(x) \quad (\text{A.19})$$

Specifically, for $m = 1$ we obtain

$$\frac{dP_n(\cos\theta)}{d\theta} = P_n^1(\cos\theta) \quad (\text{A.20})$$

Also, from (A.19) we have

$$\begin{aligned} \frac{dP_n^1(x)}{dx} &= x(1-x^2)^{-1/2} \frac{dP_n(x)}{dx} - (1-x^2)^{1/2} \frac{d^2P_n(x)}{dx^2} \Rightarrow \\ \frac{dP_n^1(\cos\theta)}{d\theta} &= \frac{\cos\theta}{\sin\theta} P_n^1(\cos\theta) + P_n^2(\cos\theta) \end{aligned} \quad (\text{A.21})$$

The code for computing the Mie solution was implemented in MATLAB. We took advantage of MATLAB's built-in Bessel functions and associated Legendre functions.

The program listing is given below. The program is written such that it saves data in a Tecplot format. Tecplot is a useful tool for visualizing the scientific data.

Program listing

```

%*****
% This program computes Mie solution for
% diffraction of a plane wave on a sphere
%*****
clear all
% load mesh
FileName=strcat('volume.n');
FID=fopen(FileName,'rt');
pp=fscanf(FID, '%f');
NodesTotal=pp(1);
TetraTotal=pp(2);
p=zeros(3,NodesTotal);
t=zeros(4,TetraTotal);

```

```

kkk=3;

for s=1:NodesTotal
    kkk=kkk+1;
    p(1,s)=pp(kkk); kkk=kkk+1;
    p(2,s)=pp(kkk); kkk=kkk+1;
    p(3,s)=pp(kkk); kkk=kkk+1;
end

for s=1:TetraTotal
    kkk=kkk+1;
    t(1,s)=pp(kkk); kkk=kkk+1;
    t(2,s)=pp(kkk); kkk=kkk+1;
    t(3,s)=pp(kkk); kkk=kkk+1;
    t(4,s)=pp(kkk); kkk=kkk+1;
end
fclose (FID);
clear pp;
for s=1:NodesTotal
    tempy=p(2,s);
    tempz=p(3,s);
    p(2,s)= tempy*cos(0.01)+tempz*sin(0.01);
    p(3,s)=-tempy*sin(0.01)+tempz*cos(0.01);
end

%*****
a=0.02;          % sphere radius
f=2e8;          % frequency
epsr=1;         % epsilon r
sigma=0.0;      % conductance

eps0=8.854e-12;
c_light=3e8;    % speed of light
mu=4*pi*1e-7;   % free space permeability
omega=2*pi*f;   % circular frequency
lambda=c_light/f; % free space wavelength
k=2*pi/lambda;  % wave number in a free space
eps=2-j*(sigma/omega/eps0); % epsilon_r-j*(sigma/omega/eps0)
kl=sqrt(eps)*k; % wave number inside the sphere
alpha=2*pi*a/lambda;
m=sqrt(eps);
N=15; % number of terms in the Mie series

for n=1:N
    term1=spbesselh(n,2,alpha)*(alpha*spbesselj(n-1,alpha)-n*spbesselj(n,alpha));
    term2=spbesselj(n,alpha)*(alpha*spbesselh(n-1,2,alpha)-n*spbesselh(n,2,alpha));
    term3=spbesselh(n,2,alpha)*(m*alpha*spbesselj(n-1,m*alpha)-n*spbesselj(n,m*alpha));
    term4=spbesselj(n,m*alpha)*(alpha*spbesselh(n-1,2,alpha)-n*spbesselh(n,2,alpha));
    c(n)=(-term1+term2)/(-term3+term4);
    d(n)=(-m*term2+m*term1)/(term3-m^2*term4);
end

E=(1+j)*zeros(NodesTotal,3);
H=(1+j)*zeros(NodesTotal,3);
for s=1:NodesTotal
    % find unit vectors in each point
    x=p(1,s); y=p(2,s); z=p(3,s);
    r=norm([x y z]);
    fi=angle(x+j*y);
    ar=[x/r y/r z/r];
    atheta(1)=x*z;
    atheta(2)=y*z;
    atheta(3)=- (x^2+y^2);
    temp=sqrt(atheta(1)^2+atheta(2)^2+atheta(3)^2);
    atheta(1)=atheta(1)/temp;
    atheta(2)=atheta(2)/temp;
    atheta(3)=atheta(3)/temp;
    afi=cross(ar,atheta);
    theta=acos(ar(3));
    for n=1:N
        clear p1;
        p1=legendre(n,ar(3)); P1n=p1(2);
        mn_atheta=1/sin(theta)*spbesselj(n,kl*r)*P1n;
        mn_afi=-spbesselj(n,kl*r)*dP1ndtheta(n,theta);
        nn_ar=n*(n+1)/(kl*r)*spbesselj(n,kl*r)*P1n;
        nn_atheta=1/(kl*r)*((kl*r)*spbesselj(n-1,kl*r)-
n*spbesselj(n,kl*r))*dP1ndtheta(n,theta);
        nn_afi=-1/(kl*r*sin(theta))*((kl*r)*spbesselj(n-1,kl*r)-n*spbesselj(n,kl*r))*P1n;
        mn=mn_atheta*cos(fi)*atheta+mn_afi*sin(fi)*afi;

```

```

nn=nn_ar*cos(fi)*ar+nn_atheta*cos(fi)*atheta+nn_afi*sin(fi)*afi;
E(s,:) = E(s,:) + (-j)^n*(2*n+1)/(n*(n+1))*c(n)*mn+j*d(n)*nn);
mn=mn_atheta*(-sin(fi))*atheta+mn_afi*cos(fi)*afi;
nn=nn_ar*sin(fi)*ar+nn_atheta*sin(fi)*atheta+nn_afi*(-cos(fi))*afi;
H(s,:) = H(s,:) + (-j)^n*(2*n+1)/(n*(n+1))*d(n)*mn-j*c(n)*nn);
end
end
H=-k1/(omega*mu)*H;

% save date in Tecplot format
FileName=strcat('sphere_field.dat');
FID=fopen(FileName,'w');
fprintf(FID, ' %s\n', 'TITLE = "MESH"');
fprintf(FID, ' %s', 'VARIABLES="X", "Y", "Z", "AbsE", "Emagn_x", "Ephase_x", "Emagn_y",
"Ephase_y", "Emagn_z", "Ephase_z"');
fprintf(FID, ' %s\n', 'AbsH", "Hmagn_x", "Hphase_x", "Hmagn_y", "Hphase_y",
"Hmagn_z", "Hphase_z"');
fprintf(FID, ' %s', 'ZONE T="mesh_surf" I=');
fprintf(FID, ' %5.0f', NodesTotal);
fprintf(FID, ' %s\n', 'F=FEPOINT, ET=TETRAHEDRON');
for s=1:NodesTotal
fprintf(FID, ' %g', p(1,s));
fprintf(FID, ' %g', p(2,s));
fprintf(FID, ' %g', p(3,s));
fprintf(FID, ' %g', sqrt(abs(E(s,1))^2+abs(E(s,2))^2+abs(E(s,3))^2));
fprintf(FID, ' %g', norm(E(s,1)));
fprintf(FID, ' %g', angle(E(s,1)));
fprintf(FID, ' %g', norm(E(s,2)));
fprintf(FID, ' %g', angle(E(s,2)));
fprintf(FID, ' %g', norm(E(s,3)));
fprintf(FID, ' %g', angle(E(s,3)));
fprintf(FID, ' %g', sqrt(abs(H(s,1))^2+abs(H(s,2))^2+abs(H(s,3))^2));
fprintf(FID, ' %g', norm(H(s,1)));
fprintf(FID, ' %g', angle(H(s,1)));
fprintf(FID, ' %g', norm(H(s,2)));
fprintf(FID, ' %g', angle(H(s,2)));
fprintf(FID, ' %g', norm(H(s,3)));
fprintf(FID, ' %g\n', angle(H(s,3)));
end
for s=1:TetraTotal
fprintf(FID, ' %5.0f', t(1,s));
fprintf(FID, ' %5.0f', t(2,s));
fprintf(FID, ' %5.0f', t(3,s));
fprintf(FID, ' %5.0f\n', t(4,s));
end
fclose (FID);

% Given values of n and x
% this function computes Spherical Bessel Function jn(x)
function B = spbesselj(n,x)
B=sqrt(pi/(2*x))*besselj(n+0.5,x);

% Given values of order, n and x
% this function computes Spherical Bessel Function hn(x)
function B = spbesselh(n,order,x)
B=sqrt(pi/(2*x))*besselh(n+0.5,order,x);

% Given values of n and theta
% this function computes dPln/dTheta derivative
function B = dPln_dTheta(n,theta)
ppp=legendre(n,cos(theta));
temp = cos(theta)/sin(theta)*ppp(2);
if (n>=2) temp=temp+ppp(3); end
B=temp;

```